PLASMA POTENTIAL IN A MAGNETIC MIRROR

WITH ELECTRON CYCLOTRON RESONANCE HEATING

by

Philip K. Smith

A thesis submitted in partial fulfullment

of the requirements for the degree of

DOCTOR OF PHILOSOPHY

(Physics)

at the

University of Wisconsin - Madison

1983

ABSTRACT

Plasma Potential in a Magnetic Mirror

with Electron Cyclotron Resonance Heating

Philip K. Smith

(Under the supervision of Professor J. C. Sprott)

Experimental and theoretical studies of the ECRH plasma in the University of Wisconsin "DC Machine" magnetic mirror have been undertaken.

Typical plasma parameters in these experiments were T_e ~ 10-30 eV, T_i ~ 4 eV, V_{po} (plasma potential at midplane) ~ 20-50 V, midplane plasma density n_o ~ 10^{16} m^{-3}, B_o (magnetic field strength on axis at midplane) ~ .005-.01 T, mirror ratio R ~ 5-20. The principal experimental findings were the appearance of strong density peaks (~ 2 x background) and notable V_f dips ($\sim\frac{kT_e}{e}$) in a narrow (~ 1 cm) region near the axial positions of cyclotron resonance. The properties of these dips do not change greatly over the range of operating parameters, but are narrower at higher pressures.

The explanation for this resonance zone structure is the accumulation of turning points at the resonance zone. This is caused the by continual increase of perpendicular electron energy for the electrons that pass through the resonance zone. The resulting increase of density at the resonance zone and the full width at half maximum (FWHM) of the density peak are quantitatively analyzed by finding the steady state electron distribution function as modified by ECRH. Models are presented which incorporate simplified ECRH, collision, and loss terms. A resonance zone density peak with the observed order of magnitude of peak-to-base ratio and FWHM is predicted.

Other issues addressed herein include calculation of Maxwellian-weighted fractions of velocity space with various plasma potential and magnetic field profiles, a comparison of models for the prediction of the midplane plasma potential, and the details of effective numerical profile determination from the electron distribution function.

ACKNOWLEDGEMENTS

The number of people who have assisted me in one way or another is too great to allow me to credit each individually, but I express my thanks to all.

A few who must be credited with giving me greater than average help are J. Callen, T. Lovell, P. Nonn, S. Prager, J. C. Sprott, K. Symon, and R. Vallem.

Discussions with fellow graduate students Rich Groebner, Mike Makowski, Roger Richards, Evan Rose, and Mike Zarnstorff often provided useful insights.

I am grateful for the help of L. Kehren and C. Seeliger during the final preparation of this manuscript.

Financial support for this research was provided by DOE.

Finally, I would like to thank my advisor, Dr. J. C. Sprott, for his comments and criticism.

TABLE OF CONTENTS

PLP Reports

Occasional references are made to "PLP" reports. These Plasma Lab Papers are internal reports of the University of Wisconsin Plasma Physics Group, and can be obtained upon request to:

Plasma Physics Office
University of Wisconsin
1150 University Avenue
Madison, Wisconsin 53706

Chapter 1. Introduction

Of all available physical processes, nuclear fusion generates the most energy per unit fuel mass.[1] This alone would make large scale power generation from fusion interesting. Combined with the fact that the fuel (deuterium obtained from water or tritium derived from lithium) is relatively cheap, and that conventional sources of power are either severely limited (hydroelectric, wind power) or will be exhausted on a time scale short compared with that of civilization (fossil fuels), the search for a method of controlled generation of power from nuclear fusion has assumed practical importance.

A less commonly mentioned prospect is that if the mass of a fusion reactor could be made small enough, it would be appealing as a propulsion system for long space trips, since the reaction products have a speed which is a significant fraction of the speed of light.[2]

The research reported here is just one of the many facets of the wide ranging pursuit of the goal of controlled fusion. It concentrates on the affects of electron cyclotron resonance heating (ECRH) in a magnetic mirror configuration. ECRH is more than mere heating; it alters the form of the distribution function and thereby the particle transport and the heating rate itself. Working knowledge in both these areas will be needed if fusion reactors using ECRH are to become reality.

In this report the relation between density and potential profiles is elucidated both with probe data, and with theory based on the trapped and untrapped regions of velocity space. Models describing a general mirror (ECRH not explicitly included), such as the free-fall model and models based on scattering rates, are discussed and compared with data. Detailed attention is given to plasma properties near the cyclotron resonance zones. It is found that a comprehensive explanation of resonance zone phenomena requires determination of the electron distribution function in the presence of ECRH. Models of increasing sophistication are presented to accomplish this goal, culminating in a finite grid numerical method and the semi-analytic KKP distributions. Several ancillary issues related to plasma potential in a mirror are discussed, such as the relation between turning point density and particle density, the properties of "sloshing" distributions, and the relative importance of fluctuations in V_f dips. It is hoped that this thesis will prove useful to other researchers.

The present work is part of a long progression of magnetic mirror concepts and experiments. As early as 1912 Stoermer noted that a dipole magnetic field could contain charged particles which would execute quasiperiodic motion. The application of magnetic fields in plasma confinement predates magnetic mirror devices. The pinch effect, pointed out by W. H. Bennett, L. Tonks, and W. Allis in the 1930's, makes use of the magnetic field produced by the plasma current itself. S. Lundquist[3] showed such dis-

charges to be unstable to the "kink" and "sausage" instabilities, but could be stabilized by the addition of a magnetic field parallel to the discharge axis. This was apparently first done experimentally by A. L. Bezbatchenko, et. al.[4] in 1956.

The conventional magnetic mirror concept was first proposed as an alternative to the toroidal z-pinch and the stellarator by York at Lawrence Livermore Laboratory (LLNL) and by Budker[5] in the Soviet Union in 1951. Hopes for mirrors as fusion devices were high as a result of optimistic estimates for confinement time. But by 1955 it was suspected that instabilities, especially the interchange, or flute instability, could reduce the confinement time drastically. Nevertheless a series of mirror experiments was undertaken. The interchange instability was not found, except in special cases, due to stabilization by the effect of finite gyroradius, a mechanism suggested by Rosenbluth, Krall, and Rostoker,[6] and to "line-tying" with equipotential surfaces outside the plasma, first mentioned by Post and co-workers.[7]

In early simple mirrors like DCX at Oak Ridge, and OGRA in the USSR, high energy ions were injected with the hope of building up density directly to thermonuclear levels.[5] But losses were so great that the density of hot ions never exceeded $\sim 5 \times 10^{15}$ m^{-3}.

The magnetic mirror concept entered a new phase with the development of the "minimum-B" mirror, in which the magnetic field increases from the center of the mirror radially as well as axially. Berkowitz[8] and others had pointed out that this would transform the mirror into a hydromagnetically stable configuration. This was accomplished by Ioffe[9] in the Soviet Union in 1961. A series of current carrying rods parallel to the axis of the simple mirror, exterior to the plasma, was added. In other words, a linear multipole field was superimposed upon that of the simple mirror. Other means of achieving the minimum-B mirror configuration were used with the "baseball" and "yin-yang" type coils.

The effects of electrostatic fields on mirror confinement were first mentioned by Post,[10,11] BenDaniel[12] and Yushmanov.[13] The electrostatic potential for a simple mirror containing a thermonuclear plasma is a nuisance, since the greater collision frequency for electrons forces them into the loss cone more rapidly than ions. A positive potential then develops in the interior to balance the loss rates of electrons and ions. This acts to increase ion loss, which is bad since net power production requires the fusion reactants—the ions—to have a long confinement time.

The tandem mirror exploits a shaped electrostatic potential to enhance confinement of both ions and electrons. In the original concept of Dimov, et. al.,[14] and Fowler and Logan,[15] in 1976 and 1977 respectively, simple mirrors ("plugs") with a strong positive central potential are linked by a long, low magnetic field "solenoid". The electrostatic potential is lowered in the solenoid. Ions in the solenoid are blocked from passing the plugs because of the high potential of the plugs, as well as the usual

magnetic mirror effect. The electrons can penetrate the plugs, but if the the solenoid potential is sufficiently high, then most electrons will not have sufficient energy to reach the end wall, which is at ground potential. The first large tandem mirror was the TMX at Lawrence Livermore Laboratory, which began operations in 1979.[16] Results from TMX have verified the tandem mirror concept, and work is proceeding on a larger tandem mirror, MFTF-B.[5,32] A small tandem mirror, Gamma-6[53], has been built in Japan. AMBAL-I in the Soviet Union was in the early operation stage in 1982, and Phaedrus is in operation at the University of Wisconsin, but ECRH is not emphasized in either of the the latter devices.[5]

The first reported use of ECRH in a mirror machine was by an Oak Ridge group starting in early 1960, when a 13 cm. wavelength radar transmitter was directed onto a gas arc within a magnetic mirror.[17]

Apparently the first device to be built specifically to test ECRH was the PTF (Physics Test Facility) in Oak Ridge, under the direction of R. Dandl and W. B. Ard in 1962.[54] This device had a 2:1 mirror ratio, and with 5 KW cw at 10.6 GHz in 1964, produced $\sim 5 \times 10^{17}$ m^{-3} and had a hot electron component of mean energy 120 KeV. Slightly later the "ECR device" was operated at Princeton[18]. An RF pulse at 10.5 GHz formed a plasma which was used to study the onset and evolution of instabilities in a mirror. At Nagoya, Japan 6.4 GHz ECRH with power levels up to 5 KW was employed in

the TPM device starting in 1968. A number of features were discovered that are common to ECRH mirrors, such as the the three-component composition of hot electrons, cold electrons, and cold ions.[26] At Oak Ridge National Laboratory the study of steady state, hot electron plasmas formed by ECRH was continued in a system of toroidally linked mirrors bearing the name "ELMO bumpy torus", or EBT.[19] A conspicuous aspect of this experiment has been the rings of hot electrons that form near the midplanes of the linked mirrors, about 10 cm from the axis. These have energies of a few hundred KeV to a few MeV, have radial extent of 3-4 cm (a few electron gyroradii), and extend axially 10 cm. This device has now been altered from the orginal "EBT-I" to "EBT-S". The principle difference is in the use of higher heating powers at a higher frequency (65 KW at 28 GHz). The ring temperature is now ~500 KeV for a density of $2\text{-}3 \times 10^{17}$ m^{-3}, compared with ~150 KeV for EBT-I at the same density.[25] A device similar to EBT-I is the Nagoya Bumpy Torus (NBT). It has a major radius of 1.6 m and a minor radius of .125 m. Its bulk resonant frequency is 8.5 GHz compared with 18 GHz in EBT-I. The prospect of using ECRH in the high magnetic fields of a prospective fusion reactor has brightened in recent years with the advent of the gyrotron. Cw powers of 200 KW at 28 GHz are currently available, and 110 GHz seems possible.[5,33] At electron temperatures over a few KeV both the o- and the x-mode are efficiently absorbed.

Much attention is given in this thesis to the alteration of the plasma density and potential near the resonance zone. Among the researchers who have commented on plasma behavior within the resonance zone is Ikezi,[26] who noted that microwave noise and an x-ray emission peak occured at the positions of fundamental resonance, and at the second harmonic. Galaktionov et. al.[27] inferred from diamagnetic signals that most particles were reflected in a narrow region near resonance. Haste and Lazar[29] found that density peaks occured near resonance. The previous workers explained their observations by invoking an accumulation of turning points, but did not go as far as the present study in attempting a quantitative modeling of the resonance zone structure.

It has now been demonstrated that ECRH can be efficiently absorbed in low temperature plasmas in a variety of magnetic configurations.[20-24] The number of mirror machine experiments alone that have employed ECRH is now quite large. Table 1.1 gives a summary of the major mirror ECRH efforts.

The device used in the current experiments is much smaller than the devices at LLNL and Oak Ridge, but important lessons can still be learned due to the ease of modifying the device to resolve specific issues.

ECRH mirror theory has also advanced in recent years. The

trapping of cold ions in a narrow potential well at resonance, and its effect on stability. Kesner[31] has proposed using ECRH to create "sloshing" electrons. The name comes from the behavior of the resonance turning electrons, which will have a large density only near resonance, and move with substantial parallel speed across the central region, in analogy with water sloshing in an oscillating bucket. The idea is to induce a potential dip of sufficient size to act as a choke on electron flux. Then it is possible to maintain different electron temperatures on either side, hence the term "thermal barrier". In most tandem mirror models this is placed at the end of the central cell.

The general objective here is to relate the use of ECRH in a mirror to the observed experimental variables, especially near the resonance zones. The influence of the potential profile is crucial in determination of loss rates, heating rates, and probe response. The potential must be found, as self-consistently as possible, from the electron distribution function produced by ECRH. In chapter 2 the basic device systems are described. Chapter 3 describes diagnostic devices and techniques used, while chapter 4 introduces the "cut-out Maxwellian" relation between plasma density and potential. In chapter 5 the global properties of plasma within the device are described, and in chapter 6 detailed attention is given to the properties near the resonance zone. In chapter 7 models are developed which explain the behavior of the plasma and allow prediction of results for other

devices. A summary of the findings is given in chapter 8, and a discussion on the implications for a larger mirror.

Table 1.1

Notable ECRH Experiments in Mirrors

Ref.	Year	Name	Site	device volume (m^3)	hf power (W)	f (GHz)	typical n (m^{-3})	T_e (eV)
54	1962	PTF	Oak Ridge	?	1000	2.3	10^{17} - 10^{18}	10K-50K
18	1965	ECR	Princeton	.00305	10K	10.5	3×10^{15} - 4×10^{17}	~200K
49	1965	Puffatron	Roehlida	?	40K peak	9.345	2.5×10^{18}	?
26,45	1967	TPM	Nagoya	.0551	5K peak	6.4	10^{16} - 10^{17}	10-20; 150K+
42	1968	Electron Trap	Leningrad	.00705	20K peak 20K peak	9.05 9.35	?	~2K
40,52	1968	Interem	Oak Ridge	.005	22K	10.3	$> 10^{18}$	50K-100K
34	1969	Local Line	Kyoto	.00554	100	2.45	?	10?
39,46,52	1970	ER 2	Prague	.025	3K	2.35	5×10^{16}-5×10^{19}	5-10
52,56	1970	Circe	Saclay	1.7	2.5-10K	10.12	$2-30\times10^{17}$	50K-100K
52,60	1970	Pleiade	Saclay	.031	700 cw	3.	10^{16} - 10^{17}	2K
52	1970	Icare	Saclay	?	1M peak	1.25	10^{18}; 5×10^{15}	20K-100K+
52,39	1970	ELMO	Oak Ridge	.002	5K	55	10^{18};$2-5\times10^{17}$	<100;.5M-4M
					.8K	35		
					1.3K	55		
52,39	1970	IMP	Oak Ridge	.01	500	34	10^{18}	< 1M
44,56	1970	Pulsed Cavity	Madison	.0274	100K	10	?	15K-30K
52	1970	UHF	Ioffe Inst.	.0016	1K	3	10^{15} - 10^{20}	<500
					.2K(cw)	9.4		
					20K pulse	9.4		
48	1971	Wavequide Trap	Moscow	.0068	3K	2.80	3×10^{17};5×10^{15}	100; 80K

Table 1.1

Notable ECRH Experiments in Mirrors
(continued)

Ref.	year	name	site	device volume	hf power	f	typical n	T_e
				(m^3)	(W)	(GHz)	(m^{-3})	(eV)
62,63	1971	DC Machine	Madison	.44	750	2.45	10^{16}	10-30
47	1972	ECR L-Coil	Nagoya	.0275	85	2.45	3×10^{14} - 6×10^{16}	3-25
61	1973	HF Barrier	Moscow	?	10	2.375	5-50 x 10^{13}	20-40
39	1973	Pleiade II	Saclay	.00125	2K	10.1	10^{16}	5K
39	1973	Circe 25KW	Saclay	.106	25K	8	10^{18}	?
39	1973	Eliza	Stuttgart	.177	2K pulse	2.4	10^{16} - 10^{17}	5
39,57,59	1973	Canted Mirror	Oak Ridge	.003	5K	10.6	10^{18};3×10^{17}	<100; ~1M
					800	35		
19,25,39	1973	EBT-I	Oak Ridge	1.35	30K	18	$2\text{-}3\times10^{17}$	250; 150K
					10K	55		
38	1974	Resonator	Marburg	.00094	1500 peak	9.72	?	?
46	1975	RHCP Device	Prague	.061	50K	10	10^{16}-3×10^{17}	10-15
41	1975	Accumulator	Moscow	?	10	2.375	?	20-40
62	1976	Gamma-1	Nagoya	?	?	?	10^{18}	?
62	1976	L-3	Princeton	.013 P	1K-5K	2.45	10^{18}	10-15
37	1976	Tunable Resonator	Moscow	.02	150	2.40	?	5-60
35	1976	Plasma Plug	Nagoya	.00792	500	2.45	?	?
43	1978	RF Plug	Moscow	.0055	20	2.38	10^{16}	40; 1.5K
25,64	1978	EBT-S	Oak Ridge	1.35	60K	18	1.5×10^{18}	500
					200K	28		
50,51,52	1979	PR-6	Kurchatov	.71	?	?	2×10^{18}	10
64	1980	NBT	Nagoya	?	10K	10.6	$3\text{-}5\times10^{17}$	50-140
					30K	8.5		

NOTES ON TABLE 1.1

1. "Year" is date of first published results.

2. "Device Volume" is the vacuum volume except when followed by the letter "P", in which case the value is the plasma volume.

3. Separate row entries under "hf power" and "f" indicate discrete power sources.

4. In "n" and "T_e", values separated by semicolons give the values for the cold (first) and hot (second) populations.

5. Values unobtainable from the sources given are denoted by "?".

REFERENCES AND NOTES FOR CHAPTER 1

[1]Power generation from antimatter annihilation or mass injection into black holes would give a greater energy output per unit input mass, but neither bulk antimatter nor black holes seem to be locally available. Even if they were, suitable control of such processes would make fusion power look trivial.

[2]Commonly mentioned fusion reactions have the following product speeds, assuming negligible energy before reaction, and using center-of-mass coordinates:

Reactants		Products	Q (MeV)	$\frac{v_1}{c}$ (%)	$\frac{v_2}{c}$ (%)
$p + {}^6Li$	→	${}^3He + {}^4He$	4.32	4.2	3.15
$p + {}^7Li$	→	${}^4He + {}^4He$	17.3	6.8	6.8
$p + {}^{11}B$	→	$3\ {}^4He$	8.7	3.9 each	
$n + {}^6Li$	→	$T + {}^4He$	18.3	8.6	6.5
$D + D$	→	$p + T$	4.00	8.00	2.65
$D + D$	→	$n + {}^3He$	3.25	7.2	2.4
$D + {}^3He$	→	$p + {}^4He$	18.3	17.4	4.45
$D + T$	→	$n + {}^4He$	17.6	17.1	4.4
$D + {}^6Li$	→	${}^4He + {}^4He$	22.3	7.7	7.7
$D + {}^6Li$	→	$p + {}^7Li$	5.0	9.6	1.4

[3]S. Lundquist, Phys. Rev. 83, 307 (1951).

[4]A. L. Bezbatchenko, et. al., J. Nucl. Energy 5, 71 (1957).

[5]B. I. Cohen, ed., Status of Mirror Fusion Research 1980, UCAR 10049-80, Lawrence Livermore Laboratory, California, Jan. 2, 1980.

[6]M. N. Rosenbluth, M. A. Krall, and N. Rostoker, Nucl. Fus. Suppl. Pt. 1, 248 (1962).

[7]R. F. Post, et. al., Phys. Rev. Lett. 11, 166 (1960).

[8]J. Berkowitz, H. Grad, and H. Rubin, Proc. 2nd Int'l Conf. on Peaceful Uses of Atomic Energy, UN, Geneva (1958) Vol. 3, p. 171.

[9]Yu. V. Gott, M. S. Ioffe, and V. G. Telkovskii, Nucl. Fus. Suppl., part 3, 1045 (1962)

[10]R. F. Post, Bull. Am. Phys. Soc. 6, 200 (1961).

[11]R. F. Post, Phys. Fluids 4, 902 (1961).

[12]D. J. BenDaniel, Plasma Phys. 3, 235 (1961).

[13]E. E. Yushmanov, Sov. Phys. JETP 22, 409 (1966).

[14]G. I. Dimov, V. V. Zakaidakov, and M. E. Kishinevskii, Sov. J. Plasma Physics 2, 326 (1976).

[15]T. K. Fowler and B. G. Logan, Comments on Plasma Physics and Controlled Fusion 2, 167 (1977).

[16]T. C. Simonen, ed., Summary of Results from the Tandem Mirror Experiment (TMX), UCRL-53120, Lawrence Livermore Laboratory, (Feb. 26, 1981).

[17] R. A. Dandl, et. al. Nuc. Fus. 4, 344 (1964).

[18] L. Ferrari and A. Kuckes, Phys. Fluids 8, 2295 (1965).

[19] C. L. Hedrick, et. al., Physics and Controlled Nuclear Fusion Research 1976, sixth Conf. Proc., Berchtesgaden, Nucl. Fus. Supplement, Vol. II (1977), p. 145.

[20] A. F. Kuckes, Plasma Physics 10, 367 (1968).

[21] H. Grawe, Plasma Physics 11, 151 (1968).

[22] M. A. Liebermann and A. J. Lichtenberg, Plasma Physics 15, 125 (1973).

[23] J. C. Sprott, Phys. Fluids 14, 1795 (1971).

[24] J. C. Sprott and P. H. Edmonds, Phys. Fluids 14, 2703 (1971).

[25] N. C. Wyeth, A. J. Lichtenberg and M. A. Liebermann, Plas. Physics 17, 679 (1975).

[25] N. A. Uckan, J. Fusion Energy 1, 49 (1981).

[26] H. Ikezi, IPPJ-67, (1968).

[27] B. V. Galaktionov, et. al., Sov. Phys.-Tech. Phys 13, 833 (1968).

[29] G. R. Haste and N. H. Lazar, Phys. Fluids 16, 683 (1972).

[30] A. F. Haught, et. al., COO-2277-10, Semi-annual Report of United Technology Research Center, Hartford, Conn., (1977).

[31] J. Kesner, Nuc. Fus. 21, 97 (1981).

[32] D. L. Correll, et. al., Nucl. Fus. 22, 223 (1982).

[33] A. V. Gaponov, et. al. Intl. J. Infrared Millimeter Waves 1, 351 (1980).

[34] H. Abe, et. al., Phys. Lett. A30, 394 (1969).

[35] H. Akiyama and S. Takeda, J. Phys. Soc. Japan 41, 1036 (1976).

[36] A. I Anisinov, N. I. Vinogradov and B. P. Poloskin, Sov. Phys. Tech. Phys. 18, 629 (1975); 18, 459 (1973).

[37] A. A. Balmashnov and K. S. Golovanivskii, Sov. Phys. Tech. Phys. 20, 486 (1976).

[38] K. Bernhardi, Phys. Lett. A50, 324 (1974).

[39] IAEA. World Survey of Major Facilities in Controlled Fusion Research 1973 Edition, (Nuclear Fusion Suppl., Vienna, 1973).

[40] R. A. Dandl, et. al., CN-24/J-6, (presentation at Novosibirsk Conference, 1968).

[41] V. D. Dougar-Jabon, K. S. Golovanivsky and V. D. Schepilov, Physica Scripta 18, 506 (1978).

[42] B. V. Galaktionov, et. al., Sov. Phys. Tech. Phys. 13, 838 (1968).

[43] K. S. Golovanivskii, V. D. Dougar-Jabon and L. A. Pokhmel´nykh, Sov. Phys. Tech. Phys. 19, 1484 (1975).

[44] D. Greene and J. L. Shohet, Plasma Physics 15, 5 (1972).

[45] H. Ikegami, et. al. Nuclear Fusion 13, 351 (1973).

[46] J. Musil and F. Za´cek, Czech. J. Phys. B20, 337 (1970); B23, 736 (1970).

[47] Y. Okamato and H. Tamagawa, Jap. J. Appl. Phys. 11, 726 (1972).

[48] B. I. Patrushev, V. P. Gozak, and D. A. Frank-Kamenetskii, Sov. Phys. Tech. Phys. 15, 1058 (1971).

[49] J. L. Shohet and J. F. Steinhaus, UCRL-12057, Jan., 1965.

[50] B. I. Kanaev, Nuc. Fus. 19, 347 (1979).

[51] B. I. Kaneev and E. E. Yushmanov, Sov. Phys. JETP 40, 290 (1975).

[52] IAEA, World Survey of Major Facilities in Controlled Fusion, (Nuclear Fusion Suppl., Vienna, 1970).

[53] S. Miyoshi, et. al., Plasma Physics and Controlled Nuclear Fusion Research 1980, (Nuclear Fusion Suppl., Vienna, 1981), Vol. I, p. 113

[54] M. C. Becker, et. al., Nuclear Fusion: 1962 Supplement, Pt. 1, p. 345.

[55] A. I. Anisimov, et. al., Nuclear Fusion Supplement, 1969. p. 191

[56] R. Bardet, et. al., Nuclear Fusion 15, 865 (1975).

[57] R. A. Dandl, H. Eason, A. C. England, and J. C. Sprott, Nuclear Fusion 13, 693 (1973).

[58] H. Ikegami, et. al., Phys. Rev. Lett. 19, 778 (1967).

[59] R. A. Dandl, et. al., Proceedings of the Fourth Int'l Conf. on Plasma Physics and Controlled Nuclear Fusion Research, Vol. II, p. 607 (IAEA, Vienna, 1971).

[60] R. Geller, B. Jacquot and C. Jacquot, in Proceedings of the Fourth Int'l Conf. on Plasma Physics and Controlled Nuclear Fusion Research, Vol. II, p. 631 (IAEA, Vienna, 1971).

[61] V. D. Dougar-Jabon, K. S. Golovanvsky and L. A. Pokhmennych, Proceedings of Sixth European Conference on Controlled Fusion and Plasma Physics, Vol. I, p. 259.

[62] IAEA, World Survey of Major Facilities in Controlled Fusion, 1976. (Nuclear Fusion Suppl., Vienna, 1976).

[63] R. Prater, Ph. D. Thesis, University of Wisconsin, (1971).

[64] M. Fujiwari, et. al., in Proc. 8th Int'l Conf. on Plasma Physics and Controlled Nuclear Fusion. [Brussels, 1980] (IAEA, Vienna, 1981) p. 845.

Chapter 2. Description of Apparatus

2.1 Vacuum system.

The device used in these experiments is commonly referred to as the "DC Machine." It has been previously described by Jernigan[1], Prater[2], Richards[3] and Strawitch[4]. The vacuum chamber consists of a cylinder of inside radius 0.47 m and length 0.66 m, with cylindrical extensions of smaller radius at each end of the main tank, bringing the total length of the machine to 1.76 m. Figure 2.1 shows details of the machine. Table 2.1 summarizes the data on machine dimensions.

Pumping is done by a Consolidated Vacuum Corporation 6-inch oil diffusion pump, using Dow Corning silicone pump oil no. 705. Back pumping of the diffusion pump is done by a Welch rotary mechanical pump, rated at 500 liters/second pumping speed. A freon cold trap is located between the diffusion pump and the main tank. A liquid nitrogen cold trap is available on an end plate of the main tank. Roughing of the system is accomplished by either the Welch pump or a portable Heraeus DK45 mechanical pump.

Base pressure is less than 5×10^{-7} torr without use of the liquid nitrogen cold trap, and less than 3×10^{-7} torr with it. Composition of the residual gas was not determined, but in similar vacuum systems water vapor dominates.[16] Pressures less than 10^{-3} torr are read from a Bayard-Alpert ionization gauge, (either type Varian 0563-K2466-305 or Westinghouse WL 5966), located on the top of the main tank, opposite the diffusion pump. System pressures of greater than one micron are read from an NRC type 501 thermocouple gauge located adjacent to the ionization gauge. The foreline pressure is separately monitored by an identical thermocouple gauge. The ratio between the system pressure and the foreline pressure is constant for a given gas, at least in the range of foreline pressures 5 to 60 microns.[4] This fact enables one to extropolate tank pressures into the 10^{-2} range, where one can not use the ionization gauge.

The pressure value taken from an ionization gauge is one of those values generally taken on faith. Unfortunately, not only does the sensitivity $S \equiv \frac{\text{apparent pressure}}{\text{true pressure}}$ vary from gas to gas, but different authorities give different values of S for a given gas, often varying by as much as a factor of two.[8]

To obtain the proper S values for the particular gauges used in the experiment, the following procedure was used. First, a small known volume was filled with a gas at a pressure that allowed use of a McLeod gauge, which gives an absolute value.[8] With the main tank isolated from pumping, a valve was opened to

allow the gas from the small volume to enter the system. Since the ratio of the volumes is known, the expected pressure change in the main tank follows from the ideal gas law. A complication is that when the main tank is not being pumped, the pressure increases linearly with time due to inevitable tiny leaks and/or outgassing. However, by graphing pressure versus time across the time interval during which the new gas was admitted, it is possible to determine the incremental change due to the gas from the small volume alone. Results indicated that the tube used had a relative sensitivity to air of 1.56, not 1.00 as company literature claimed. The relationship between gauge reading and true pressure is given in Table 2.2 for various gases.

2.2 Magnetic field system.

The magnetic fields of the DC machine are produced by independent, continuously adjustable currents in three sets of coaxial coils--"end coils", "Helmholtz coils", and the "internal ring." Coil characteristics are summarized in Table 2.3.

The coils are made of hollow copper tubing. An ethylene glycol-water mixture is pumped through the coils for cooling. The flow is about five gallons per minute, with a differential pressure of 100 to 150 psi.

The axial magnetic field in the DC Machine is readily derived from first principles. At the midplane the magnetic field B_o in Teslas is:

$$B_o = 10^{-4} (.1112\ I_E + 1.0457\ I_H + .2285\ I_R) \qquad (2.2.1)$$

The maximum axial field B_{max}, usually very near the end coil position, in Teslas is

$$B_{max} = 10^{-4} (4.954\ I_E + .5881\ I_H + .03081\ I_R) \qquad (2.2.2)$$

I_E, I_H, and I_R are, respectively, the end coil current, Helmholtz coil current, and internal ring current, in amperes.

The DC Machine has great flexibility in the types of fields that can be produced as a result of the independence of the three coil currents. For the most of the current experiments, the magnetic configuration was that of a simple mirror with mirror ratio 10-20, as shown in fig. 2.2. But if the ring current is run opposed to the other coils (as it usually is), and exceeds

$$|I_R| > .49 I_E + 4.58 I_H$$

then the field at the center is reversed and the magnetic field shape is that of a field reversed mirror, as in fig. 2.3. With the Helmholz coils dominant, the field is essentially linear, as shown in figure 2.4. A relatively unexploited field configuration is shown in figure 2.5. Here the internal ring is run with a high current in the same sense as the other coils, resulting in a high central field and a pair of mirror regions on axis.

For the field reversed mirror and simple mirror configurations the magnetic field along the axis of symmetry is like that shown in figures 2.6a and 2.6b, respectively.

2.3 Microwave System

Previous users[1-4] of the DC Machine have relied mainly on a Lisitano coil[7] mounted in the east extension for plasma production. About 60 watts of S-band (2.45 GHz) microwave power can be coupled to the plasma through this coil.

In the present investigations, however, the majority of experiments made use of microwaves fed into the midplane via a rectangular waveguide. A Thomson-CSF model MCF 1166 Magnetron provides up to 1 KW of 2.45 GHz microwaves. The microwave assembly is shown in Figure 2.7.

A plasma can be established only when surfaces of constant B at the resonant value (.0875 Tesla = 875 Gauss) are present within the device. In typical experiments these resonant surfaces are located on cross sections of the cylindrical extensions on either side of each end coil. There is also a resonant surface concentric around the internal ring whenever $|I_R| > 1300$ amperes.

For some experiments a 300 Mhz, 50 W, UHF magnetron was used. The best coupling occured when the antenna was a straight wire of 23.4 cm (very nearly one quarter wavelength) projecting radially inward from a side port.

There is no plasma breakdown unless the neutral pressure exceeds about 10^{-5} torr. At relatively high pressure (5-100 microns), plasma breakdown can occur without the presence of the external magnetic fields. Such plasmas tend to be localized around internal objects in the tank, where locally intense hf electric fields exist.

Because quantitative predictions of ECRH effects require a value for the hf electric field amplitude E_{hf}, an effort was made to measure this parameter.

One method used was to monitor the resistance of a neon glow tube (NE-2) in the presence of E_{hf}. As the field increases, the relative ionization of the gas within the tube increases, and its resistance falls. The bulb was calibrated by measuring the resistance in the center of an S-band waveguide which had a known hf electric field prior to insertion. The high frequency RMS electric field within a device can be described in terms of the "quality factor", Q:

$$E_{RMS}^2 = \frac{P\,Q}{\varepsilon_o \omega V} \qquad (2.3.1)$$

P is the input power, ω is the angular frequency $2\pi f$, V is the device volume, and $\varepsilon_o = 8.854 \times 10^{-12}$ F/m. The neon bulb resistance method gives $Q_o = 172 \pm 26$, where Q_o is the Q value in the absence of plasma.

Another method which permitted local quantitative measurements was to measure the output of a microwave diode attached via microdot cable to a small coupling loop inserted within the tank. This was calibrated in the same manner as the neon bulb resistance. Results gave $Q_o \sim 1500$.

Both the neon bulb resistance method and the coupling loop output method are subject to the criticism that their insertion severely perturbs the vacuum field. Much of the perturbation would come from the lead wires necessary for measurement. Two alternative methods were suggested to obtain a local measurement without leads. First, a neon bulb stripped of its external leads was mounted on a teflon (low loss) rod. The idea was to obtain the local microwave field as a function of bulb brightness. Unfortunately, though the bulbs glowed vigorously with their lead wires attached, they failed to turn on at all when re-inserted without the leads, even at the highest powers available.

A novel method was to monitor the color of encapsulated liquid crystals exposed to a microwave flux for a specific time. The particular sheets used were obtained from Edmund Scientific Co., and go through color changes from dark yellow to orange to green to deep blue as temperature is increased. Insertion of these liquid crystal sheets into a waveguide allowed prediction of color status with a known power. Insertion of the sheet had no effect on the transmitted power, unlike the neon bulb and coupling loop method, and indicated that these sheets had minimal

perturbative qualities. When placed within the DC Machine, no color change was observed after irradiation at the highest S-band powers available ($\sim$ 1 KW). This sets an upper limit of $Q_o < 3700$.

A non-perturbing, but non-local method of measuring Q is to have a variable frequency source sweep across cavity modes. Q is derived from the ratio $\frac{f}{\Delta f}$, where f is the center frequency and Δf is the full width of the half-power response of the mode. This method gives $Q_o \sim 3000$ to 3500. The higher Q_o is understandable if the earlier local measurements are, in fact, loading down the source. This is to be compared with the order of magnitude Q_o expected from the volume V, surface area S, and skin depth δ in the device:[10]

$$Q_{vac} \sim \frac{V}{\delta S} \sim \frac{.44\ m^3}{(1.7\times10^{-6}m)*(3.42\ m^2)} = 7.5 \times 10^4 .$$

Such Q values can not be approached because of extra surface area from probes, supports, and surface inperfections, and oxide layers that decrease conductivity and thus increase skin depth.

A common assumption is that the electric field in a plasma adjusts itself so that complete absorption of power occurs at the resonance zone. The relation between resonance density and power absorption is given in section 7.3.

Table 2.1

Basic Facts about the DC Machine

Material	5083-H112 Aluminum
Main Tank	(see note i)
Volume	.439 m^3
Surface Area	3.155 m^2
Length	.66 m
Inside Radius	.46 m
Outside Radius	.474 m
West End Extension	
Volume	5.23×10^{-3} m^3
Surface Area	.151 m^2
Length	.31 m
Inside Radius	.055 m
Outside Radius	.0637 m
East End Extension	(see note ii)
Volume	3.85×10^{-3} m^3
Surface Area	.118 m^2 w/o Lisitano Coil .147 m^2 w/Lisitano Coil
Length	.25 m
Inside Radius	.0375 m
Outside Radius	.0382 m
Total Volume	.4405 m^3 (see note iii)
Inside Surface Area	3.42 m^2 (see note iii)

NOTES

(i) Internal ring and supporting structures ignored.

(ii) Values apply to times before Aug. 28, 1980; afterwards an extension identical to the the west end was attached to the DC Machine.

(iii) Diffusion pump channel ignored, but not internal ring structure.

Table 2.2

Density and Measured Pressure in the DC Machine

Gas	Listed S	Adjusted S	Tank Pres./ Foreline Pres. (1)	(2)	True Pres./ /Themocouple Guage reading
H_2	.44	.69	1.93×10^{-6}	3.56×10^{-6}	.62
He	.17	.27	1.51×10^{-6}	3.05×10^{-6}	1.06
air	.96	1.56			1.13
Ar	1.38	2.15	1.52×10^{-5}		1.83

Notes

(i) Values in column 1 apply when the diffusion pump gate valve is fully open.

(ii) Values in this column 2 apply then the diffusion pump gate valve is cracked slightly open, enough for a 1" diameter rod to be inserted in the elbow joint.

(iii) Listed sensitivity values, S, are taken from references 11-14.

Table 2.3

DC Coil Characteristics

	End Coils	Helmholtz Coils	Internal Ring
Mean coil radius	.127 m	.565 m	.33 m
Distance to midplane	.554 m	.283 m	0 m
Effective no. of turns	100	72	12
Coil Resistance (Ω)	.058 (East) .063 (West)	.149	.00345
Maximum current (A)	280	400	1800
Inductance* (mH) (calculated for 0 Hz)	4.51	22.5	.166
(measured at 1 KHz)	.98	1.5	.015

*Note. The discrepancy between calculated and measured inductance values is that the calculated inductance does not take into account the metal walls of the device interior to the coil turns. This means much less area for magnetic flux at higher frequencies, and hence less inductance.

Figure 2.1 DC Machine.

A--Lisitano source

B--S Band waveguide

C--End Coils

D--Helmholtz Coils

E--Internal Ring

F--Liquid N_2 cold plate

All dimensions are in centimeters.

Figure 2.2 DC Machine magnetic field in simple mirror configuration.

I_e = 200 A I_h = 250 A I_r = -800 A.

Figure 2.3 DC Machine magnetic field in field reversed mirror configuration. I_e = 200 A I_h = 250 A I_r = -1600 A

Figure 2.4 DC Machine magnetic field with zero ring current.

I_e = 200 A I_h = 250 A I_r = 0 A

Figure 2.5 DC Machine magnetic field with strong positive internal ring current.

I_e = 200 A I_h = 250 A I_r = 1600 A

In figures 2.2 through 2.5 E, H, and R mark the end coils, Helmholtz coils, and internal ring, respectively. These carry currents I_e, I_h, and I_r, respectively Only the upper half of the DC machine is shown. The solid lines are flux surfaces. The notation used for labels is of the form n (-m), which means that the surface encloses $\frac{1}{2\pi} * n \times 10^{-m}$ webers. The dashed lines are mod-B surfaces. The units of the numbers on these lines are gauss.

Figure 2.6 Magnetic fields along the axis of the DC Machine.

2.6a Field reversed mirror configuration.

2.6b Simple mirror configuration.

Figure 2.7 Components of S-band Microwave System.

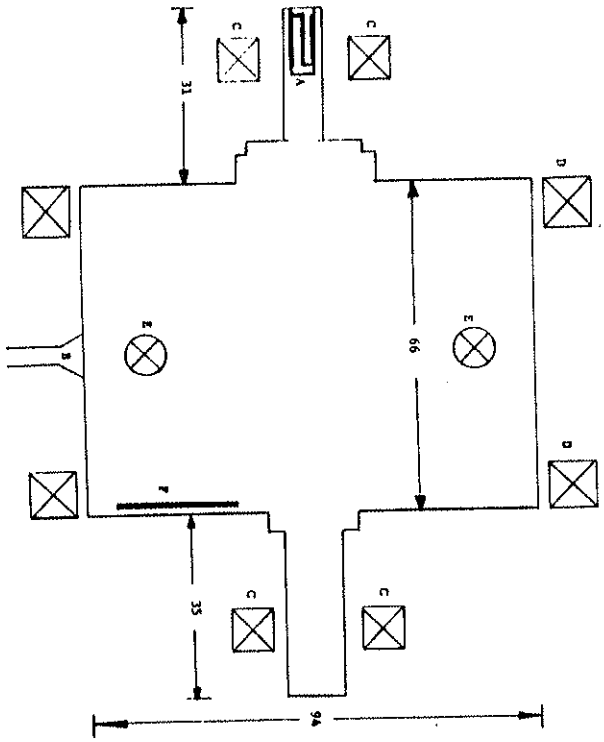

FIGURE 2.1
DC MACHINE

Figure 2.2 DC Machine magnetic field in simple mirror configuration.

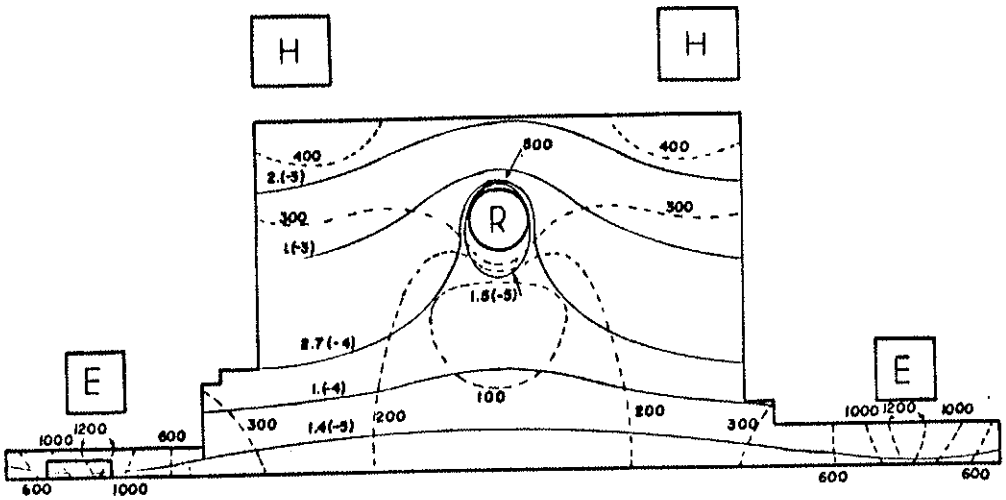

Figure 2.3 DC Machine magnetic field in field reversed mirror configuration.

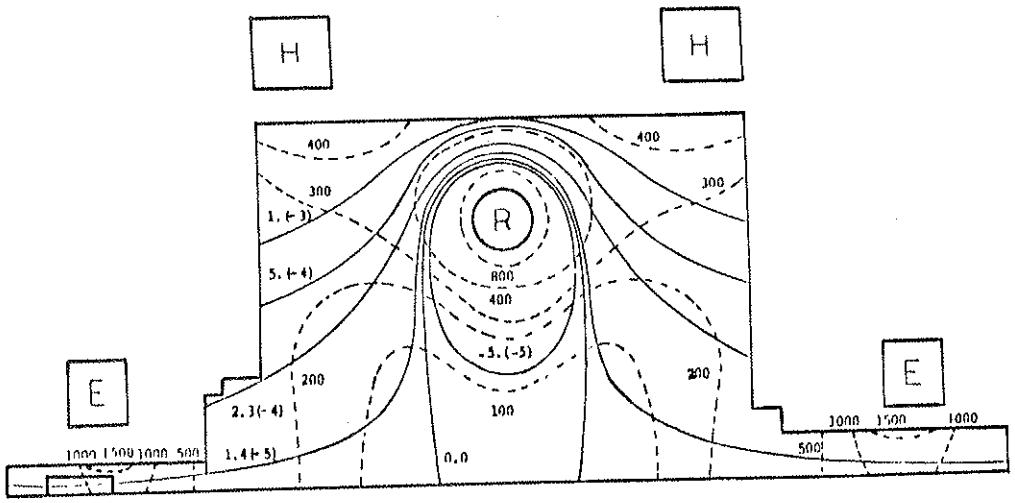

Figure 2.4 DC Machine magnetic field with zero ring current.

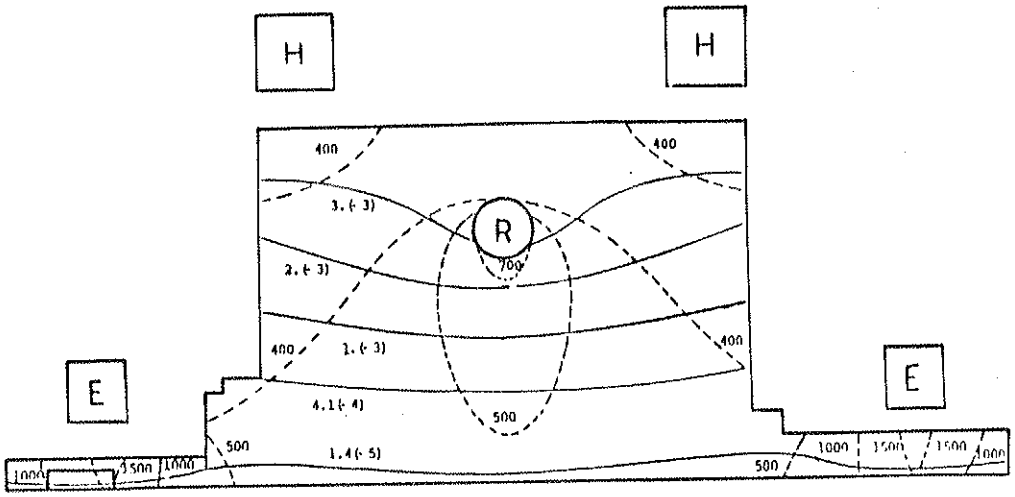

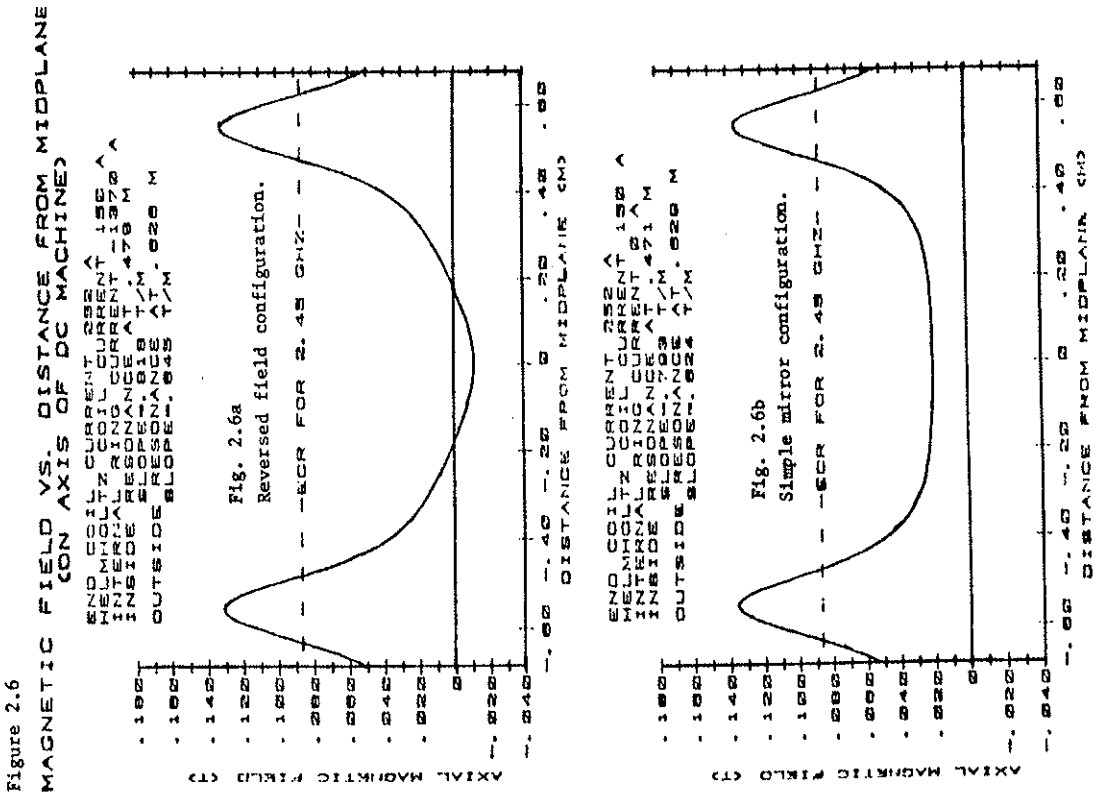

Figure 2.6

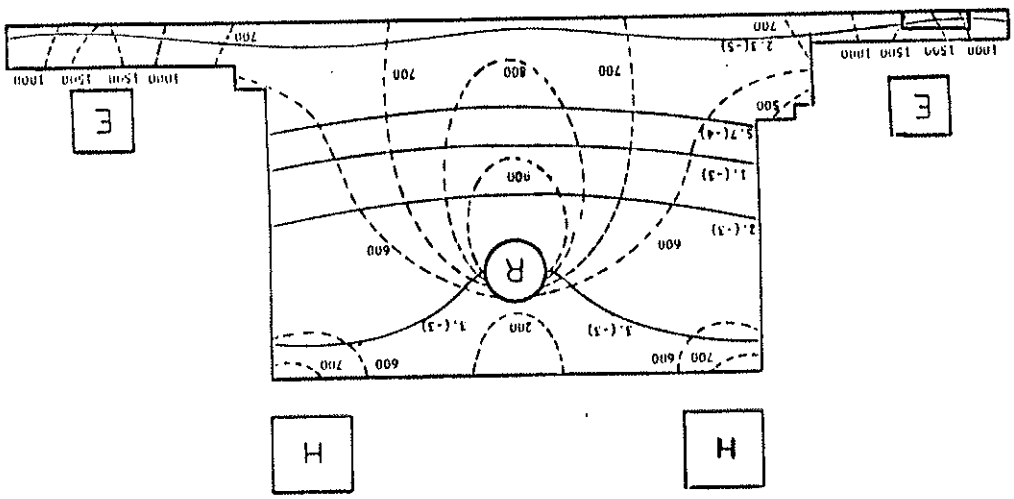

Figure 2.5 DC Machine magnetic field with strong positive internal ring current.

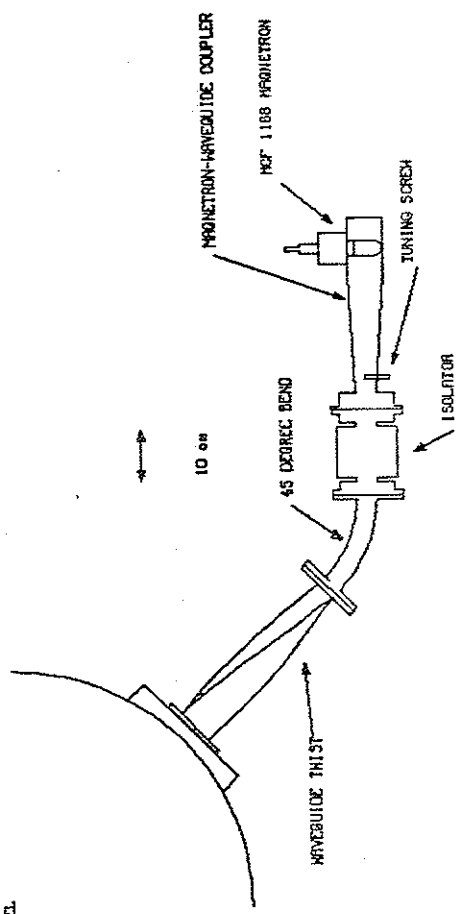

FIGURE 2.7 COMPONENTS OF S-BAND MICROWAVE SYSTEM.

REFERENCES AND NOTES FOR CHAPTER 2

[1]T. C. Jernigan, Ph. D. Thesis, University of Wisconsin, Madision (1971).

[2]R. Prater, Ph. D. Thesis, University of Wisconsin, Madison (1971).

[3]R. K. Richards, Ph. D. Thesis, University of Wisconsin, Madison (1976).

[4]C. M. Strawitch, Ph. D. Thesis,

University of Wisconsin, Madison (March, 1981).

[6]In the DC Machine the ratios of main tank pressure (in torr) to foreline pressure (in microns) are 1.56×10^{-6}, 1.12×10^{-6}, 7.5×10^{-6}, and 1.6×10^{-5} for H_2, He, air, and Ar, respectively.

[7]G. Lisitano, Proceedings of the Seventh International Conference on Phenomena in Ionized Gases, Vol. 1, (Beograd: Gradevinka Knjiga Publishing House, 1966) p. 464-467.

[8]A. Roth, Vacuum Technology, (American Elsevier, New York, 1976) p. 283.

[9]J. C. Sprott and K. A. Conner, in Plasma Instabilities and Waves Excited by an Anisotropic Energy Distribution Produced by Electron Cyclotron Resonance, Quarterly Progress Report 13, (June 15, 1970), p. 23.

[10]T. Moreno, Microwave Transmission Design Data, (Dover Publications, New York, 1958), p. 215.

[11]A. Guthrie, Vacuum Technology, (John Wiley & Sons, Inc., New York, 1963), p 52.

[12]S. Dushman and A. H. Young, Phys. Rev. 68, 278 (1945).

[13]S. Wegener and C. B. Johnson, J. Sci. Instrum. 28, 278 (1951).

[14]G. J. Schulz, J. Appl. Phys. 28, 1149 (1957).

[15]R. A. Breun, Ph. D. Thesis, University of Wisconsin, Madison, (PLP 634, June 1975), p.124.

[16]L. Holland, W. Steckelmacher and J. Yarwood, eds., Vacuum Manual, (E. F. Spon, London, 1974).

Chapter 3. Diagnostics

Experimental data in plasma physics takes on the idiosyncrasies of whatever technique is used for measurement. In many cases erroneous values might be obtained if data were not interpreted with care. In this chapter details are given about the principle methods used in the present experiment to obtain values of plasma variables.

3.1 Langmuir probes.

The bulk of data in this thesis was obtained by Langmuir probes. The Langmuir probe is a simple device---an electrode for which the current is monitored as a function of voltage. The theory and interpretation of the data obtained can be complex, however, as evidenced by the voluminous literature on the subject. References 1 through 4 provide a general review of the theory and use of Langmuir probes.

In the present series of experiments the emphasis was on measuring the plasma potential, V_p. The technique for extracting this value from raw data deserves attention. For an ideal planar probe in a Maxwellian plasma the electron current increases exponentially as the probe bias V is increased, up to the plasma potential, after which the current stays constant at the "electron saturation current". For such a curve (as in figure 3.1a) there is no problem in picking V_p, since it is just the point of sharp transition from rising current to steady current.

In the plasmas studied here, this simple picture fails. There is no true electron saturation current. Instead a a more or less smooth transition, or "knee", exists from the exponential region to the "saturation" region. In the "saturation" region the current increases at an ever slower rate with increasing bias. (See figure 3.1b). The causes of the deviation from the ideal curve may be plasma potential fluctuations, magnetic field effects, a non-Maxwellian plasma, or variation of the work function over the surface of the probe.

Even in a collisionless, steady-state, non-magnetized Maxwellian plasma and for an ideal collecting probe, Laframboise[5] has shown that the onset of electron saturation is always gradual for a spherical probe whenever $\rho = \frac{r}{\lambda_D} = \frac{\text{probe radius}}{\text{Debye length}}$ is not large compared with unity. Thus the picture of a sharp knee is not always justified even for an ideal plasma.

There has been some controversy in the probe literature about which part of the knee to use for V_p. Some workers[2,6,7] have used the potential which is at the intercept of the curves of tangency to the linear "saturation" region and that of maximum slope, as in figure 3.2. One difficulty with this is that the "saturation" regime may not be linear. For a plasma with a large λ_D, Chang and Laframboise[8] argued for using the bias of the maximum of the second deriviative of the electron current as V_p. However, this has been disputed by Shimizu and Dote.[9] Vorobeva, et. al.[10] also used the bias of maximum second deriviative for V_p. A subsequent

test by Milenin[11] using the noise characteristic method, found that the maximum of the first deriviative (zero of the second deriviative) was more in accord with V_p, however. Virmont and Godard[12] also found that for a spherical probe in a Maxwellian plasma, the inflection point was very close to the plasma potential. Ludkovnikov and Novgorodov[13] studied non-Maxwellian plasmas and found that even in these plasmas best consistency with known values of temperature and density occurred with the inflection point of the IV curve taken as V_p.

In view of the fact that the inflection point of the IV curve is a unique point, is consistent with ideal planar theory, and has been relatively well accepted as the location of V_p, the inflection point was used for V_p for results obtained from Languir probes in this thesis. There is no evidence of plasma drift, which could invalidate this result.

Another common practice is to use the plasma potential obtained from the floating potential, V_f, and the electron temperature, T_e. For an ideal Langmuir probe, for which the probe size is large compared with λ_D, and $T_e > T_i$, the plasma potential is calculated readily from the relation:

$$V_p = V_f + \frac{kT_e}{e}\frac{1}{2}\ln\left(\frac{m_i}{2m_e}\right) \qquad (3.1.1)$$

where m_e is the electron mass, and m_i is the ion mass. The use of this formula avoids the uncertainty associated with the extended

"knee", since V_f and T_e are comparatively well defined. However it should be pointed out that this is not a measurement of V_p, but rather an application of simple probe theory. It assumes, for example, that the ions are driven to the probe by a sheath potential of ~ .5 $\frac{kT_e}{e}$. In the present study, use of equation (3.1.1) yielded V_p values that were consistently too high. This is primarily because of the effects of the magnetic field, which reduces the electron current to the probe much more than the ion current. For particle collection across the magnetic field the reduction factor is approximately[2] $(1 + \omega_c^2\tau^2)^{-1}$, where ω_c is the cyclotron frequency and τ is the mean collision time. The value of ω_c makes this factor significantly smaller than unity for electrons, but hardly different from unity for ions.[1] A more detailed analysis by Sugawara[14] indicates that the parallel electron flux is also reduced. Figure 3.3 shows representative values of $\alpha \equiv \frac{e(V_p-V_f)}{kT_e}$ measured during the present investigation as a function of magnetic field strength B. Not only are the values well below those expected from simple probe theory, but it is clear that α depends on what type of probe is being used. Researchers that have used (3.1.1) as the basis of their plasma potential values are thus in error, up to an electron temperature or even more.

It was also necessary in some experiments to know the value of plasma density, n. For a planar probe in a homogeneous, infinite, unmagnetized plasma this amounts to measuring the flat "ion saturation current", I_{isat}. Unfortunately, the normalized

ion current curves of Laframboise[5] show that a relatively constant "ion saturation current" cannot be expected unless $\frac{r}{\lambda_D} \to \infty$. It is possible to take the graphical data of reference 5 and derive relatively simple analytical expressions for the normalized value of I_{isat}.[15] However, the results of such effort are not self-consistent when the measured values of the plasma are substituted; the slope ion saturation curve indicates a different value of density than the absolute level of the current. Possibly this is due to magnetic field effects, which were ignored in the treatment of Laframboise[5]. Brown, Compher, and Kunkel[16] investigated the ion current in a magnetoplasma and compared the results with that of microwave interferometry. They found that the best choice of "ion saturation current" occurred when the point at the transition between the linear part and the exponential part was used. Since their IV plots resemble those of this study, this rule was used for obtaining I_{isat} values for density determination. (See Fig. 3.4). If $\frac{kT_e}{e}$ is the electron temperature in eV, A_p is the probe area in m^2 and the I_{isat} the ion saturation current in amperes, the density n in m^{-3} is

$$n = 1.6 \times 10^{15} \frac{I_{isat}}{A_p} \left(\frac{kT_e}{e}\right)^{1/2}. \qquad (3.1.2)$$

It was frequently useful to examine IV traces on an oscilloscope during the course of an experiment. Figure 3.5 shows the set-up used for this. A second scope is use to obtain an adjust-

able, high-linearity sweep of bias with time. This is required if the slope of the current, and thus the plasma potential, is to be determined electronically. Figure 3.6 shows typical resulting scope traces, with superimposed current deriviatives. Details of other IV display-and-analysis circuitry are given in references 17-26.

With the complete IV trace, information on density and mean electron energy can be deduced even if the electron distribution function is not Maxwellian.[27] For most IV graphs, however, an exponential region, characteristic of a well defined electron temperature, was apparent. Since the magnetic field does not affect the T_e value obtained with Langmuir probes,[14,28] the values obtained by taking the best linear fit on a semi-log plot are reliable.

There were usually no difficulties in getting a good value for the floating potential, V_f. Occasionally the plasma properties drifted with time, so that repeated scans were used to insure that the data were self-consistent.

To facilitate the analysis of IV plot data, computer programs were written. These were the Basic program IVGEN, designed for the PDP-11 computer, and the Fortran program IVAN, written for use on the NMFECC Cray-1 and CDC 7600 computers. Input consisted of a series of (V,I) pairs for each case. A least squares fit was used to find T_e. A cubic fit was used on the 4 points in the region of greatest slope to find the inflection point, which was used for

V_p. The rule of Brown, Compher and Kunkel[16] was used in obtaining a value of I_{isat}, as in figure 3.4.

3.2 Emission probes.

The potential difference between the plasma and an immersed electrode affects the ability of that probe to emit, as well as collect, electrons. This forms the basis for "emitting probes", in which the probe is held at a hot enough temperature ("T_w"), so that a measurable emission current can occur if the relative bias permits. This is actually quite an old idea, proposed by Langmuir[29] along with collecting probes.

The use of emission probes has historically fallen into one of two categories: swept probes[30-32], in which the probe bias is changed as with a regular Langmuir probe; and floating probes[32-36], in which the bias of the emitting probe is allowed to adjust itself so that the net current to the probe is zero.

In the swept bias method, the plasma potential is taken as that point at which the effect of emission becomes noticeable. Often several sweeps are made at different probe temperatures (accomplished by making the probe a filament and adjusting the heating current though it), so that the divergence of the set of curves from the cold probe values becomes clear, as shown by Chen.[30] At probe bias $V > V_p$, emitted electrons are pulled back to the filament and the net electron current is due to the collected current only, and has the same value as for the cold probe. For

negative probe bias, $V < V_p$, the emitted electrons leave the probe region and contribute current. Some researchers[31,32] have differentiated the emission probe IV trace electronically, in an effort to pin down the V_p value more precisely.

When the emission current is made to be of the same order of magnitude as the collected electron current, the emission probe will have a floating potential ("V_{fe}") very close to that of the plasma potential,[32] as shown in figure 3.7. These data were obtained by placing a cylindrical insert into one of the end extensions of the DC Machine, open to the plasma only by a screen. By varying the bias of the insert, which enclosed the probe, the local plasma potential could be independently varied.

Emission probe behavior can be explained by considering the idealized system of an emitting planar probe of saturated electron emission I_{eo} in a plasma where the electron saturation current is I_{co}. Ion current is at least an order of magnitude smaller than I_{co}, and will be neglected. Space charge effects are also neglected. If the probe is positive with respect to the plasma, the collected electron current will be I_{co} and the emitted current will be reduced by the factor $\exp[-\frac{eV}{kT_w}]$, since the emitted electrons have a Maxwellian distribution of temperature T_w. V is the bias relative to the probe. For a floating probe the two currents must be equal, and thus the emissive floating potential V_{fe} takes on the value

$$V_{fe} = \frac{kT_w}{e} \ln \left(\frac{I_{eo}}{I_{co}}\right) \qquad (3.2.1)$$

If the probe is negative with respect to the plasma, all emitted electrons escape to the plasma, but the incoming electron current is attenuated by the Boltzmann factor $\exp[\frac{eV}{kT_e}]$, where T_e is the electron temperature inside the plasma. In this case the floating potential is

$$V_{fe} = \frac{kT_e}{e} \ln \left(\frac{I_{eo}}{I_{co}}\right) \qquad (3.2.2)$$

When the saturated emission current is greater than the saturation collection current, (but not too much greater), the probe floats on the order of $\frac{kT_w}{e}$ volts above the plasma potential. For an emitting probe this is < 0.2 volts, small compared with variations in the plasma potential in the mirror and with the width of the "knee" region of standard Langmuir probes. Thus the use of emission probes can provide greater accuracy as well as the advantage of a direct reading.

Chen[30] worried that in this method the V_p value deduced could be in error as a result of emitted electrons building up a space charge sheath about the probe. A form of the Child-Langmuir law would then limit the use of emission probes in high density plasmas where large emission currents are needed. In a plasma with relatively cold ions, it appears that the space charge sheath is in large part counteracted by ion trapping.[37] Efforts at a

self-consistent treatment of emission probes where space charge is important have thus far been rudimentary.[32]

The emission probes used in the this series of experiments had a well defined V_{fe} plateau as filament voltage (thus filament current and kT_w) were increased.[37] This permits the use of the floating method, which involves less elaborate circuitry and gives a direct reading of V_p. To prevent the voltage drop across the filament from interfering with potential measurements, the 60 Hz heating current was rectified by the addition of a diode. Readings were taken during the time that no current flowed, so that the entire filament was at the same potential. V_{fe} drooped somewhat as the filament wire cooled during the $\frac{1}{120}$ second off-time, but this was not a serious problem. Makowski[38] devised a procedure to find V_p from the size of this droop.

Though the V_p values obtained by observing V_{fe} from an emissive probe agreed quite well with V_p as given by inflection point of the IV trace of a cold probe, the emission probe data values derived from emission probe data were better defined. The filaments used for most experiments were of tungsten, taken from a TS311 bulb, rated at 10 volts. To get good emission it was necessary to use a filament voltage well above the rated value. Initially filaments from smaller voltage bulbs were used, but they were abandoned because they tended to burn out after only a short useful life in the plasma. Good results were also obtained from a low-resistance filament (~ 2 cm of 5 mil diameter thoriated tungsten wire). In the floating regime, the AC heating voltage was small compared with the DC signal. This permitted a direct read-out on a DMM or display on an X-Y plotter without the necessity of a sample/hold circuit.

For the floating emissive probe method to give satisfactory results, it is important to make sure that the plateau voltage associated with high emission has been reached. The circuit shown in figure 3.8 allows display of floating potential versus heating bias. Figure 3.9 shows a resulting plot. The two levels—cold floating potential and the hot plasma potential plateau are clearly apparent. Because the expected floating potential has a dependence on the plasma density and magnetic field strength through the electron saturation current, it is risky to take the floating potential of an emissive probe with a fixed heating bias as the plasma potential where n and B are known to vary considerably.[37] The swept heating bias arrangement of figure 3.8 overcomes this problem, and has the subsidiary benefit of retaining a large emissive capability, which is observed to decrease if a filament is continuously operated at high emission.

3.3 Noise probes.

It is sometimes possible to find V_p by examination of the plasma noise current to a probe as a function of bias.[11,39-47] One explanation of why this works regards the plasma as a noise generator, separated from the probe by the sheath resistance. When the probe bias is equal to the plasma potential, the sheath disappears, and the full amplitude of the fluctuations is felt by the probe. This qualitative account has been used to justify allegedly successful attempts at getting V_p in discharge tubes and in the ECRH plasma of CIRCE at Saclay, France.[11,40,42,43,47]

It is also possible to justify the noise probe method by considering oscillations on the DC probe characteristic curve. If δV_i is the oscillitory voltage within the plasma, then the amplitude of the probe current fluctuation for bias V is

$$\delta I = \frac{dI}{dV}\Big|_V \delta V_i \qquad (3.3.1)$$

δI is greatest where $\frac{dI}{dV}\Big|_V$ is at a maximum, namely at $V = V_p$. This method then is not fundamentally different from taking the inflection point as V_p. One merely lets the self-oscillations of the plasma define the local deriviative of the IV trace. Richards, et. al.[44] found an extremely close fit between relative noise current and the first deriviative value. This was also true of the DC Machine plasmas. The noise vs. bias curves were qualitatively similar to that found by Fujita[41] on the Etude

device. Probe noise increases up to the limit set by power supplies (~ 100 V). The noise frequency spectrum is dominated by low frequency (< 10 KHz), as determined from a Tektronix 1L5 Spectrum analyzer. Oscillation magnitudes should decrease as the adjustment time of the probe sheath is approached. This is roughly the transit time of an electron of thermal speed v_e across a Debye length:

$$\tau_a \sim \frac{\lambda_{De}}{v_e} = \left(\frac{\varepsilon_o kT_e}{ne^2}\right)^{\frac{1}{2}} \left(\frac{kT_e}{m_e}\right)^{-1/2} \qquad (3.3.2)$$

$$= \left(\frac{\varepsilon_o m_e}{ne^2}\right)^{\frac{1}{2}} = \omega_{pe}^{-1}$$

For a typical DC Machine plasma $n < 10^{16}$ m^{-3}, so that $f_{pe} < 900$ MHz. The high range of frequencies was measured with a Hewlett Packard Model 851B spectrum analyzer over the range .01-10 Ghz. Little noise was picked up at the higher frequencies.

When plasma noise is excessive, the apparent floating potential is reduced. This is a separate topic and is taken up in section 6.6.

3.4 Gridded Energy Analyzers.

Figure 3.10 shows an energy analyzer used to determine the mean ion energy. The device was mounted on one of the end plates. In this position it is a non-perturbing device, for any particle reaching it would be lost to the wall anyway. Multi-grided probes

have been extensively used in the past. References 48-50 give a background on their theory and use.

Energy analyzer data indicates that T_i is 2-5 eV. This is in contrast with the He II 4686 Å line-broadening study of Fonck and Guss,[51] in which a null result was interpreted as evidence that T_i < .06 eV. It should be noted that other ECRH experiments have found $T_i \sim (.1\text{-}.5) \times T_e$.[52,53]

It is difficult to devise an explanation for the observed ion current behavior without invoking ions with at least a few eV of thermal energy. The most obvious alternative is to account for the dispersion in parallel energy as a result of ionization at positions of different plasma potential. The current in this explanation can be deduced from assuming quadratic variation of plasma potential $\phi \sim \phi_o(1-\alpha z^2)$ and magnetic field $B \sim B_o(1+\beta z^2)$ near the midplane, with the electron density given by a Boltzmann factor, $n_e = \exp(\frac{e}{kT_e}(\phi-\phi_o)) \equiv \exp(-\eta)$. Then a detector at the position where the magnetic field is B_d, with retarding potential ϕ and collection area A_d, should collect ion current

$$I = C \int_0^{\Upsilon} \frac{e^{-\Upsilon}\, d\Upsilon}{\sqrt{\Upsilon\,(1+\kappa\Upsilon)}} \qquad (3.4.1)$$

where $C \equiv \dfrac{e\, n_g \langle\sigma v\rangle_{ion} A_d B_d}{2 B_o \sqrt{\alpha}(\frac{e\phi_o}{kT_e})^{1/2}}$ and $\kappa \equiv \dfrac{\beta}{\alpha}(\dfrac{e\phi_o}{kT_e})^{-1}$.

In (3.4.1) n_g is the ionization rate. To first order in κ, (3.4.1) becomes

$$I = C\,\{(1-\tfrac{\kappa}{2})\sqrt{\pi}\,\mathrm{erf}(\sqrt{\Upsilon}) + \kappa\sqrt{\Upsilon}\,e^{-\Upsilon}\} \qquad (3.4.2)$$

Figure 3.11 compares the expected current from the cold ion model with the Maxwellian model. The normalized bias is $\frac{kT_e}{e}$ for the Maxwellian (thermal) model. It is Υ for the free-fall model. The normalized bias for the experimental cases is found by taking the voltage range over which the probe current falls from e^{-1} of its asymptotic value to e^{-2} of that value. Plotted in this way, the experimental traces agreed well even though the values of T_i and ion saturation current are different in each case. The curve is clearly exponential for large retarding biases. For low retarding bias, the curves gradually approach a limit, somewhat like the free fall model, suggesting some admixture of low energy free-fall ions.

Figure 3.1 Ideal and actual Langmuir plots.

3.1a Ideal IV characteristic for an argon plasma with T_e = 8 eV, V_p = 15 V, and I_{e-sat} = .155ma

3.2a Tracing from an actual IV plot with the same plasma conditions.

Figure 3.2 Intercept method of determining V_p.

V_p and V_f indicate the plasma potential and floating potential, respectively, on this generalized plot. Best linear fits are taken to the steep part of the plot and the electron saturation region. The bias at which the curves intercept is taken as V_p.

Figure 3.3 Values of $\alpha \equiv \frac{e(V_p - V_f)}{kT_e}$ vs. magnetic field strength B for Helium.

+ —— values for a tungsten filament probe.

0 —— values for a 1.22 mm diameter spherical tip probe.

Figure 3.4 IV Plot showing location of "ion saturation current". I_A is taken as the saturation level.

Figure 3.5 Circuitry used for displaying IV trace on oscilloscope.

R1 = 100Ω, C1 = 1 μF, R2 = 20kΩ, C2 = .0025μF.

CH1, CH2: Channels 1 and 2 on 1A1 Tektronix Plug-in.

The isolation transformer on the power line side of the 555 scope makes it possible to float that scope electrically. This allows use of the adjustable, high linearity sawtooth output as a probe driver. High linearity is important so that the $\frac{dI}{dt}$ output of the differentiator circuit is proportional to $\frac{dI}{dV}$.

Figure 3.6 Sample IV Traces taken with the circuit of figure 3.5 A sequence of plots spanning the resonance zone is shown. Plasma potential, floating potential, and electron temperature are noted on each.

Figure 3.7 Comparison of V_p values obtained using the IV inflection point and the floating emissive potential.

The plasma potential was adjusted by varying the bias of a large metal vessel surrounding the probe. The same filament was used to obtain both data values.

Figure 3.8 Circuit for obtaining floating emissive potential as a function of heating bias.

Figure 3.9 Floating emissive potential vs. heating bias for a typical case.
The data were taken with the circuit of figure 3.8. The IV inflection bias is shown on the far right.

Figure 3.10 Energy analyzer used for T_i measurement.

Figure 3.11 Comparison of experimental data points with the thermal and free fall models.
case 1—1.7×10^{-5} torr He I_e=220, I_H=205, I_r=-774, T_i = 4.75 eV
case 2—1.7×10^{-5} torr He I_e=220, I_H=205, I_r=-774, T_i = 4.2 eV
case 3—2.1×10^{-5} torr He, I_e=221, I_H=205, I_r=-775, T_i = 3.8 eV
case 4—3.2×10^{-5} torr He, I_e=220, I_H=205, I_r=-775, T_i = 5.6 eV

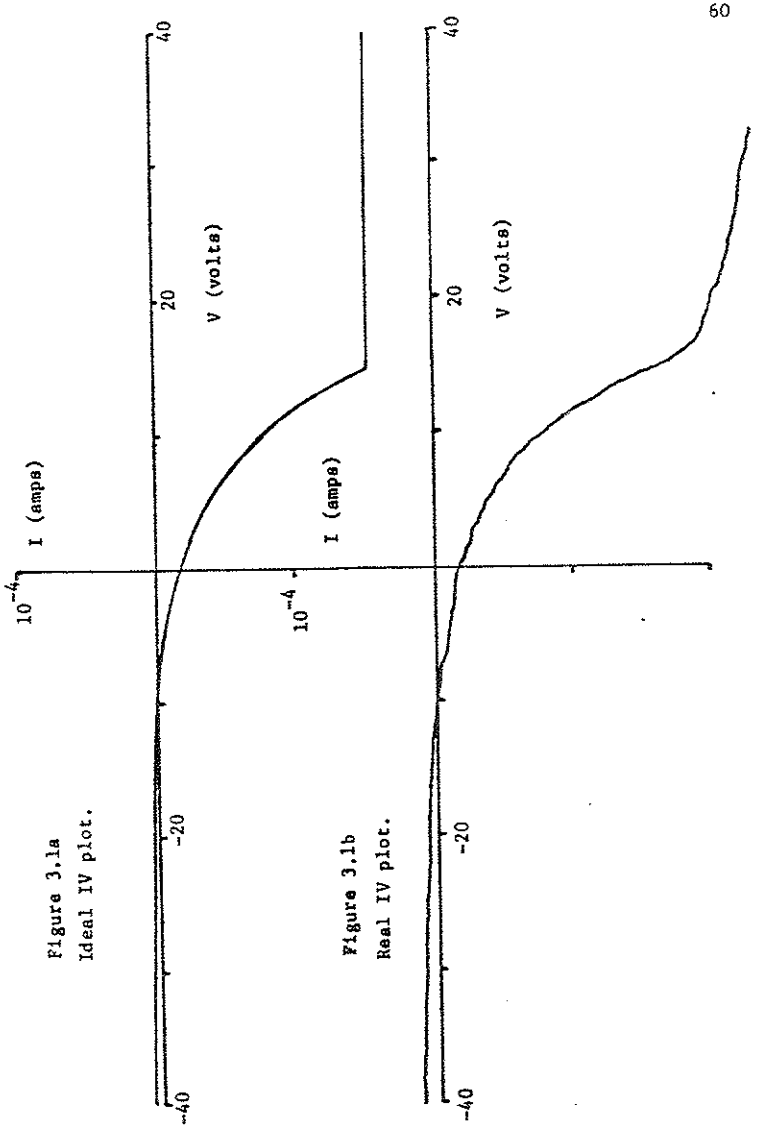

Figure 3.1a
Ideal IV plot.

Figure 3.1b
Real IV plot.

FIGURE 3.2

Intercept method of extracting V_p from an IV trace.

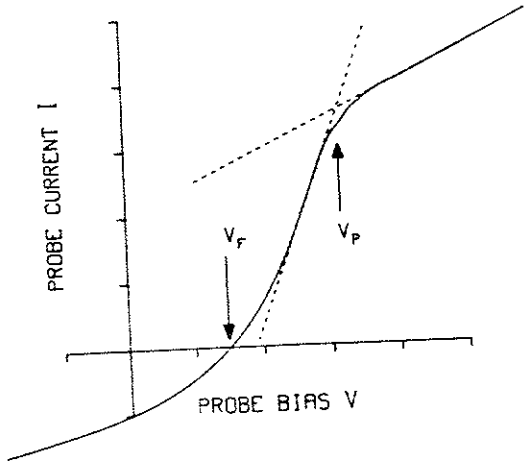

Figure 3.3 $\alpha = e(V_p - V_f)/kT_e$ vs. magnetic field strength.

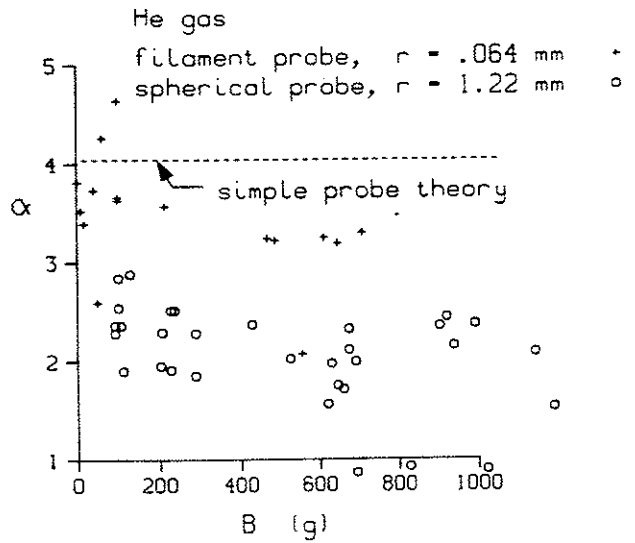

FIGURE 3.4 IV PLOT SHOWING LOCATION OF "SATURATION CURRENT".

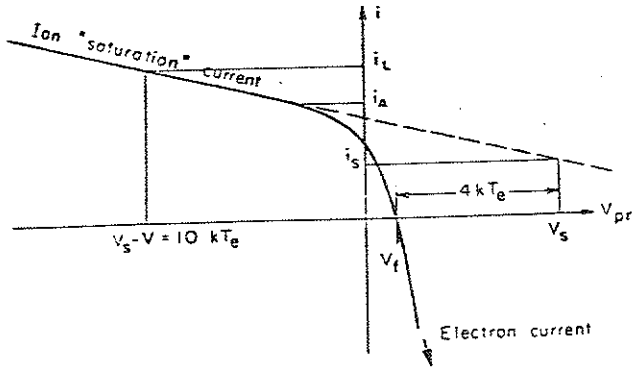

I_A TAKEN AS THE SATURATION LEVEL; WHERE LINEAR REGION JOINS EXPONENTIAL REGION.

GRAPH TAKEN FROM REFERENCE 16.

Figure 3.5 Circuitry used to display IV trace on oscilloscope

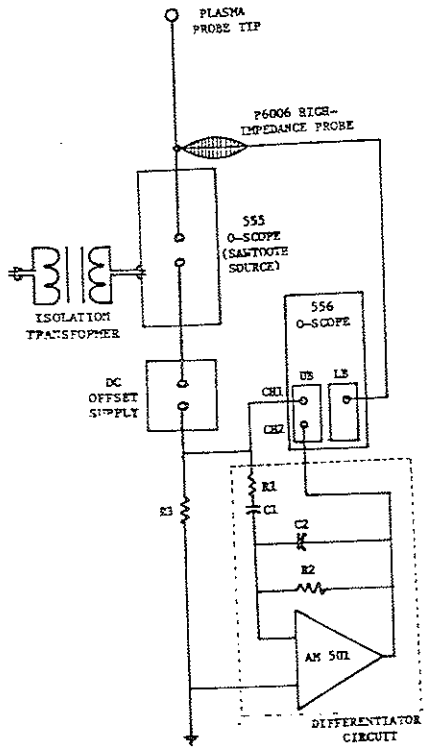

Figure 3.6 IV traces obtained using the circuitry of figure 3.5.

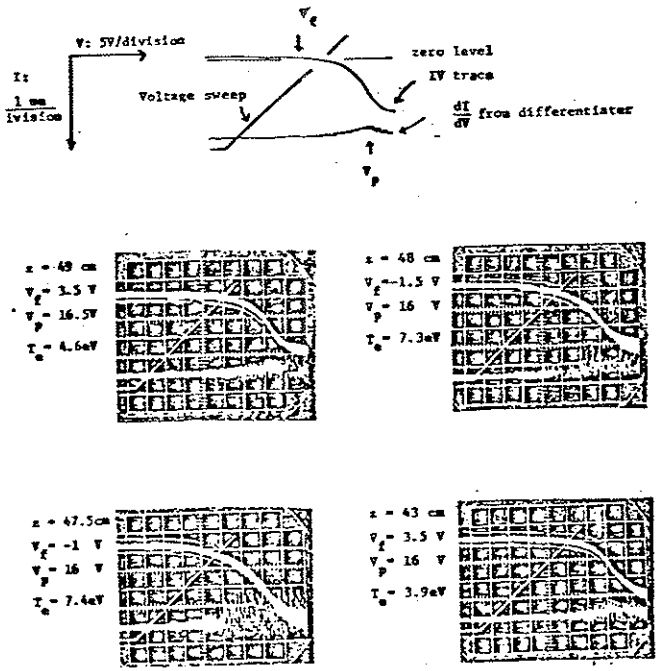

Figure 3.7 Relation between emissive probe floating potential and Langmuir probe inflection potential.

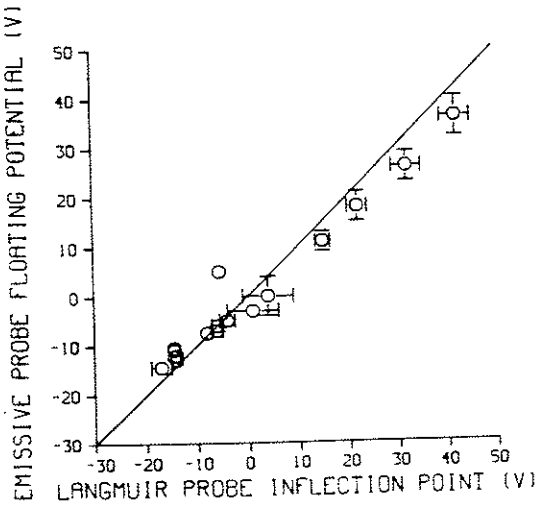

FIGURE 3.8 CIRCUIT FOR OBTAINING V_{FE} AS A FUNCTION OF HEATING BIAS.

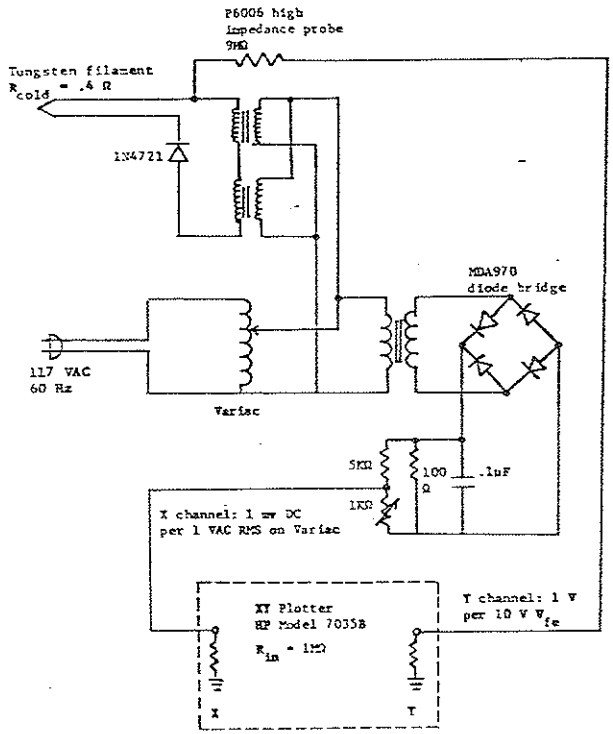

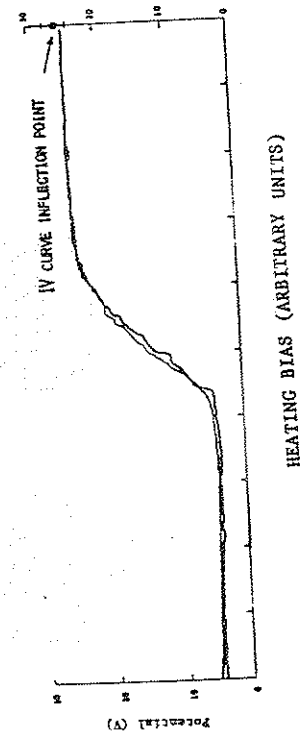

Figure 3.9 FLOATING POTENTIAL OF EMISSIVE PROBE VS. HEATING BIAS.

Figure 3.10 Details of gridded parallel energy analyzer.

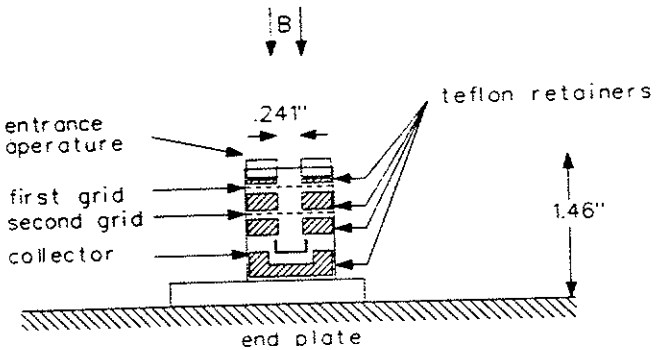

Figure 3.11 Gridded analyzer traces compared with thermal and free-fall models.

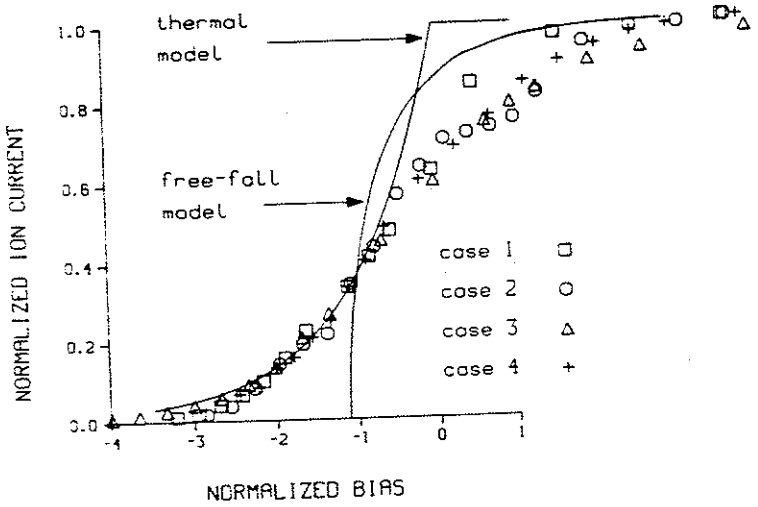

REFERENCES FOR CHAPTER 3

[1]J. D. Swift and M. J. R. Schwar, Electrical Probes for Plasma Diagnostics, (Iliffe Books, London, 1969).

[2]P. M. Chung, L. Talbot, and K. J. Touryan, Electric Probes in Stationary and Flowing Plasmas: Theory and Application, (Springer-Verlag, New York, 1975).

[3]F. F. Chen, "Electric Probes", Chap. 4 in Plasma Diagnostic Techniques, R. H. Huddlestone and S. L. Leonard, eds., (Academic Press, New York, 1965).

[4]R. H. Clements, J. Vac. Sci. Technol. 15, 193 (1978).

[5]J. G. Laframboise, Theory of Spherical and Cyllindrical Langmuir Probes in a Collisionless, Maxwellian Plasma at Rest, University of Toronto Institute for Aerospace Studies Report No. 100, (1966).

[6]A. J. Stamm, PLP 21, (1963).

[7]J. C. Sprott, PLP 88, (1966).

[8]J.-S. Chang and J. Laframboise, Phys. Fluids 19, 25 (1975).

[9]T. Shimizu and T. Dote, Phys. Fluids 22, 2250 (1978).

[10]N. A. Vorobeva, Y. Kagan and V. Milenin, Sov. Phys.-Tech. Phys 8, 423 (1971).

[11]V. M. Milenin, Sov. Phys.-Tech. Phys. 16, 634 (1971).

[12]J. Virmont and R. Godard, Plasma Phys. 14, 793 (1972).

[13]A. I. Lukovnikov and M. Z. Novgorodov, Sov. Phys.-Tech. Phys. 16, 1931 (1972).

[14]M. Sugawara, Phys. Fluids 9, 797 (1966).

[15]P. K. Smith, PLP 783, (1979).

[16]I. Brown, A. Compher and W. Kunkel, Phys. Fluids 14, 1377 (1971).

[17]D. R. Nordlung and O. P. Breaux, Rev. Sci. Instrum. 43, 248 (1972).

[18]W. D. Friedman, Rev. Sci. Instrum. 42, 963 (1971).

[19]W. L. Harries, Rev. Sci. Instrum. 39, 1294 (1968).

[20]D. J. Holly, T. W. Lovell, and J. C. Sprott, Rev. Sci. Instrum. 45, 947 (1974).

[21]J. C. Holmes and E. P. Szuszczewicz, Rev. Sci. Instrum. 46, 592 (1975).

[22]H. Jones and P. Saunders, J. Sci. Instrum. 37, 460 (1960).

[23]J. Lacoste and K. Dimoff, Rev. Sci. Instrum. 44, 1278 (1973).

[24]K. A. Milnes, et. al., IEEE Trans. Plasma Sci. PS-8, 124 (1980).

[25]J. F. Waymouth, J. Appl. Phys. 30, 1404 (1959).

[26]I. Alexeff and D. F. Howell, J. Appl. Phys. 40, 4877 (1969).

[27]M. J. Druyvesteyn, Z. Physik 64, 790 (1930).

[28] J. R. Sanmartin, Phys. Fluids 13, 103 (1970).

[29] I. Langmuir, Phys. Rev. 33, 954 (1929).

[30] F. F. Chen, "Electric Probes", Plasma Diagnostic Techniques, Chap. 4, (R. H. Huddlestone and S. L. Leonard, eds.), (Academic Press, New York, 1965).

[31] J. J. Schuss and R. R. Parker, J. Appl. Phys. 45, 4778 (1974).

[32] J. R. Smith, N. Hershkowitz, and P. Coakley, Rev. Sci. Instrum. 50, 210 (1979).

[33] C. R. Hoffmann and D. J. Lees, Plasma Physics 13, 689 (1971).

[34] R. F. Kemp and J. M. Sellen, Rev. Sci. Instrum. 37, 455 (1965).

[35] O. Biblarz and H. Derfer, J. Phys. Soc. Japan 29, 180 (1970).

[36] R. W. Motley, J. Appl. Phys. 43, 3711 (1972).

[37] P. K. Smith, PLP 879, (August, 1982).

[38] M. Makowski and G. Emmert, PLP 876 (August, 1982); PLP 882 (October, 1982).

[39] K. D. Asvadurov, I. A. Vasil'eva, and V. M. Torchinskii, Sov. Phys.-Tech. Phys 17, 166 (1972).

[40] T. Dote, J. Phys. Soc. Japan 24, 224 (1968).

[41] J. Fujita, MATT-743 (Princeton Plasma Physics Laboratory), (December, 1969).

[42] K. S. Golovanivskii, Sov. Phys.-Tech. Phys. 15, 1146 (1971).

[43] H. Ikezi, M. Fujiwara and K. Takayama, J. Phys. Soc. Japan 25, 1663 (1968).

[44] Yu. M. Kagan, N. B. Kolokolov, V. M. Milenin, and A. M. Mirzabekov, Sov. Phys.-Tech. Phys. 15, 1019 (1970).

[45] S. Kojima, K. Takayama and A. Shimauchi, J. Phys. Soc. Japan 9, 802 (1954).

[46] S. L. F. Richards, G. L. Lloyd and R. P. Jones, J. Phys. D 6, 695 (1973).

[47] A. A. Zaitsev, M. Ya. Vasil'eva and V. M. Mnev, Sov. Phys.-JETP 9, 1130 (1959).

[48] G. Navratil, Ph. D. thesis, University of Wisconsin, PLP 693, (1976).

[49] E. I. Dobrokhotov and I. N. Moskalev, Sov. Phys-Tech. Phys. 15, 808 (1970).

[50] R. Jones, Rev. Sci. Instrum. 49, 21 (1978).

[51] R. J. Fonck and W. C. Guss, PLP 584, (Sept., 1974).

[52] H. Ikezi, IPPJ-67, (May, 1968).

[53] M. Okabayashi, K. Chen and M. Porkolab, Phys. Rev. Lett. 31, 1113 (1973).

Chapter 4. Density and potential in the "cut-out Maxwellian" model

4.1 Introduction

In this chapter the density n(z) at axial position z is found as a function of the local magnetic field B(z), and the local plasma potential $\phi(z)$, using the cut-out Maxwellian method. The motivation for doing this is to find out what density profiles will co-exist with a given plasma potential profile. This has been done in special cases by Post[1], BenDaniel[2], and Yushmanov.[3] Recently Cohen[4] has applied a variation of this method which might be described as a "cut-out drifting Maxwellian" model.

Here the distribution function is assumed to be Maxwellian for the confined regions of velocity space and empty for the untrapped "cut-out" regions. The ratio of values of density obtained in this model to that of the loss-free Maxwellian are the Maxwellian weighted "trapped fractions" of velocity space. These will be used as a basis for predicting ϕ by the models of Chapter 5, since rates of scattering into the loss region are determined by the fraction of untrapped velocity space. Because some of the previously published results have been misleading,[5] and because it is desirable to include all cases in a single source for posterity, this chapter is devoted to the subject.

The assumption of negligible population of the cut-out regions is reasonable when the loss time, τ_ℓ, for particles in the cut-out region to leave the mirror, is short compared with the characteristic times for ionization, τ_i, and for scattering into the cut-out region, τ_s.

The criterion for confinement is whether or not the particle will penetrate the magnetic mirror (at $z = L$), assuming conservation of particle energy and adiabatic invariance of magnetic moment. The boundary between confined and unconfined velocity space is a hyperboloid with a shape determined by the local, midplane, and maximum magnetic fields (B, B_o, and B_L, respectively); and the corresponding plasma potentials (ϕ, ϕ_o, and ϕ_L). To simplify notation ϕ_o is defined to be zero for the rest of this chapter.

Three considerations allow determination of n(z) from the midplane velocity distribution:

1. As B increases, a magnetic flux tube gets smaller in cross section A(z). Since $A(z) = A(o)\,\frac{B_o}{B(z)}$, a weighting factor due to the magnetic field of $\frac{B}{B_o}$ is introduced.

2. The time a particle spends in a given length increment dz near z is $\frac{dz}{v_\parallel(z)}$. This introduces a weighting factor of $v_{\parallel o}/v_\parallel(z)$.

3. Particles which have turning points between the midplane and z do not contribute to n(z). The limits of integration over $v_{\perp o}$ and $v_{\parallel o}$ must therefore exclude such particles.

These more or less intuitive factors arise naturally when conversion is made between midplane velocity space variables and local velocity space variables.

An equivalent procedure is to express the distribution function in local velocity space variables--a Maxwellian with Boltzmann factor for electrostatic potential--and integrate over the confined part of local velocity space.

4.2 Density profile for a potential well.

For the potential well the velocity space diagram for the midplane is shown in Fig. 4.1. For this case $q\phi_L > q\phi > 0$, where q is the charge of the particle.

From conservation of particle energy,

$$\frac{1}{2} m v_{\parallel}^2 + \frac{1}{2} m v_{\perp}^2 + q\phi = \frac{1}{2} m v_{\parallel o}^2 + \frac{1}{2} m v_{\perp o}^2 = E \text{ (constant)} \qquad (4.2.1)$$

and adiabatic invariance of magnetic moment μ,

$$\mu = \frac{m v_{\perp}^2}{2B} = \frac{m v_{\perp o}^2}{2B_o} = \text{constant} \qquad (4.2.2)$$

the expression for parallel velocity at z is

$$v_{\parallel}^2(z) = v_{\parallel o}^2 - (\frac{B}{B_o} - 1) v_{\perp o}^2 - \frac{2q\phi(z)}{m} = v_{\parallel o}^2 - \frac{\Delta B}{B_o} v_{\perp o}^2 - \frac{2q\phi}{m} \qquad (4.2.3)$$

The particle mass is m, with $\Delta B \equiv B - B_o$, $\Delta B_L \equiv B_L - B_o$.

The boundary between the "confined" and cutout" regions of velocity space is found by setting $v_{\parallel}=0$ at z=L:

$$v_{\parallel o}^2 = \frac{\Delta B_L}{B_o} v_{\perp o}^2 + \frac{2q\phi_L}{m} \qquad (4.2.4)$$

The resulting midplane velocity distribution is

$$f_o(v_{\parallel o}, v_{\perp o}) =$$

$$n_* \left(\frac{m}{2\pi kT}\right)^{\frac{3}{2}} \exp\left[\frac{m}{2kT}(v_{\parallel o}^2 + v_{\perp o}^2)\right] \qquad \left(v_{\parallel o}^2 < \frac{\Delta B_L}{B_o} v_{\perp o}^2 + \frac{2q\phi_L}{m}\right)$$

$$= 0 \qquad \left(v_{\parallel o}^2 > \frac{\Delta B_L}{B_o} v_{\perp o}^2 + \frac{2q\phi_L}{m}\right) \qquad (4.2.5)$$

In (4.2.5), n_* is what the midplane density would be if the cutout regions were populated. T is the electron temperature and k is Boltzmann's constant.

For a particle to reach position z, but not the loss position z_L, it is necessary that

$$\frac{\Delta B}{B_o} v_{\perp o}^2 + \frac{2q\phi}{m} < v_{\parallel o}^2 < \frac{\Delta B_L}{B_o} v_{\perp o}^2 + \frac{2q\phi_L}{m} \qquad (4.2.6)$$

The confined velocity space has two symmetric regions of positive and negative $v_{\parallel o}$, so that a factor of two must be inserted when the integration is over positive $v_{\parallel o}$ only. For $q\phi_L > 0$, particles

of any $v_\perp$ can be trapped, so the $v_\perp$ limits are 0 and ∞. The expression for n(z) is then given by

$$n(z) = 4\pi n_* \left(\frac{m}{2\pi kT}\right)^{3/2} \int_0^\infty dv_\perp\, v_{\perp o} \exp\left(-\frac{mv_{\perp o}^2}{2kT}\right) \times$$

$$\int_{\sqrt{\left[\frac{\Delta B_L}{B_o} v_{\perp o}^2 + \frac{2q\phi_L}{m}\right]}}^{\infty} dv_{\perp o} \exp\left(-\frac{mv_{\perp o}^2}{2kT}\right) \left(v_{\perp o}^2 - \frac{\Delta B}{B_o} v_{\perp o}^2 - \frac{2q\phi}{m}\right)^{-1/2} \qquad (4.2.7)$$

Subsequent equations can be simplified by using the following dimensionless variables:

$$x = \frac{mv_{\perp o}^2}{2kT} \qquad y = \frac{mv_{\perp o}^2}{2kT} \qquad \eta = \frac{q\phi}{kT} \qquad \eta_L = \frac{q\phi_L}{kT} \qquad (4.2.8)$$

With these variables (4.2.7) can be rewritten as

$$n(z) = \frac{n_*}{\sqrt{\pi}} \int_0^\infty dy\, e^{-y} \int_{\frac{\Delta B}{B_o} y + \eta}^{\frac{\Delta B_L}{B_o} y + \eta_L} dx\, e^{-x} \left(x - \frac{\Delta B}{B_o} y - \eta\right)^{-1/2} \qquad (4.2.9)$$

The integrals given in appendix A can be used to solve (4.2.9). After normalization to the actual midplane density n_o, one has:

$$n(z) = n_o\, e^{-\eta}\, \frac{F_1(z)}{F_1(0)} \qquad (4.2.10)$$

where $F_1(z) = \operatorname{erf}[\eta_L - \eta]^{1/2} +$

$$\left(1 - \frac{B}{B_L}\right)^{1/2} \exp\left(B\, \frac{\eta_L - \eta}{B_L - B}\right) \left\{1 - \operatorname{erf}\left[B_L\, \frac{\eta_L - \eta}{B_L - B}\right]^{1/2}\right\} \qquad (4.2.11)$$

Yushmanov[3] obtained an equivalent expression for (4.2.11). Aside from a typographical error,[5] BenDaniel[2] did as well. The result of Post[1] is at variance with these results. However, a careful rederivation along the lines given by Post[1] indicates that (4.2.11) is correct.[5]

4.3 Cut-out Maxwellian equation for a potential hill.

The preceding calculations were for particles confined within the mirror by the magnetic field, aided by the electric field. If the plasma potential forms a potential hill rather than a potential well, (i. e., $q\phi_L < q\phi < 0$), a different expression must be used. Figure 4.2 shows the velocity space diagram for this case. In this case the minimum $v_\perp$ for confinement is

$$v_{\perp m} = \left(-\frac{2q\phi_L}{m}\, \frac{B_o}{\Delta B_L}\right)^{1/2} \qquad (4.3.1)$$

The appropriate cut-out Maxwellian integral is

$$n(z) = 4\pi n_* \left(\frac{m}{2\pi kT}\right)^{3/2} \frac{B}{B_o} \int_{v_{\perp m}}^{\infty} dv_{\perp o}\, v_{\perp o} \exp\left(-\frac{mv_{\perp o}^2}{2kT}\right) \times$$

$$\int_{\sqrt{\left(\frac{\Delta B_L}{B_o} v_{\perp o}^2 + \frac{2q\Delta\Phi_L}{m}\right)}}^{\infty} dv_{\parallel o}\, v_{\parallel o} \exp\left(-\frac{mv_{\parallel o}^2}{2kT}\right) \left(v_{\parallel o}^2 - \frac{\Delta B}{B_o} v_{\perp o}^2 - \frac{2q\Delta\Phi}{m}\right)^{-1/2} \Bigg\} \qquad (4.3.2)$$

$$\sqrt{\left(\frac{\Delta B}{B_o} v_{\perp o}^2 + \frac{2q\Delta\Phi}{m}\right)}$$

Using the variables x, y and η defined by (4.2.8) one has

$$n(z) = \frac{n_*}{\sqrt{\pi}} \frac{B}{B_o} \int_{y_m}^{\infty} dy\, e^{-y} \int_{x_1}^{x_2} \frac{dx\, e^{-x}}{\left(x - \left(\frac{\Delta B}{B_o} y + \eta\right)\right)^{1/2}} \qquad (4.3.3)$$

where $y_m = -\frac{B_o \eta_L}{\Delta B_L}$, $x_1 = \frac{\Delta B}{B_o} y + \eta$, $x_2 = \frac{\Delta B_L}{B_o} y + \eta_L$

The inner integral is of the form

$$\int_{x_1}^{x_2} \frac{dx\, e^{-x}}{\left[x - \left(\frac{\Delta B}{B_o}\eta + \eta\right)\right]^{1/2}} = \qquad (4.3.4)$$

$$\sqrt{\pi} \exp\left(-\frac{\Delta B}{B_o}\eta - \eta\right) \operatorname{erf}\left(\left[\left(\frac{\Delta B_L - \Delta B}{B_o}\right) y + \eta_L - \eta\right]^{1/2}\right)$$

Then (4.3.2) becomes

$$n(z) = n_* \frac{B}{B_o} e^{-\eta} \int_{y_m}^{\infty} dy \exp\left(-\frac{B}{B_o} y\right) \operatorname{erf}\left(\left[\frac{B_L - B}{B_o} y + \eta_L - \eta\right]^{1/2}\right) \qquad (4.3.5)$$

Application of integral (12) of appendix A to (4.3.5) gives

$$n(z) = \frac{B_o}{B} \left\{\exp\left(\frac{B\eta_L}{\Delta B_L}\right) \operatorname{erf}\left(\left[\frac{B - B_o}{B_L - B_o} \eta_L - \eta\right]^{1/2}\right) + \right. \qquad (4.3.6)$$

$$\left. \left(1 - \frac{B}{B_L}\right)^{1/2} \exp\left[B \frac{\eta_L - \eta}{B_L - B}\right] \left(1 - \operatorname{erf}\left(\left[\frac{B_L}{B_L - B}\left(\frac{B - B_o}{B_L - B_o} \eta_L - \eta\right)\right]^{1/2}\right)\right)\right\}$$

Then for the case of the potential hill one has

$$n(z) = n_o e^{-\eta} \frac{F_2(z)}{F_2(0)} \qquad (4.3.7)$$

Where $F_2(z) = \exp\left(\frac{B\eta_L}{B_L - B_o}\right) \operatorname{erf}\left[\frac{B - B_o}{B_L - B_o} \eta_L - \eta\right]^{1/2}$

$$+ \left(1 - \frac{B}{B_L}\right)^{1/2} \exp\left(B \frac{\eta_L - \eta}{B_L - B}\right) \left\{1 - \operatorname{erf}\left(\left[\frac{B_L}{B_L - B}\left(\frac{B - B_o}{B_L - B_o} \eta_L - \eta\right)\right]^{1/2}\right)\right\} \qquad (4.3.8)$$

$$= \exp\left(\frac{B\eta_L}{\Delta B_L}\right) \operatorname{erf}\left[\frac{\Delta B}{\Delta B_L} \eta_L - \eta\right]^{1/2}$$

$$+ \left(1 - \frac{B}{B_L}\right)^{1/2} \exp\left(B \frac{\eta_L - \eta}{B_L - B}\right) \left\{1 - \operatorname{erf}\left(\left[\frac{B_L}{B_L - B}\left(\frac{\Delta B}{\Delta B_L} \eta_L - \eta\right)\right]^{1/2}\right)\right\}$$

It should be noted that (4.3.7) and (4.3.8) account only for the density of particles that cross the midplane. There may be non-midplane-crossing particles present.

4.4 Influence of "wall confined" particles on density.

In the DC Machine and most other mirror devices, the end wall is located not at maximum B ("L"), but some distance further out ("W"), where the magnetic field has fallen to B_W. For the case of the potential hill this does not change the confined region of midplane velocity space. In the potential well, however, the potential continues to rise from $q\phi_L$ to $q\phi_W$. The particles which cross L with low $v_\parallel$, previously considered lost, will be electrostatically reflected. These "wall confined" particles form a new region of confinement in midplane velocity space, as is shown in figure 4.3.

To extend the cut-out Maxwellian approach to this case, one integrates over those positions in velocity space which are in the trapped region for either z_L or z_W. For wall confined particles to reach a point with magnetic field B and normalized potential η, the requirement is

$$(\frac{B}{B_o} - 1)y + \eta \leq x \leq (\frac{B_W}{B_o} - 1)y + \eta_W \qquad (4.4.1)$$

For mirror confined particles the requirement is

$$(\frac{B}{B_o} - 1)y + \eta \leq x \leq (\frac{B_L}{B_o} - 1)y + \eta_L \qquad (4.4.2)$$

Note that for y below a certain y_m, equation (4.4.1) sets the limits on x for confinement; for $y > y_m$, (4.4.2) applies. The value of y_m is

$$y_m = \frac{mv_{\perp m}^2}{2kT} = B_o \frac{\eta_W - \eta_L}{B_L - B_W} \qquad (4.4.3)$$

The cut-out Maxwellian integral is adjusted to cover the boundaries of midplane velocity space for the two regions:

$$n = \frac{n_*}{\sqrt{\pi}} \frac{B}{B_o} \int_{y_m}^{\infty} dy\, e^{-y} \int_{(\frac{B}{B_o}-1)y+\eta}^{(\frac{B_L}{B_o}-1)y+\eta_L} dx \frac{e^{-x}}{(x - (\frac{B}{B_o}-1)y - \eta)^{1/2}} \qquad (4.4.4)$$

$$+ \frac{n_*}{\sqrt{\pi}} \frac{B}{B_o} \int_{y_m}^{\infty} dy\, e^{-y} \int_{(\frac{B}{B_o}-1)y+\eta}^{(\frac{B_W}{B_o}-1)y+\eta_W} dx \frac{e^{-x}}{(x - (\frac{B}{B_o}-1)y - \eta)^{1/2}}$$

The inner integrals have the form

$$\int dw\, e^{-w} (w + b)^{-1/2} = \sqrt{\pi}\, e^{b}\, \mathrm{erf}([w + b]^{1/2})$$

The first inner integral of 4.4.4 becomes

$$\int_{(\frac{B}{B_o}-1)y+\eta}^{(\frac{B_L}{B_o}-1)y+\eta_L} dx\, e^{-x}\,(x-(\tfrac{B}{B_o}-1)y-\eta)^{-1/2} \qquad (4.4.5)$$

$$= \sqrt{\pi}\,\exp[-(\tfrac{B}{B_o}-1)y-\eta]\,\operatorname{erf}\Big(\big[(\tfrac{B_L-B}{B_o})y+\eta_L-\eta\big]^{1/2}\Big)$$

The second inner integral of (4.4.4) is

$$\int_{(\frac{B}{B_o}-1)y+\eta}^{(\frac{B_W}{B_o}-1)y+\eta_W} dx\, e^{-x}\,(x-(\tfrac{B}{B_o}-1)y-\eta)^{-1/2} \qquad (4.4.6)$$

$$= \sqrt{\pi}\,\exp[-(\tfrac{B}{B_o}-1)y-\eta]\,\operatorname{erf}\Big(\big[(\tfrac{B_W-B}{B_o})y+\eta_W-\eta\big]^{1/2}\Big)$$

The first integral of (4.4.4) is now

$$n_1 = n_* e^{-\eta}\,\frac{B}{B_o}\int_{y_m}^{\infty} dy\,\exp(-\tfrac{B}{B_o}y)\,\operatorname{erf}\big([\tfrac{B_L-B}{B_o}]y+\eta_W-\eta\big]^{1/2}) \qquad (4.4.7)$$

From Appendix A, integral 12, this is

$$n_1 = n_* e^{-\eta}\,\frac{B}{B_o}\Big\{-\frac{B_o}{B}\exp(-\tfrac{B}{B_o}y)\,\operatorname{erf}\big([(\tfrac{B_L-B}{B_o})y+\eta_L-\eta]^{1/2}\big)$$

$$+\frac{B_o}{B}(1-\tfrac{B}{B_L})^{1/2}\exp\Big(B\tfrac{\eta_L-\eta}{B_L-B}\Big)\operatorname{erf}\Big(\big[\tfrac{B_L}{B_L-B}\big[(\tfrac{B_L-B}{B_o})y+\eta_L-\eta\big]\Big]\Big|_{y_m}^{\infty} \qquad (4.4.8)$$

$$= n_* e^{-\eta}\Big\{\exp(-\tfrac{B}{B_o}y_m)\,\operatorname{erf}\big([(\tfrac{B_L-B}{B_o})y_m+\eta_L-\eta]^{1/2}\big)$$

$$+(1-\tfrac{B}{B_L})^{1/2}\exp\Big(B\tfrac{\eta_L-\eta}{B_L-B}\Big)\Big(1-\operatorname{erf}\big([\tfrac{B_L}{B_o}y_m+B_L\tfrac{\eta_L-\eta}{B_L-B}]^{1/2}\big)\Big)\Big\}$$

$$= n_* e^{-\eta}\Big\{\exp(-B\tfrac{\eta_W-\eta_L}{B_L-B_W})\,\operatorname{erf}\Big(\big[\tfrac{B_L-B}{B_L-B_W}(\eta_W-\eta_L)+\eta_L-\eta\big]^{1/2}$$

$$+(1-\tfrac{B}{B_L})^{1/2}\exp\Big(B\tfrac{\eta_L-\eta}{B_L-B}\Big)\Big(1-\operatorname{erf}\big([B_L(\tfrac{\eta_W-\eta_L}{B_L-B_W}+\tfrac{\eta_L-\eta}{B_L-B})]^{1/2}\big)\Big)\Big\}$$

The second integral of (4.4.4) is:

$$n_2 = n_* e^{-\eta}\,\frac{B}{B_o}\int_0^{y_m} dy\,\exp(-\tfrac{B}{B_o}y)\,\operatorname{erf}\big([(\tfrac{B_W-B}{B_o})y+\eta_W-\eta\big]^{1/2}) \qquad (4.4.9)$$

For $B > B_W > 0$ one obtains

$$n_2 = n_* e^{-\eta}\,\frac{B}{B_o}\Big\{-\frac{B_o}{B}\exp(-\tfrac{B}{B_o}y)\,\operatorname{erf}\big([(\tfrac{B_W-B}{B_o})y+\eta_W-\eta]^{1/2}\big)$$

$$+\frac{B_o}{B}[1-B_W/B]^{1/2}\exp\Big(B\tfrac{\eta_W-\eta}{B_W-B}\Big)\operatorname{erf}\Big(\big[\tfrac{B}{B-B_W}\big\{\tfrac{B_W-B}{B_o}y+\eta_W-\eta\big\}\big]^{1/2}\Big)\Big|_0^{y_m}$$

$$= n_* e^{-\eta}\Big\{\operatorname{erf}[\eta_W-\eta]^{1/2}-\exp(-\tfrac{B}{B_o}y_m)\operatorname{erf}\big([\tfrac{B_W-B}{B_o}y_m+\eta_W-\eta]^{1/2}\big)$$

$$+(1-\tfrac{B_W}{B})^{1/2}\exp\Big(B\tfrac{\eta_W-\eta}{B_W-B}\Big)\Big(\operatorname{erf}\big([-\tfrac{B}{B_o}y_m+B\tfrac{\eta_W-\eta}{B-B_W}]^{1/2}\big)-\operatorname{erf}\big([\tfrac{\eta_W-\eta}{B-B_W}]^{1/2}\big)\Big)\Big\} \qquad (4.4.10)$$

$$= n_* e^{-\eta} \{\mathrm{erf}[\eta_W-\eta]^{1/2} \exp(-B \frac{\eta_W-\eta_L}{B_L-B_W}) \mathrm{erf}([\frac{B_W-B}{B_L-B_W}(\eta_W-\eta_L) + \eta_W-\eta]^{1/2})$$

$$+(1- \frac{B_W}{B})^{1/2} \exp(B\frac{\eta_W-\eta}{B_W-B})(\mathrm{erf}([B(\frac{\eta_W-\eta}{B-B_W} - \frac{\eta_W-\eta_L}{B_L-B_W})]^{1/2})-\mathrm{erf}([B\frac{\eta_W-\eta}{B-B_W}]^{1/2}))\}$$

When $B_W < B < B_L$ and $\eta < \eta_L < \eta_W$) the plasma density is

$$n = n_1 + n_2 \qquad (4.4.11)$$

$$= n_* e^{-\eta} \{\exp(-B\frac{\eta_W-\eta_L}{B_L-B_W}) \mathrm{erf}([\frac{B_L-B}{B_L-B_W}(\eta_W-\eta_L) + \eta_L-\eta]^{1/2})$$

$$+ (1- \frac{B}{B_L})^{1/2}\exp(B\frac{\eta_L-\eta}{B_L-B}) (1 - \mathrm{erf}([B_L(\frac{\eta_W-\eta_L}{B_L-B_W} + \frac{\eta_L-\eta}{B_L-B}]^{1/2}))$$

$$+ \mathrm{erf}([\eta_W-\eta]^{1/2} - \exp(-B\frac{\eta_W-\eta_L}{B_L-B_W} \mathrm{erf}([\frac{B_W- B}{B_L-B_W}(\eta_W-\eta_L) + \eta_W-\eta]^{1/2})$$

$$+ (1- \frac{B_W}{B})^{1/2} \exp(B\frac{\eta_W-\eta}{B_W-B}) [\mathrm{erf}([B(\frac{\eta_W-\eta}{B-B_W} - \frac{\eta_W-\eta_L}{B_L-B_W})-\mathrm{erf}([B\frac{\eta_W-\eta}{B-B_W}]\}$$

4.5 Extension of the Cut-out Maxwellian approach for a more detailed potential profile

In a real plasma the electrostatic potential will vary along the magnetic field lines. It is entirely possible that particles at a given point in midplane velocity space will satisfy the loss criteria for both the maximimum B field position and the wall position, but not for some other position. In this case they remain confined. To obtain a good approximation to the true loss region it is necessary to look at the entire region $0 < z < W$ in enough detail so that the intermediate barriers to loss are found.

To do this, let the midplane-to-wall distance be divided into K cells, in the k-th of which the magnetic field and plasma potential are B_k and ϕ_k respectively. For cell n, the loss criterion associated with cell k, ($k > n$) is

$$v_\parallel^2 > (\frac{B_k}{B_n} -1)v_\perp^2 + \frac{2q}{m}(\phi_k-\phi_n) \qquad (4.5.1)$$

Or in terms of the normalized variables of (4.2.8), $x > y(\frac{B_k}{B_n} -1) + \eta_k - \eta_n$.

Figure 4.5 shows the confinement regions for three exterior cells, but the same principles apply to any number of cells. In (x,y) symbolism the boundaries of the confinement regions are straight lines, with an x-intercept of $\eta_k-\eta_\ell$ and a slope equal to $\frac{B_k}{B_\ell} -1$, where k is the subscript of the exterior cell and ℓ is that of the point where the density is to be calculated. In the case of $B_{k'} > B_k$ the value of y at which exterior cell k' begins to determine the loss-trapped boundary in place of cell k is given by

$$y = B_n \frac{\eta_k - \eta_{k'}}{B_{k'} -B_k} \qquad (4.5.2)$$

Let M be the number of exterior cells that make up the loss boundary for cell ℓ. It is convenient to re-label these cells as $m = 1, 2, \ldots M$, in which bin m determines the loss curve for $y_m < y < y_{m+1}$. Also let the doubly subscipted variable $y_{m\ell}$ be given by

$$y_{m\ell} = B_\ell \frac{n_m - n_\ell}{B_m - B_\ell} \qquad (4.5.3)$$

Then the cut-out density in cell ℓ is given by

$$n_\ell = n_* \exp(-n_\ell) \times \qquad (4.5.4)$$

$$\sum_{m=1}^{M} \{\exp(-y_m)\ \mathrm{erf}[(\frac{B_m}{B_\ell} -1)(y_m+y_{m\ell})]^{1/2} -$$

$$\exp(-y_{m+1})\ \mathrm{erf}[(\frac{B_{m+1}}{B_\ell} -1)(y_{m+1}+y_{m\ell})]^{1/2}$$

$$+ (1- \frac{B_\ell}{B_m})^{1/2} \exp(y_{m\ell})\ \mathrm{erf}[\frac{B_m}{B_\ell}(y_{m+1}+y_{m\ell})]^{1/2} - \mathrm{erf}[\frac{B_m}{B_\ell}(y_{m+1}+y_{m\ell})]^{1/2}\}$$

4.6 Hybrid simplex approximation

The "wall confined" expression of section 4.4 has four limiting parameters (B_L, ϕ_L, B_W, and ϕ_W), and is rather complicated. It is possible to obtain a more tractable form by adopting two idealizations:

1. The magnetic field at the wall is equal to that at midplane.
2. The potential is constant throughout the plasma, but changes abruptly at the wall (square well approximation).

The trapped region is then like that of figure 4.4. In this "hybrid simplex approximation", the borders of the confined region of velocity space are straight lines.

The density at z is

$$n(z) = n_* \{\mathrm{erf}[n_W]^{\frac{1}{2}} + (1- \frac{B}{B_L})^{1/2} (1 - \mathrm{erf}[\frac{B_L}{B_L-B_o} n_W]^{1/2} + \qquad (4.6.1)$$

$$(\frac{B}{B_o} -1)^{\frac{1}{2}} \exp[- \frac{B\ n_W}{B-B_o}] (H[\frac{B_o}{B_L-B_o} \frac{B_L-B}{B-B_o} n_W]^{\frac{1}{2}} - H[\frac{B_o}{B-B_o} n_W]^{\frac{1}{2}}) \}$$

The hybrid simplex loss region is used in chapter 7 for density calculation of non-Maxwellian distributions.

4.7 Cut-out Maxwellian for end zone plasmas

Between the position of maximum B and the wall (the end zone) the magnetic field tends to push the particles out. Only when $q\phi$ is increasing toward the wall is particle confinement possible. In this case the density of [electrostatically] trapped particles is given by

$$n = n_*\{\mathrm{erf}[n_W-n]^{1/2} - (\frac{B-B_W}{B})^{1/2} \exp[B \frac{n_W-n}{B_W-B}] H[B_W \frac{n_W-n}{B-B_W}]^{1/2} \qquad (4.7.1)$$

H(x) is the error function analogue, given in appendix A. When the drop to the wall n_W-n approaches zero, this reduces to $n \sim \frac{2}{\pi} n_*(n_W-n) (1- \frac{B_W}{B})^{1/2}$. If particles are electrostatically trapped by the walls and magnetically trapped by the magnetic mirror maximum they can remain in the end zone. They are then said to be "Yushmanov trapped".

To recapitulate this chapter, a series of forms for "cut-out Maxwellian" density have been derived. The governing magnetic and electrostatic potential will determine which is to be used. These forms will be useful whenever it is desirable to analyze the effects of having only part of velocity space populated. In particular, these models are used in chapters 5 and 7 to find a self-consistent density and potential profile.

Figure 4.1 Midplane phase space for $q\Phi_L > 0$.
A particle at the midplane is in a potential well

Figure 4.2 Midplane phase space for $q\Phi_L < 0$.
A particle at the midplane is located on a potential hill. Unless it has sufficient $v_\perp$ for magnetic confinement, it is lost.

Figure 4.3 Effect of wall potential on confinement.
Here there is an increase in the effective potential from midplane to mirror, and an additional increase to the wall.
Top diagram: wall magnetic field B_w exceeds midplane field B_o. The outer edge of the new loss boundary is concave outward.
Center diagram: $B_w = B_o$. The new loss boundary is vertical.
Lower diagram. $B_w < B_o$. The loss boundary is convex outward.

Figure 4.4 Midplane phase space for $q\Phi_L > 0$ (hybrid simplex approximation)
The boundaries of the hyberboloid loss boundary of Fig. 4.1 are "straightened out" in this approxmation, which is appropriate to a situation in which particles must pass a pure mirror and a pure electrostatic barrier independently.

Figure 4.5 Trapped regions of velocity space for a discrete sequence of exterior cells.

Figure 4.1 Midplane phase space for $q\Phi_L > 0$

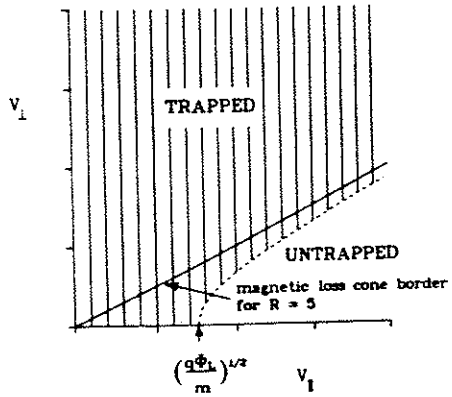

Figure 4.2 Midplane phase space for $q\Phi_L < 0$

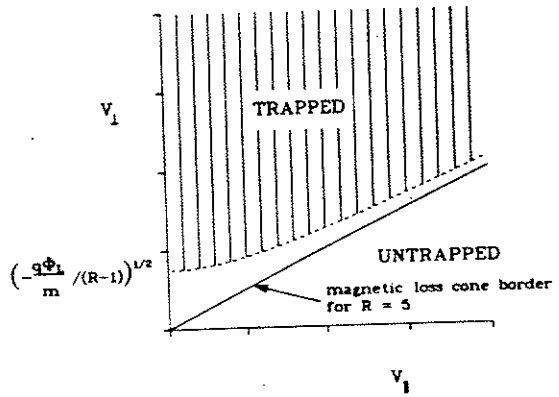

Figure 4.3
Effect of wall potential on confinement

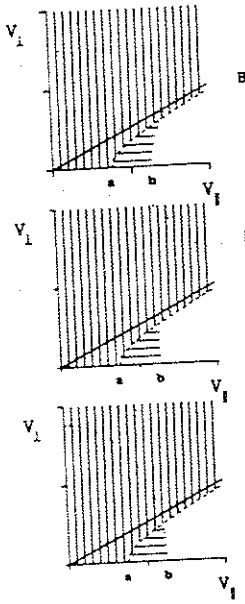

NOTES

1. Magnetic loss cone border for R = 5 is shown by solid line.
2. Dashed line shows trapping border associated with mirror at L.
3. Dotted line shows trapping border associated with wall at W.
4. Mirror trapped region is vertically shaded. Parallel speed at a = $(q\Phi_L/m)^{1/2}$
5. Wall trapped region is horizontally shaded. Parallel speed at b = $(q\Phi_w/m)^{1/2}$

Figure 4.4 Midplane phase space for $q\Phi_L > 0$ (hybrid simplex approximation)

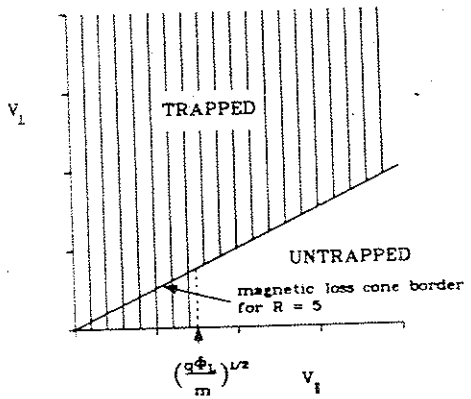

Figure 4.5
Trapped regions of velocity space for a discrete sequence of exterior cells.

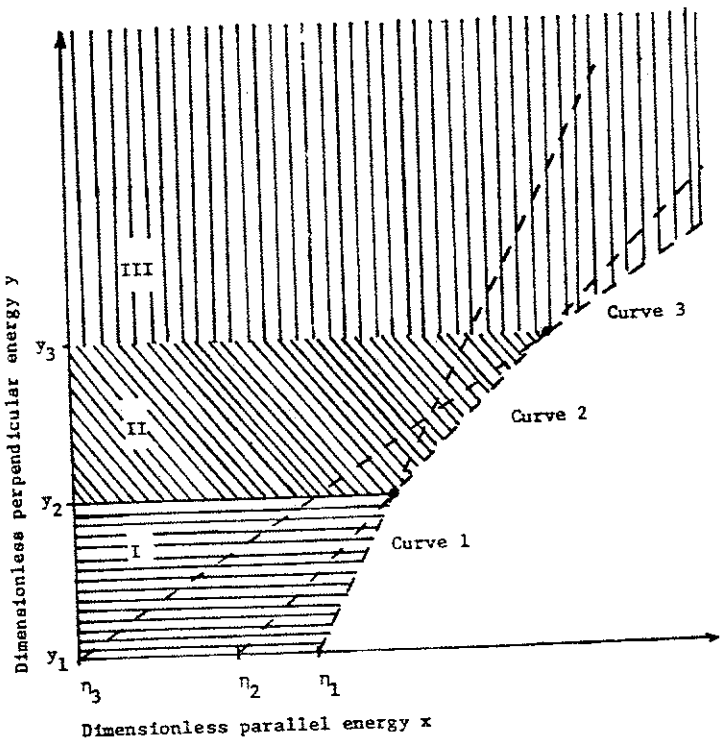

REFERENCES FOR CHAPTER 4

[1] R. F. Post, Phys. Fluids 4, 902 (1961).

[2] D. J. BenDaniel, Plasma Physics 3, 235 (1961).

[3] E. E. Yushmanov, Sov. Phys. JETP 22, 409 (1966).

[4] R. H. Cohen, UCRL-84535 (Lawrence Livermore Laboratory, 1980).

[5] P. K. Smith, PLP 885, (Dec., 1982).

Chapter 5. Theory and experiment for the potential change across the mirror length

In this chapter models are presented which predict the potential in a mirror without explicitly considering ECRH. Such models have prospective application in explaining the behavior of ion extraction sources and "cold" plasma blankets surrounding a hot fusion plasma. The cut-out Maxwellian results of Chapter 4 are used in some of the models. But first a model embodying a simple Maxwellian is presented.

5.1 Free fall model series solution with strict neutrality

The "free fall" model has been used for many years to describe planar discharges.[1] Its assumptions are that

(A1) Steady state conditions prevail.

(A2) Ion and electron densities are equal.

(A3) The electron density at axial position z is given by the Boltzmann relation:

$$n_e(z) = n_o \exp[-\eta] \equiv n_o \exp\left(\frac{e\phi(z)}{kT_e}\right) \qquad (5.1.1)$$

In (5.1.1) n_o is the density at the midplane, e is the electronic charge, k is Boltzmann's constant, T_e is the electron temperature, $\phi(z)$ is the electrostatic potential at z, with $\phi(0)$ being chosen as the zero potential.

(A4) T_e is constant along a field line.

(A5) Background neutral gas has constant density n_g. This is a valid assumption since the e-folding time for pumping out molecules, 2.7 seconds at the measured 165 l/sec pumping speed, is much longer that the transit time of the molecules across the machine. The plasma/neutral gas fraction is ~1%, and thus burnout of neutrals by ionization can be neglected.

(A6) Ions are created by electron ionization of neutral gas only.

(A7) Plasma potential falls monotonically from center to walls.

(A8) Ions are created with zero energy and move along the magnetic field lines with an energy acquired in descending through an electrostatic potential. They are lost upon reaching the end wall. This means that both thermal motion and collisions of the ions are ignored. The $\mu\nabla B$ force and radial transport of ions across the magnetic field are also neglected. Assumption (A8) leads to the name "free fall" for this model.

Some previous workers on the DC Machine have assumed unheated ions,[2,3] which suggests the use of the free fall model for the determination of plasma potential and density along a field line. Previous solutions of the problem[1,4,5,6,7] were based on the assumption of a constant (or non-existent) magnetic field. When the magnetic field is allowed to vary, the transform methods of solving the free fall model--Abel's transform, Schlömilch's transform,[8] and Laplace's transform--fail. It is still possible

to use the neutrality condition (A2) to obtain a power series of the form

$$s = \eta^{1/2} (a_0 + a_1\eta + a_2\eta^2 + \cdots + a_m\eta^m + \cdots) \qquad (5.1.2)$$

Here $s = z/L$, the distance from the midplane in units of the ionization scale length: $L = (\frac{2kT_e}{M_i})^{1/2} / (n_g \langle\sigma v\rangle_{ion})$

If the magnetic field can be adequately represented by

$$\frac{1}{B} = \frac{1}{B_o} (1 + b_1 s^2 + b_2 s^4) \qquad (5.1.3a)$$

then one has the ratio

$$\frac{B_o}{B(\eta)} = \sum_{m=0}^{\infty} \beta_m \eta^m \qquad (5.1.3b)$$

and the definition $\gamma_m = \sum_{j=0}^{m} \frac{(-1)^j}{j!} \beta_{m-j}$ (5.1.3c)

The coefficients of the series expansion in (5.1.2) are

$$a_m = \frac{1}{2m+1} (\gamma_m [\frac{2}{\pi} \frac{2m!!}{(2m-1)!!} - a_0] - \sum_{j=1}^{m-1} (2j+1) a_j \gamma_{m-j}) \qquad (5.1.4)$$

In terms of a_m, $\gamma_m = \frac{\pi}{2} \frac{(2m-1)!!}{2m!!} \sum_{j=0}^{m} (2j+1) a_j \gamma_{m-j}$ (5.1.5)

and $\gamma_0 = 1$, $a_0 = \frac{2}{\pi}$. In terms of b_1 and b_2 the first a_m values are

$$a_0 = 2/\pi \qquad (5.1.6a)$$

$$a_1 = 8b_1/3\pi^3 - 2/3\pi \qquad (5.1.6b)$$

$$a_2 = 32b_1^2/45\pi^5 - 56b_1/45\pi^3 + 32b_2/3\pi^5 - 1/15\pi \qquad (5.1.6c)$$

$$a_3 = -1792b_1^3/225\pi^7 + 4192b_1^2/1575\pi^5 \qquad (5.1.6d)$$
$$+ 68b_1/525\pi^3 + (3328b_1b_2)/105\pi^7 - 1184b_2/105\pi^5 - 1/105\pi$$

A computer program was written to use (5.1.4) to find a_m up to any number of terms. A listing is given in PLP 886.[9] Figures 5.1, 5.2, and 5.3 show, for mirror ratios of 1.1, 2, and 3, respectively, a comparison of the free-fall model predictions with and without the affects of magnetic field.

In general n increases more rapidly in a region of increasing B than in a constant B field. The problem of infinite electric fields sometimes occurs, as in figure 5.3. This results from the neglect of the $\frac{d^2\phi}{dz^2}$ term in Poisson's equation. This is corrected in section 5.2.

5.2 Free fall model numerical solution of the complete plasma equation

Tonks and Langmuir[1] were the first to investigate the "plasma equation", in which a Boltzmann type electron density term, and an ion density term derived from a specified source function in space, are substituted into Poisson's equation.

The equation to be solved is

$$\left(\frac{\lambda_D}{L}\right)^2 \frac{d}{ds}\left(\frac{1}{B}\frac{d\eta}{ds}\right) + \frac{\exp(-\eta)}{B} = \int_0^s \frac{\exp(-\eta')}{B'} \frac{ds'}{[\eta - \eta']^{1/2}} \qquad (5.2.1)$$

Here $\lambda_D = \left(\frac{\epsilon_o kT_e}{ne^2}\right)^{1/2}$, the midplane electron Debye length.

To solve (5.2.1) numerically, the distance between the midplane and wall is divided into a large number [100] of smaller intervals. In each interval $\frac{1}{B}$ and η are approximated by quadratics.

Detailed discussion of the numerical solution is given by Smith.[9] Suffice it to say a program was written that makes it possible to incorporate the effects of an almost arbitrary magnetic field into a solution of Poisson's equation in the free fall model. Figure 5.4 shows the present model compared the the results of Self,[5] for the zero B case, as well as for the model neglecting the second deriviative term, the "plasma approximation" of section 5.1. The present model and the Self[5] model agree in this case.

Figure 5.5 shows the η vs. s profiles for a magnetic field with increases away from midplane as given by

$$B = B_o\left(1 + \frac{z^2}{L_M^2}\right) \qquad (5.2.2)$$

In Figure 5.6 the η vs. s profile is shown for a magnetic field with decreases away from midplane as given by

$$B = B_o/\left(1 + \frac{z^2}{L_M^2}\right) \qquad (5.2.3)$$

As in section 5.1, the general rule is that η increases more rapidly than in the constant B case if B increases outward, and increases less rapidly than in the constant B case if B is decreasing from the midplane.

Figure 5.7 shows the η profiles expected with a magnetic field like the simple mirror configuration of the DC Machine, for three values of tank pressure. η at the mirror is considerably increased over that calculated assuming constant B. By using the ionization flux Γ_{ion} to the wall from this model the total normalized potential change between midplane and wall is found from the condition that the outgoing electron flux be attenuated to the ion level:

$$\eta_w = \ln\left(\frac{n_o\left(\frac{kT_e}{2\pi m_e}\right)^{1/2}}{\Gamma_{ion}}\right) \qquad (5.2.4)$$

The results are shown in figure 5.8 for helium, along with experimental data points for this magnetic field. The data points do not agree with the free fall model with magnetic field effects included, any better than with such effects neglected. Three reasons are possible for this state of affairs:

(1) The ion population is not really a free-fall distribution. This is borne out by gridded analyzer traces, indicating a substantial Maxwellian ion component.

(2) The electron distribution loss region has been neglected.

(3) Within the trapped region of electron velocity space, the distribution may deviate from a Maxwellian because of RF heating.

Problems (1) and (2) are partially addressed in the remaining sections. Inclusion of RF heating effects is generally more difficult. This is discussed in chapter 7.

5.3 Kaufman model

One of the earliest estimates of plasma potential in a mirror was that of Kaufman,[10] for a square well magnetic system, assuming a balance of Coulomb scattering rates of ions and electrons. The drop of potential to the wall in units of electron temperatures, denoted as γ is

$$\gamma = \ln\left[\left(\frac{T_i}{T_e}\right)^{3/2}\left(\frac{m_i}{m_e}\right)^{1/2}\right] = \ln\left(\frac{\nu_{ee}}{\nu_{ii}}\right) \qquad (5.3.1a)$$

The effects of neutral scattering can be incorporated into the Kaufman model by using the total collision rates for electrons (ν_e) and ions (ν_i), rather than the self-collision rates:

$$\gamma = \ln\left(\frac{\nu_e}{\nu_i}\right) \qquad (5.3.1b)$$

Figure 5.9 shows the observed values of η vs. the theoretical predictions of the Kaufman model (5.3.1a) and (5.3.1b). Perfect agreement would be a straight line at 45°. Inclusion of neutrals improves the agreement of theory and experiment; the points are moved to the proper quadrant. The data were taken with H_2, He, and Ar plasmas over a wide range of parameters.

5.4 BenDaniel-Brambilla-Werkoff Model

This model was first proposed by BenDaniel[11] and elaborated upon by Brambilla and Werkoff.[12] Loss rate coefficients K_i and K_e govern particle loss balance in steady state:

$$\frac{1}{n_e}\frac{dn_e}{dt} = -K_e[\bar{n}_e + \bar{n}_i] = \frac{1}{n_i}\frac{dn_i}{dt} = -K_i\,\bar{n}_i \qquad (5.4.1)$$

where $\bar{n}_e$ and $\bar{n}_i$ are average densities for electrons and ions, respectively, approximated by the central density values. The results of simplified Fokker-Planck formalism are used to define

$$K_i = \left(\frac{1}{T_i}\right)^{3/2}\frac{N(N+1)}{2}\frac{1}{(m_i)^{1/2}}\,C_1 \qquad (5.4.2)$$

$$\text{and}\quad K_e = \left(\frac{1}{T_e}\right)^{3/2}\frac{\exp[-\gamma}{(m_e)^{1/2}}\frac{1}{\gamma^{3/2}}\,C_1 \qquad (5.4.3)$$

C_1 is a constant, and N is an eigenvalue dependent on mirror ratio

R obtained from Fokker-Planck theory.[13] Substitution of (5.4.3) and (5.4.2) into (5.4.1) gives the equation for γ:

$$\gamma + \frac{3}{2}\ln\gamma - \ln\left[2\ \ln\left(\frac{R}{1+\frac{T_e}{T_i}\gamma}\right)\right] = \ln\left[\left(\frac{T_i}{T_e}\right)^{3/2}\left(\frac{m_i}{m_e}\right)^{1/2}\right] = \nu\left(\frac{\nu_{ee}}{\nu_{ii}}\right) \tag{5.4.4}$$

As in the Kaufman model, inclusion of neutrals is possible with replacement of the RHS of (5.4.4) with the total collision rates: $\nu_{ee} \to \nu_e$, $\nu_{ii} \to \nu_i$.

BenDaniel[11] originally used the effective mirror ratio as

$$R_{eff} = \frac{R}{1+\frac{T_e}{T_e}\gamma} \tag{5.4.5}$$

This gives the proper loss cone angle in velocity space for a monergic distribution. This can be generalized to a cut-out Maxwellian by setting using as R_{eff} the value obtained from

$$\left(1-\frac{1}{R_{eff}}\right)^{1/2} = f_t \text{ (trapped fraction of v-space)} \tag{5.4.6}$$

In figure 5.10 observed values of γ are plotted against theoretical predictions of γ from the BenDaniel-Bramilla-Werkoff model with corrections for neutrals and non-monoegic distributions. For the DC Machine $\eta \sim 4$-5 is predicted with this model with normal operating parameters. The experimental spread is much larger.

5.5 Sprott Model

Sprott[14] equated loss rates in a square well model of a mirror based on the relative size of scattering rates. The potential drop is assumed to take place at the walls of the device, so that the loss fraction is the same for both ions and electrons and is $1 - \sqrt{1 - 1/R}$. The rate of scattering into the loss cone is taken to be

$$\nu_{scatt,e} = \nu_e / \log_{10} R \qquad \nu_{scatt,i} = \nu_i / \log_{10} R \tag{5.5.1}$$

for electrons and ions, respectively, with ν_e and ν_i the 90° scattering rates. The requirement that the ion and electron scattering into the loss region each equal the ionization rate leads to the values

$$e\Phi = -kT_i \ln\left[1 + (1-\frac{1}{R})^{1/2}\left(\frac{\nu_i}{\nu_e} - 1\right)\right] \tag{5.5.2}$$

$(\nu_i > \nu_e)$

$$e\Phi = kT_e \ln\left[1 + (1-\frac{1}{R})^{1/2}\left(\frac{\nu_e}{\nu_i} - 1\right)\right] \tag{5.5.3}$$

$(\nu_i < \nu_e)$

In the original model scattering by neutrals into the loss cone was given the same $(\log_{10}R)^{-1}$ dependence that characterizes Coulomb scattering. Neutral scattering may be somewhat better represented with a hard-sphere approximation, which leaves the colliding particle randomly distributied in pitch angle. This can be incorporated into the model by the substitutions of

$$\nu_i^* = \nu_{in}(1 - \sqrt{1 - 1/R}) + \nu_{ii}/\log_{10}R \qquad \text{for } \nu_i$$

$$\nu_e^* = \nu_{en}(1 - \sqrt{1 - 1/R}) + (\nu_{ee} + \nu_{ei})/\log_{10}R \qquad \text{for } \nu_e$$

Figure 5.11 shows the observed values of n compared with the predictions of this model, with and without the neutral scattering term modifications suggested above. The results are not greatly affected by the change.

A similar calculation is the estimate of ϕ given by Kesner, Knorr, and Nicholson,[15] who equated a Maxwellian electron density to ion densities given a "pre-acceleration", in a specified region of velocity space. They were interested in finding the conditions under which a potential minimum could occur in a magnetic field minimum.

5.6 Smith model

In this model an estimate of the central plasma potential in a magnetic mirror is found from the rates of particle incrementation ν_i, the loss rate ν_l, and the scattering rate ν_s. The working assumptions of this model are:

(1) The trapped and untrapped regions of velocity space are populated with characteristic densities n_1 and n_2, respectively. Then the actual density of particles in each region is

$$n_T = n_1 f_T \qquad n_u = n_2(1 - f_T) \tag{5.6.1}$$

where f_T is the trapped fraction of velocity space.

(2) Particles are created at rate ν_i and in proportion to the existing distribution function value:

$$\frac{dn_1}{dt}\Big|_i = \nu_i n_1 \qquad \frac{dn_2}{dt}\Big|_i = \nu_i n_2 \tag{5.6.2}$$

In the present experiments ν_i is the ionization rate, $\nu_i = \nu_{ion} = n_g\langle\sigma v\rangle_{ion}$, with n_g the neutral gas density and $\langle\sigma v\rangle_{ion}$ the ionization reaction rate. In other devices it could represent the injection rate of a beam.

(3) Particles in the untrapped region are lost at rate ν_l:

$$\frac{dn_2}{dt}\Big|_l = -\nu_l n_2 \tag{5.6.3}$$

The mean loss frequency can be obtained from the mean loss speed:

$$\nu_l = \frac{\bar{v}_l}{W} \qquad (5.6.4)$$

where W is the midplane-to-wall distance. In (5.6.4) $\bar{v}_l$ is the mean outward speed within the loss region. The expression for $\bar{v}_l$ is

$$\bar{v}_l = \frac{\exp(-\eta_L)}{R}\left(\frac{kT}{2\pi m_i}\right)^{1/2} \qquad (5.6.5a)$$

$(\eta > 0,\ R > 1)$

$$\bar{v}_l = \exp(-\eta_w)\left(1 - (1-\frac{1}{R})^{1/2}\exp\left[\frac{-\eta_w}{R-1}\right]\right)\left(\frac{kT}{2\pi m_i}\right)^{1/2} \qquad (5.6.5b)$$

$(\eta > 0,\ R > 1)$

(hybrid simplex approximation)

$$\bar{v}_l = \left\{\exp\left(-\frac{\eta_L}{1-R}\right) + \frac{\exp(-\eta_L)}{R}\left(1-\exp\left(\frac{R}{R-1}\eta_L\right)\right)\right\}\left(\frac{kT}{2\pi m_i}\right)^{1/2} \qquad (5.6.5c)$$

$(\eta > 0,\ R < 1)$

$$\bar{v}_l = \left(1 - \frac{R-1}{R}\exp\left(\frac{\eta_L}{R-1}\right)\right)\left(\frac{kT_i}{2\pi m_i}\right)^{1/2} \qquad (5.6.5d)$$

$(\eta < 0)$

The loss speed is essentially the same as that given by Knight[16] for currents in auroras.

(4) Particles are scattered in such a way that the distribution tends toward an isotropic Maxwellian at rate ν_s:

$$\frac{dn_T}{dt}\Big|_s = -\nu_s\, n_T\,(1 - f_T) + \nu_s\, n_u\, f_T \text{ , or}$$

$$\frac{dn_l}{dt}\Big|_s = -\nu_s\,(n_1 - n_2)(1 - f_T) \qquad (5.6.6)$$

$$\frac{dn_u}{dt}\Big|_s = \nu_s\, n_T\,(1 - f_T) - \nu_s\, n_u\, f_T \text{ , or}$$

$$\frac{dn_l}{dt}\Big|_s = \nu_s\,(n_1 - n_2)\, f_T \qquad (5.6.7)$$

In steady state one must have

$$\dot{n}_1 = \nu_i\, n_1 - \nu_s\,(n_1 - n_2)\,(1 - f_T) = 0 \qquad (5.6.8)$$

$$\dot{n}_2 = \nu_i\, n_2 - \nu_s\,(n_1 - n_2)\, f_T - \nu_1\, n_2 = 0 \qquad (5.6.9)$$

From the difference of (5.6.8) and (5.6.9) one finds the relative values of n_1 and n_2:

$$n_2 = \frac{\nu_s - \nu_i}{\nu_1 + \nu_s - \nu_i}\, n_1 \qquad (5.6.10)$$

Substituting (5.6.10) into (5.6.9) gives the trapped fraction of velocity space:

$$f_T = \frac{(\nu_1 - \nu_i)(\nu_s - \nu_i)}{\nu_s\,\nu_1} \qquad (5.6.11)$$

For rapid particle loss, $\nu_1 \to \infty$, and one has $f_{T\infty} \to (\nu_s - \nu_i)/\nu_s$.

Tables 5.1, 5.2, and 5.3 show the predictions of this model for H_2, He, and Ar plasmas, respectively, for various mirror ratios, using the hybrid simplex velocity space approximation. Maxwellian rates are used for ionization, and the rate of 90° scattering of electrons with neutrals is used for ν_s. Figure 5.12 shows the Smith model compared with experimental data, in the limit of zero exit time.

A similar model for the special case of a solenoidal field may be of occasional use. Equating the ionization rate with constant plasma density from midplane to wall position W,

$$\frac{dN}{dt}\Big|_{ion} = \int_0^W n_g\, n_e\, \langle\sigma v\rangle_{ion}\, dz = n_g\, n_e\, \langle\sigma v\rangle_{ion}\, W \qquad (5.6.12)$$

to the reduced electron loss to the wall,

$$\frac{dN}{dt}\Big|_{el} = n_e \left(\frac{kT_e}{2\pi m_e}\right)^{1/2} \exp\left(-\frac{e\phi}{kT_e}\right) \qquad (5.6.13)$$

gives the solenoidal approximation to central plasma potential ϕ relative to the wall:

$$\phi_o = \frac{kT_e}{e} \ln\left[\frac{\left(\frac{kT_e}{2\pi m_e}\right)^{1/2}}{n_g \langle\sigma v\rangle_{ion} W}\right] \qquad (5.6.14)$$

Table 5.4 gives rank-differences correlation coefficients between the models presented in sections 5.3-5.6 and experimental observations. For helium no fit is particularly good, but for hydrogen and argon the Smith model works best. It is interesting that a model which is based essentially on the geometry of velocity space is generally successful in predicting γ. The agreement with theory is noticeably better than in the other models presented here.

Table 5.1

Smith model ϕ predictions for H_2

(volts, in $\nu_1 \to \infty$ limit)

T_e (eV)	Mirror Ratio 1.1	1.5	2	3	5
2.	17.42	17.42	17.42	17.40	17.23
3.	17.96	17.96	17.96	17.86	17.37
4.	18.54	18.54	18.52	18.27	17.37
5.	19.14	19.14	19.09	18.63	17.24
6.	20.31	20.31	20.21	19.53	17.67
8.	20.31	20.29	20.00	18.62	15.48
10.	21.53	21.49	20.95	18.85	14.41
12.5	22.69	22.59	21.65	18.49	12.16
15.	23.72	23.52	22.10	17.75	9.17
17.5	24.84	24.51	22.55	16.93	5.53
20.	26.02	25.55	23.01	16.03	-
25.	28.10	27.24	23.39	13.28	-
30.	28.47	26.97	21.32	6.22	-
40.	32.32	29.46	20.37	-	-
50.	35.75	31.49	18.42	-	-

Note: "-" indicates breakdown of the model for negative potentials

Table 5.2

Smith model φ predictions for He

(volts, in $\nu_1 \to \infty$ limit)

T_e (eV)	Mirror Ratio 1.1	1.5	2	3	5
2.	20.00	20.00	20.00	20.00	20.00
3.	27.75	27.75	27.75	27.73	27.51
4.	28.72	28.72	28.72	28.65	28.16
5.	29.62	29.62	29.62	29.45	28.62
6.	30.49	30.49	30.47	30.17	28.95
8.	32.02	32.02	31.95	31.28	29.16
10.	33.36	33.36	33.19	32.03	28.89
12.5	35.03	35.02	34.66	32.77	28.23
15.	36.58	36.55	35.94	33.22	27.15
17.5	38.21	38.14	37.23	33.61	25.92
20.	39.83	39.71	38.45	33.87	24.45
25.	43.26	43.01	40.97	34.34	21.17
30.	46.83	46.41	43.50	34.70	17.31
40.	54.26	53.41	48.63	35.21	6.94
50.	62.43	61.11	54.40	36.23	-

Note: "-" indicates breakdown of the model for negative potentials

Table 5.3

Smith model ϕ predictions for Ar

(volts, in $\nu_i \to \infty$ limit)

T_e (eV)	Mirror Ratio 1.1	1.5	2	3	5
3.	11.93	11.93	11.90	11.65	10.85
4.	13.81	13.81	13.75	13.32	12.10
5.	14.95	14.95	14.83	14.15	12.42
6.	16.14	16.13	15.94	14.98	12.73
8.	18.20	18.17	17.79	16.21	12.81
10.	20.34	20.28	19.68	17.44	12.80
12.5	21.14	21.00	19.94	16.55	9.83
15.	21.59	21.33	19.68	14.92	5.35
17.5	22.74	22.33	20.10	13.98	-
20.	23.54	22.92	20.02	12.31	-
25.	25.18	24.00	19.68	8.17	-
30.	27.55	25.95	20.08	3.97	-
40.	30.18	27.08	17.27	-	-
50.	32.92	28.04	13.53	-	-

Note: "-" indicates breakdown of the model for negative potentials

Table 5.4

Correlation coefficients between experimental data

and model predictions for γ

gas	No. cases	MODEL (1)	(2)	(3)	(4)	(5)	(6)	(7)
H_2	46	.445	.539	-.319	.263	.478	.279	.661
He	51	-.021	-.382	.136	-.21	-.374	-.452	-.111
Ar	82	.123	-.342	-.239	-.359	-.382	-.375	.623

Models:

(1)--Kaufman

(2)--Modified Kaufman

(3)--BenDaniel-Brambilla-Werkoff

(4)--BenDaniel-Brambilla-Werkoff with revised R and neutral scattering

(5)--Sprott

(6)--Modified Sprott

(7)--Smith

Figure 5.1 n vs. s for a DC-like mirror for hydrogen T_e = 10 eV; $n_g = 10^{18} m^{-3}$, R = 1.1.

Figure 5.2 n vs. s for a DC-like mirror for hydrogen T_e = 10 eV; $n_g = 10^{18} m^{-3}$; R = 2.

Figure 5.3 n vs. s for a DC-like mirror for hydrogen T_e = 10 eV; $n_g = 10^{18} m^{-3}$; R = 3.

Explanations for figures 5.1-5.3

R: mirror ratio T_e: electron temperature n_g: neutral gas density per cubic meter. (w/B): predictions using the model of this report, including magnetic field effects. (w/o B): predictions with the standard free fall model, neglecting the magnetic field.

Figure 5.4 Comparison of the numerical model of the present work with the solution of Self.

Figure 5.5 Free fall model numerical predictions of n vs. s for a magnetic field increasing away from midplane.

Figure 5.6 Free fall model numerical predictions of n vs. s for a magnetic field decreasing away from midplane.

L_M = magnetic scale length

L_{ion} = ionization scale length (see text)

Figure 5.7 η vs. z predicted from the free fall numerical model with a magnetic field like that of the DC Machine.

η profiles for three values of helium gauge pressure are given, as well the η values predicted in the zero B model.

η = dimensionless potential (see text)

s = dimensionless distance (see text)

Figure 5.8 Wall values of η vs. neutral pressure for the free fall numerical model.

Calculations are done for electron temperatures of 5, 10 and 20 eV.

Dashed lines: model without magnetic field effects

Solid lines: model with magnetic field effects

Data points: Helium data with the magnetic field as shown in fig. 5.7;

I_e = 220 A, I_H = 150 A, I_r = -560 A

Figure 5.9 Experimental γ vs. theoretical γ from the Kaufman model.

The points which have theoretical γ predictions of < 1 are those of the original model. The group of points with theoretical $\gamma > 2$ include the effects of neutral scattering.

Figure 5.10 Experimental γ vs. theoretical γ from the BenDaniel-Brambilla-Werkoff model.

Figure 5.11 Experimental γ vs. theoretical γ from the Sprott model.

Figure 5.12 Experimental γ vs. theoretical γ from the Smith model.

Figure 5.13 Theoretical values of γ from the Smith model, as a function of mirror ratio R.

$$w \equiv \frac{\nu_{ion}}{\nu_{ion} + \nu_{scat}}$$

In figures 5.9-5.12, the same experimental data points are plotted. A wide range of mirror ratios and fill pressures are represented.

$$\gamma = \frac{e\phi_o}{kT_e}$$

Figure 3.1 η vs. s in a DC-like mirror for hydrogen; T_e = 10eV; $n_g = 10^{18} m^{-3}$; R = 1.1.

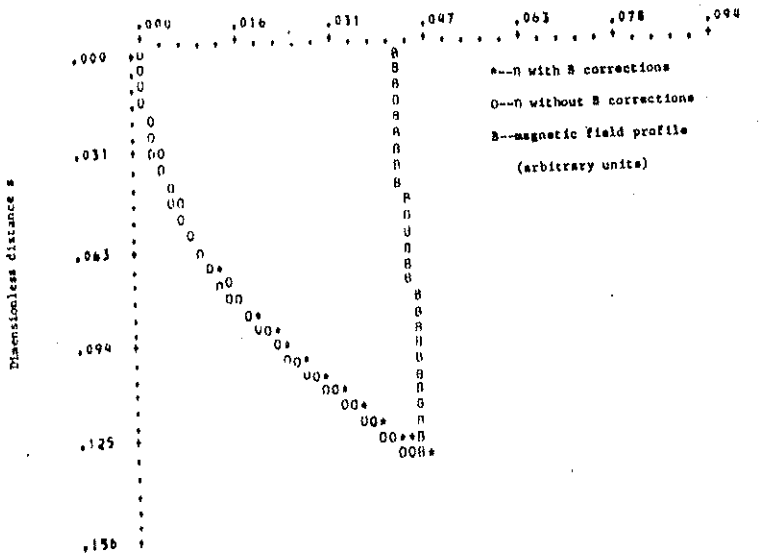

Figure 3.2 η vs. s in a DC-like mirror for argon; T_e = 5eV; $n_g = 10^{18} m^{-3}$; R = 2.

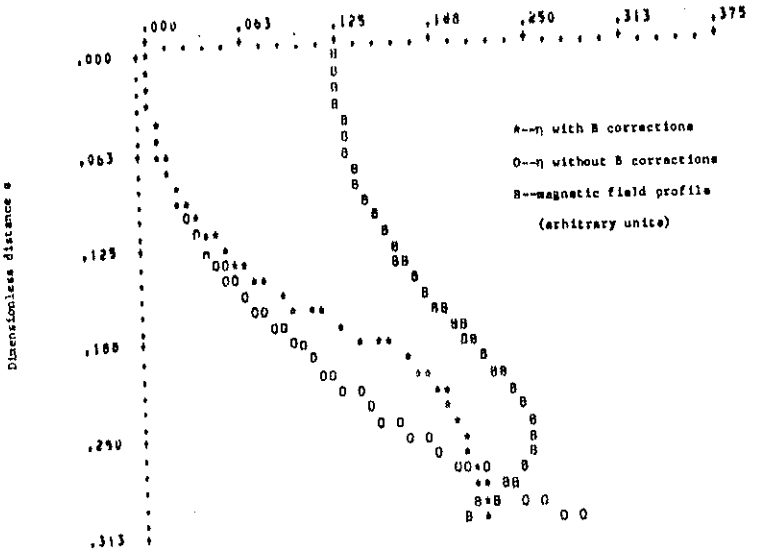

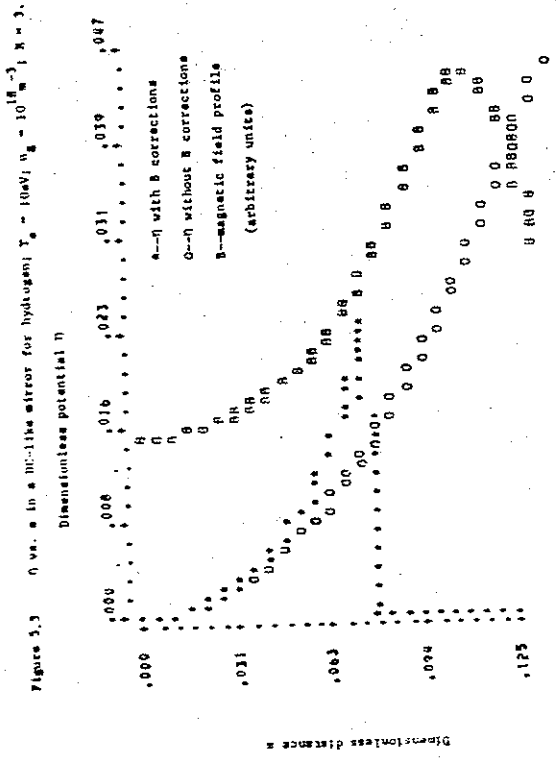

Figure 5.3 η vs. s in a Ni-like mirror for hydrogen; T_e = 10eV; $n_e = 10^{18}\,m^{-3}$; N = 3.

Figure 5.4 Comparison of the numerical model of the present work with the solution of Self.

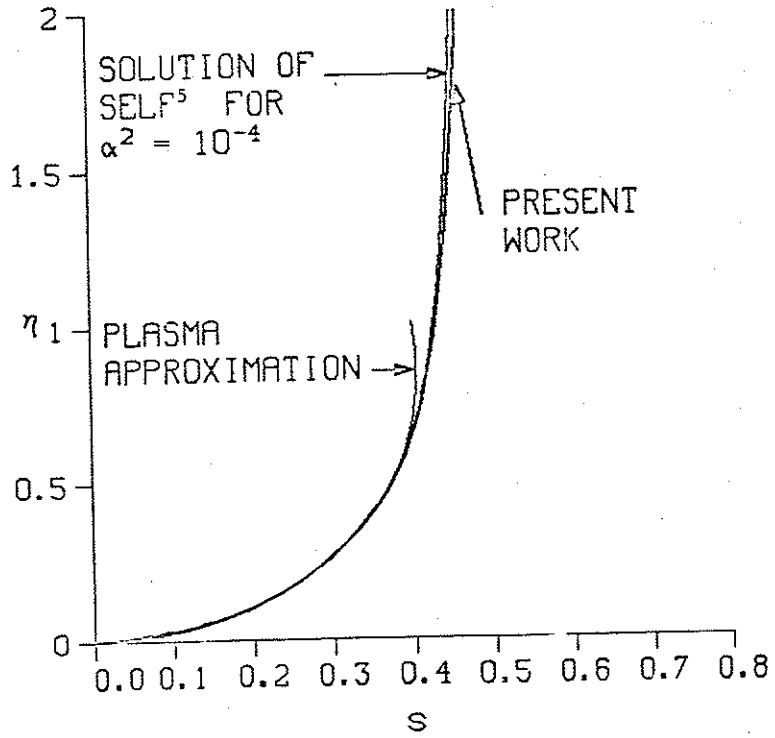

Figure 5.5 Free fall model numerical predictions of η vs. s for a magnetic field increasing away from midplane.

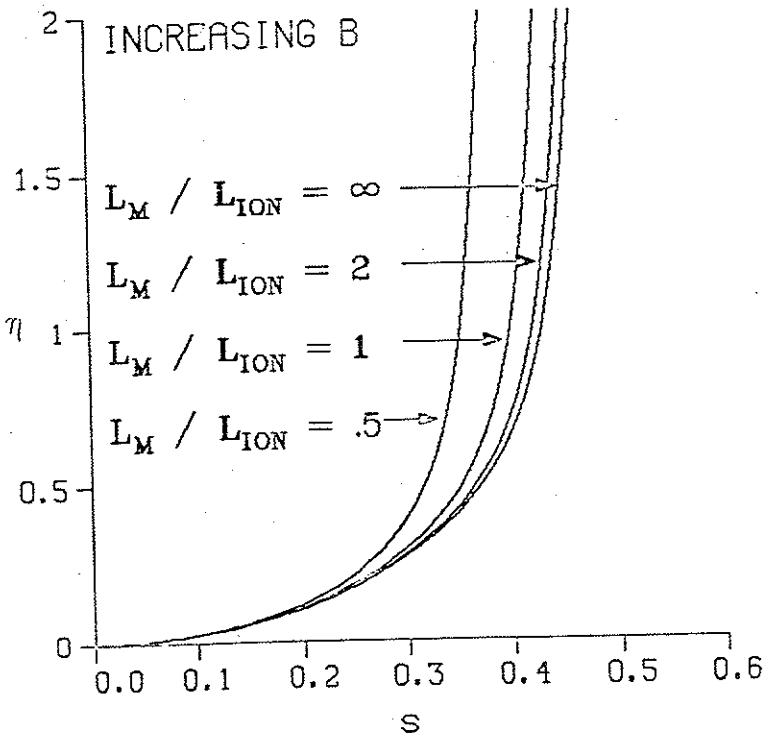

Figure 5.6 Free fall model mumerical predictions of η vs. s for a magnetic field decreasing away from midplane.

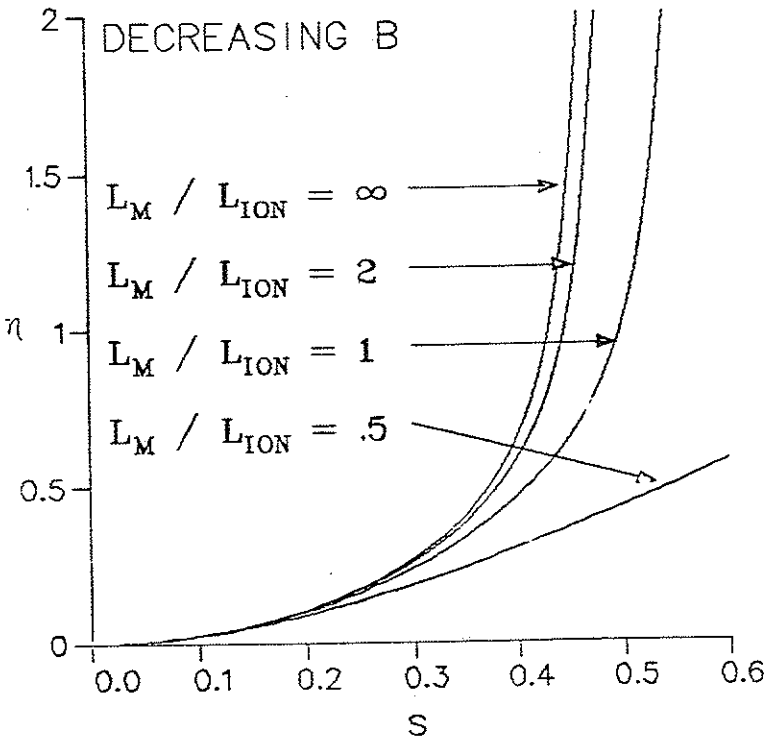

Figure 5.7 Free fall model numerical predictions of η vs. z for a magnetic field like that of the DC Machine.

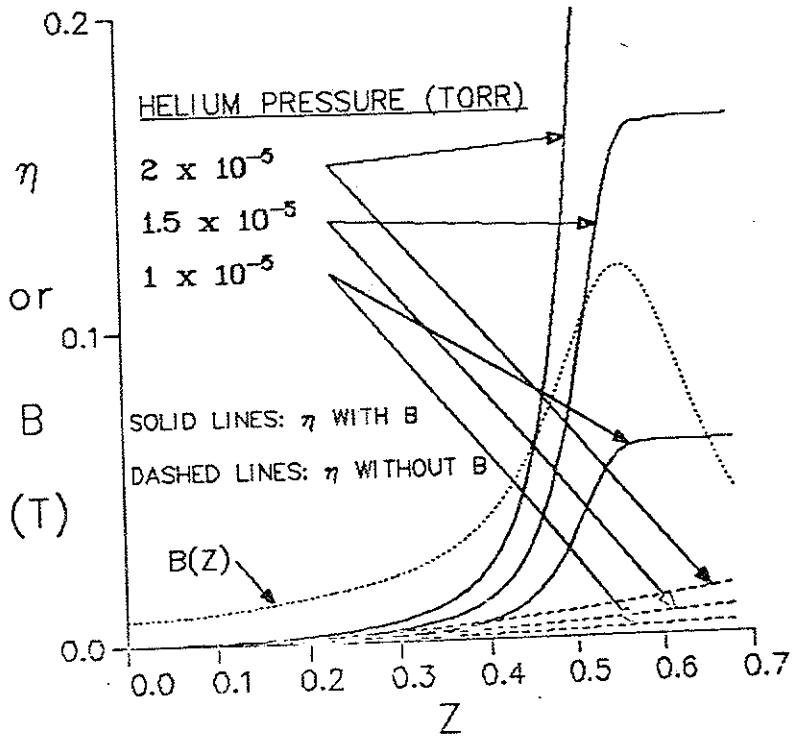

Figure 5.8 Free fall model predictions for η at the wall with and without a magnetic field similar to the DC machine, compared with experimental data.

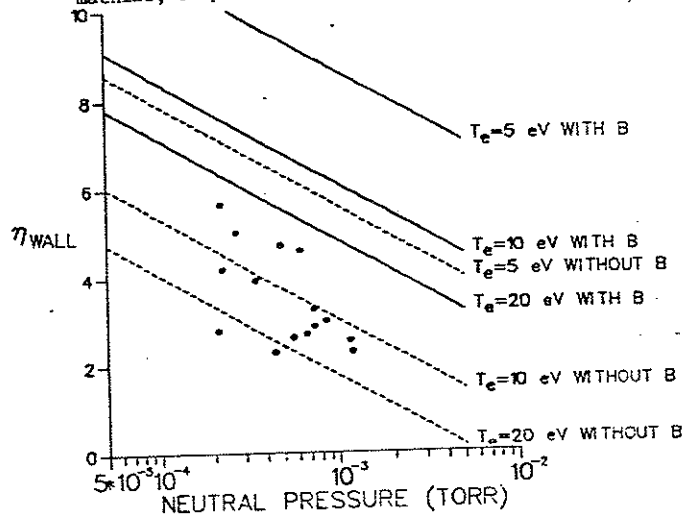

FIGURE 5.9 EXPERIMENTAL Y VS. THEORETICAL Y FROM THE KAUFMAN MODEL.

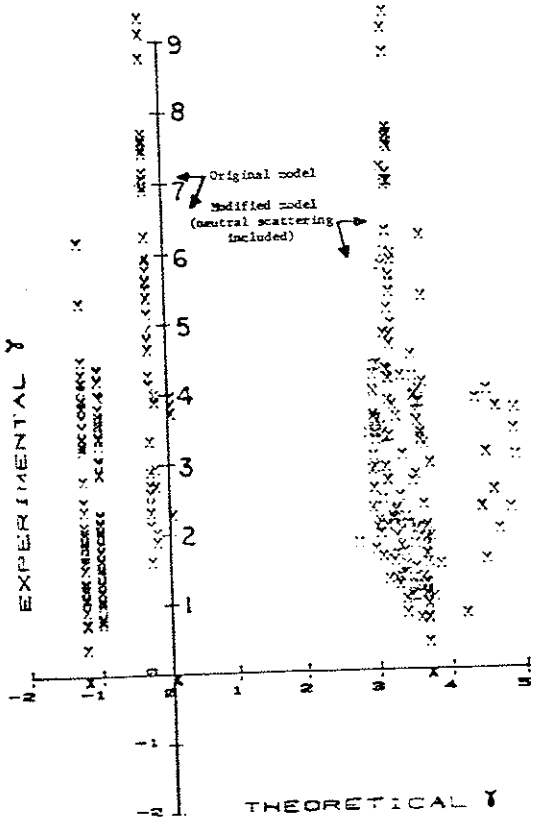

FIGURE 5.10 EXPERIMENTAL Y VS. THEORETICAL Y FROM THE BENDANIEL-BRAMBILLA-HERSOFF MODEL.

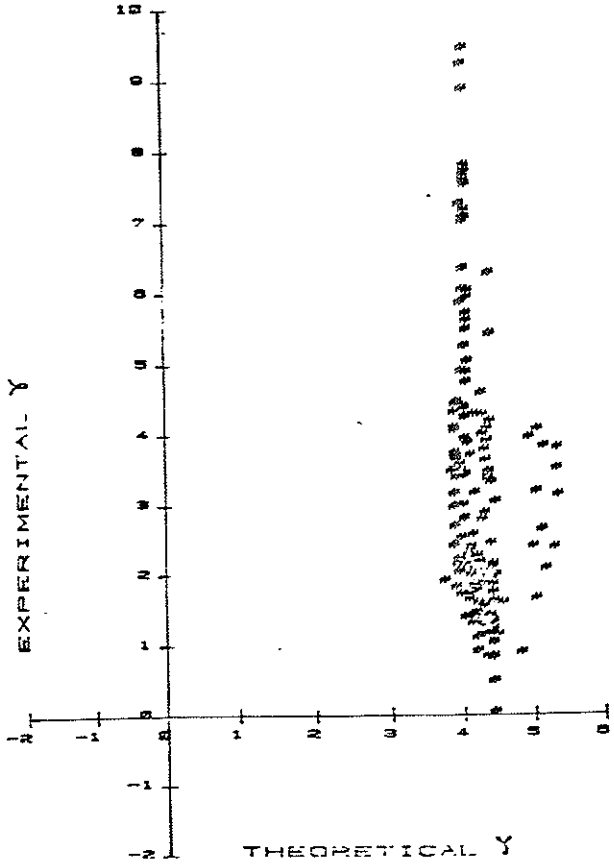

FIGURE 5.11 EXPERIMENTAL Y VS. THEORETICAL Y FROM THE SPROTT MODEL.

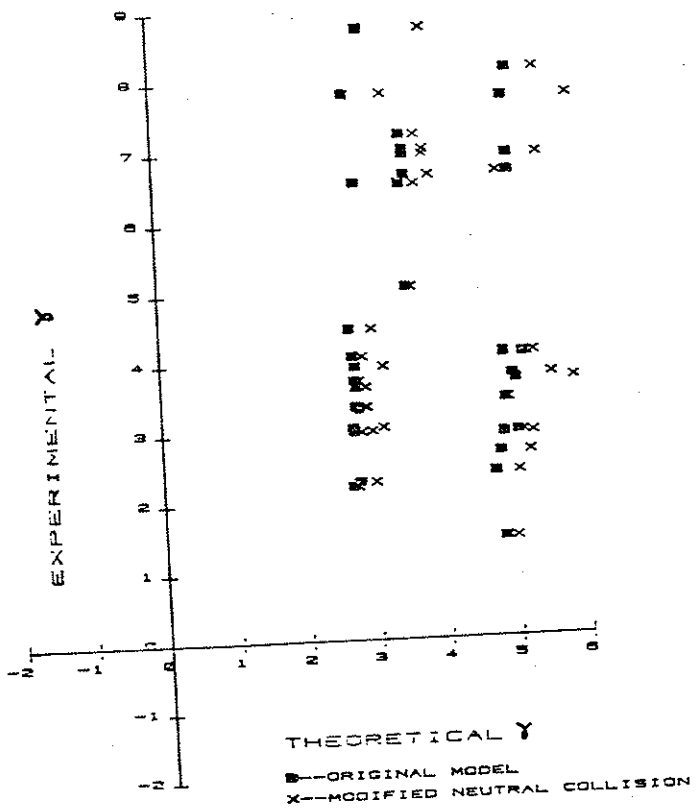

FIGURE 5.12 EXPERIMENTAL Y VS. THEORETICAL Y FROM THE SMITH MODEL.

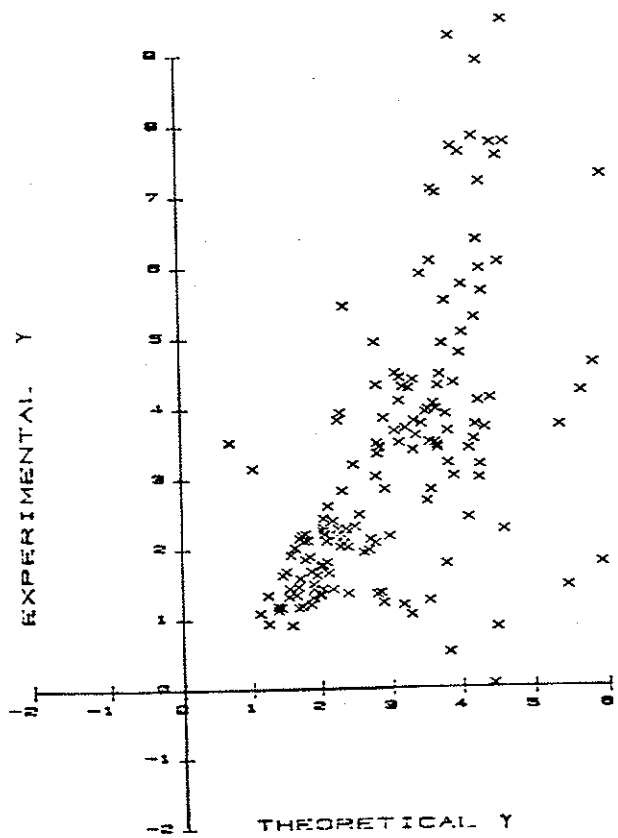

FIGURE 5.13 Υ VS. R IN SMITH MODEL.

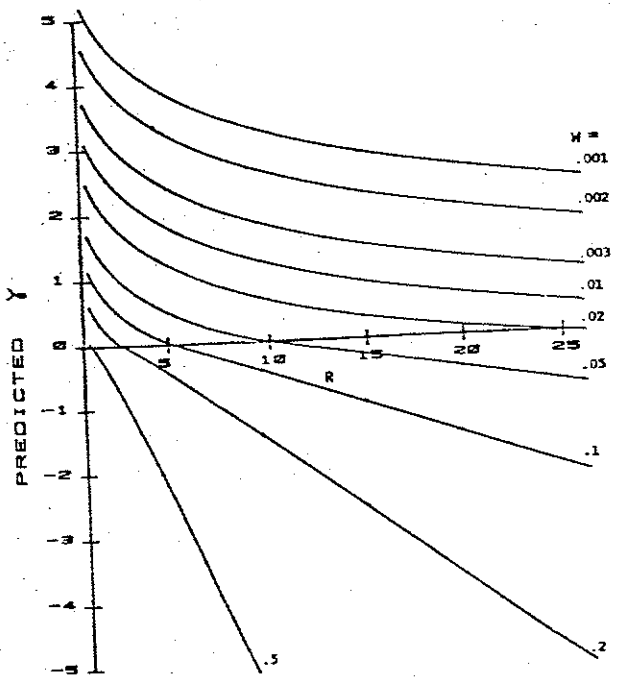

REFERENCES FOR CHAPTER 5

[1] L. Tonks and I. Langmuir, Phys. Rev. 34, 876 (1929).

[2] R. Fonck and W. Guss, PLP 584, (Sept.,1974).

[3] C. M. Strawitch, Ph. D. Thesis, University of Wisconsin, Madison, (March, 1981).

[4] E. B. Harrison and W. B. Thompson, Proc. Phys. Soc. 74, 2 (1959). (Cambridge: University Press, 1950) p. 229.

[5] S. A. Self, Phys. Fluids 6, 1762 (1963).

[6] S. A. Self, J. Appl. Phys 36, 456 (1963).

[7] G. A. Emmert, et. al., Phys. Fluids 23, 803 (1980).

[8] E. T. Whittaker and G. N. Watson, A Course on Modern Analysis, 4th ed. (Cambridge Univ. Press, Cambridge, England, 1952).

[9] P. K. Smith, PLP 886 (January, 1983).

[10] A. N. Kaufman, TID-7520 (Pt. 2), 387 (1956).

[11] D. J. BenDaniel, Plas. Phys. 3, 235 (1961).

[12] M. Brambilla and F. Werkoff, EUR-CEA-FG-552 (1980).

[13] D. J. BenDaniel and W. Carr, UCRL-5859, (1960).

[14] J. C. Sprott, PLP 484 (1972); PLP 518 (1973).

[15] J. Kesner, G. Knorr and D. R. Nicholson, Univ. of Iowa Report 80-11 (1980).

[16] S. Knight, Planet. Space Sci., 21, 741 (1973).

Chapter 6. Phenomena near the resonance zone

In this chapter the emphasis is on revealing the observed properties of plasma near the axial positions of the resonance zone. The picture that emerges is that the resonance zone in the DC Machine is characterized by a narrow (~ 1 cm) region of markedly reduced V_f, and of strongly increased density. These features have been noted obliquely in other research, but their significance in the present experiment suggests they have not received their proper attention.

6.1 Floating potential

Figure 6.1 is an example of the floating potential (V_f) given by a Langmuir probe as it is moved along the axis of the DC machine. The floating potential shows noticeable dips at axial positions very close to the resonant zones. That these are related to the resonance zone is supported by the following additional evidence:

(1) When the magnetic field is changed the dips move in the direction of the new location of the resonance zone.

(2) When a different frequency of microwaves is used, the dip occurs near the new value of magnetic field predicted for resonance.

This is demonstrated by figure 6.2, which compares the observed dip position with the position of cyclotron resonance predicted from the coil currents. Figure 6.3 shows the detail from a typical dip. The dips are seen in each of the gases used (hydrogen, helium, and argon) and have been observed with tank pressures of 10^{-5} torr to over 10^{-3} torr. Figure 6.4 gives the characteristic values of dip depth and width for each of these gases. With a full width at half maximum (FWHM) of ~1 cm, these dips are quite narrow compared with the vacuum wavelength of 12.2 cm., the magnetic field scale length of about 15 cm., and the electron mean free path of a few meters.

The depth of this "resonance zone dip" is $\sim 1 \times \frac{kT_e}{e}$ or 5-10 volts for a typical plasma. Table 6.1 gives information on the derived ΔV_f values by gas species.

V_f and V_p are related in simple probe theory by [4]

$$V_f = V_p - \alpha \times \frac{kT_e}{e} \qquad (6.1.1)$$

(6.1.1) implies V_f dips could be induced by a decrease in plasma potential V_p, an increase in kT_e, or both. There are, however, other possible explanations for a V_f decrease.

Using the high impedance method of finding V_f with insufficient input impedance may cause density peaks--such as are found near resonance--to produce spurious V_f structure. Appendix F gives details. In this experiment, this is not a problem if input impedances of 10MΩ or greater are used.

Another mechanism for driving V_f anomalously negative is the presence of large amplitude oscillations in the plasma. This is taken up in section 6.6, but to anticipate a result, this is an indequate explanation of the dips here.

When the Lisitano source is used as the plasma source, the floating potential and plasma potential profiles are realatively featureless, as shown in figure 6.5. When the 300 MHz source is used, the resonance field (111 gauss) is located near the midplane, and the dip is both broader and deeper than for the 2.45 GHz source, as shown in figure 6.6.

Within the stable range of operation of the S-band source, the V_f profile was insensitive to the power level, as shown in figure 6.7 In figure 6.8 the normalized dip depth, $\frac{e\Delta V_f}{kT_e}$, is plotted vs. helium gauge pressure for a series of data runs with I_e = 221, I_H = 150, I_r = -525, and S-band power P = 750 W. The dips are seen over the whole range of pressures studied.

6.2 Saturation currents

Both the ion and electron saturation currents show peaks near resonance. Figures 6.9a and 6.9b show the ion and electron saturation currents I_{is} and I_{es} for a single experiment (P = 10.5×10^{-5} torr He gauge, 750 W @2.45 GHz, B_{Max} = 1194g, B_{min} = 93g). It appears at first glance that the resonance peak is a minor feature in the electron curve. The difference between the curves is mainly because the electron collection capability of a probe changes drastically with magnetic field value. That this is the prime source of deviation is shown in figure 6.10, in which the ratio I_{es}/I_{is} is plotted vs. local magnetic field B. The result is that the electron saturation current is reduced by a factor proportional to $B^{-.39}$. When this factor is taken into consideration, the two curves are similar, as shown in figure 6.11. The relative size of the electron current peak is somewhat smaller than the ion current peak.

The differing transport rates of electrons along the field and perpendicular to the field were exploited by the two-surface probe shown in figure 6.12. The "parallel" surface was a disk facing into $\vec{B}$. The other "perpendicular" surface was a cylinder with an axis along $\vec{B}$. Near an electron's turning point the energy is mainly invested in $v_\perp$. The liklihood of collection by the cylindrical surface is maximized. Far from the turning point $v_\parallel$ dominates, and the electron is much more likely to be collected by moving along field lines to the disk than to move move across

field lines to the cylinder. If the electron turning point density (see Appendix C) peaks at a given position, this implies a peak of $I_\perp/I_\parallel$, the ratio of electron saturation currents at the "perpendicular" and "parallel" surfaces. Figure 6.13 shows a sample plot of $I_\perp/I_\parallel$ fo this probe. At high B the gyroradius of an electron is small. The effective collection area of the perpendicular surface is also small, so the minimum at the position of maximum B is not surprising. However, $I_\perp/I_\parallel$ has a peak at the resonance position. This is evidence of an accumulation of turning points near the resonance zone. Examination of $I_\perp$ and $I_\parallel$ separately show that both peak at the resonance zone.

As in the V_f profile, the resonance structure is seen on both sides of the magnetic field maximum.

The observed resonance I_{i-sat} was relatively reproducible, as shown by the three data sets displayed in figure 6.14. Sometimes a problem occured with "mode switching", between plasma regimes with differing but internally consistent profiles. It was unclear why the problem sometimes occured.

Figure 6.15a shows the ratio $\frac{I_{peak}}{I_{base}}$ vs. tank pressure. I_{base} is the minimum saturation current just interior to the resonance peak value I_{peak}. The ratio deceases slowly with pressure. Figure 6.15b shows the FWHM of the ion saturation peaks with pressure. The peaks do not broaden with pressure, but rather get narrower. This is contrary to what one would expect from the

argument that the effect of greater collisions at the higher pressure would tend to broaden any narrow features.

6.3 Electron temperature

The electron current is an exponential function of probe bias for a Maxwellian plasma, and the same value of T_e results no matter what part of the curve is chosen for analysis. This is not true for the perturbed distributions of the present experiments, especially near the resonance zone. It <u>is</u> possible to define a mean e-folding rate. The "T_e" obtained from the IV-plot analysis programs is of this form. Figure 6.16 shows the dependence of "T_e" at the midplane and at the resonance zone, with tank pressure. Figure 6.17 compares the size of the V_f dip for several cases with the increase of T_e at resonance compared with adjacent values. There is substantial difficulty in taking the difference of T_e at resonance and at adjacent points, since each has its own large uncertainty. Nevertheless the general message is that the magnitude of the T_e increase is on the order of that needed to explain the V_f dips.

In previous research of ECRH plasmas[5-11] a small fraction of superthermal electrons has often been reported. Searches were made for such electrons in the DC Machine by checking for x-ray induced scintillation attached via optical fiber to a photomultiplier tube, by checking to see if the count rate on a GM-counter adjacent to the machine were higher than background

when an experiment was in progress, and by checking the reading on a 0-200 milliroentgen pocket dosimeter placed beside a plexiglass covered port before and after an experiment. All methods gave negative results. "Cutie-Pie" radiation monitors were used as well, but the results were ambiguous since the zero level was affected by the change in magnetic field as they were moved. The radiation level escaping the DC Machine from superthermal electrons must be quite small, however.

6.4 Density

Langmuir probe measurements show a pronounced increase of the "ion saturation current"[1] as the probe is moved across a resonance zone. The ion saturation current scales as $nT_e^{1/2}$. T_e increases, but not enough to account for the size of the I_{is} peak. The bulk of the I_{is} peak is due to an actual density peak at the resonance zone. Other researchers[6,11-13] have also noticed a density peak in the vicinity of the resonance zone.

Figure 6.18 shows the size of the density peak at resonance, derived from I_{is} and T_e, as a function of position for a given experiment. T_e is also plotted to make it clear that both T_e and n peak. The pre-peak minimum is typical.

An alternative explanation not requiring a local density peak is that the enhanced "ion current" collected is in fact, an excess of secondary electrons emitted by the probe (in response to a local enhancement of high energy primary electrons). Ioffe, et. al.[3] used this explanation for their ECRH experiment. There are several reasons why this doesn't apply to the plasmas investigated here. If high energy electron flux were responsible for a fake I_{is} curve, then these electrons would have to be several hundred eV to produce a secondary electron flux of sufficient size to explain the I_{is} peak. For example, platinum, frequently used in probe tips, emits a maximum of 1.8 secondary electrons for each primary electron, at the optimum primary energy of 700 eV.[2] If a probe were contaminated with oxides or alkali halides, the secondary electron emission can increase by about a factor of two. The probe bias covers the range ±50 V, so that there should be relatively little effect of probe bias on the emitted electron flux, so long as the probe is negative with respect to the plasma. The effect of secondary electrons is thus to move the entire portion of the curve more negative than V_p, toward the region of ion collection. What is observed is that the ion current level and the slope of the ion current with respect to bias increase.

The latter effect is consistent with a real density increase, but not with the secondary electron effect.

The ion saturation peaks have a FWHM comparable with that of the V_f dip. Figure 6.19 shows a comparison of the typical resonance width and other length scales of interest.

6.5 Plasma potential

Basic probe theory allows changes in floating potential from either changes in the plasma potential or in electron temperature.

$$V_f = V_p - \alpha \times \frac{kT_e}{e} \qquad (6.5.1)$$

where α is a dimensionless constant of value 3-6, depending on ion mass and magnetic field.

Emissive probe data indicate a small (~ 1V) decrease of V_p near resonance. Figure 6.20 shows the V_f and V_p structure near resonance for a particular case. The point is that $\Delta V_p \ll \Delta V_f$, and so the floating potential dip can not be due to a corresponding dip in plasma potential. Many emissive profiles were taken, concentrating on the resonance zone to get the magnitude of V_p dips, but the dips found, ~ 1 V, merge into the noise region so that few quantitative conclusions can be drawn.

This means thermal effects are the prime cause of the V_f dips, as implied earlier. While the observed V_p dips are low compared with T_e, they are comparable with T_i. This can be explained by a four-species quasineutrality model with the following plasma components:

(1) Near-resonance-turning electrons. Near resonance the density is modeled by a Gaussian peak. Below a junction point (the low side of the peak where the density has fallen to half of maximum) these are given by the ideal sloshing formula:

$$n_{er} = \alpha \exp[-k(z-z_R)^2] \qquad z > z_R - \frac{FWHM}{2} \qquad (6.5.1)$$

$$= n_o \tau_e \frac{B}{B_o} \left(\frac{B_R - B_o}{B_R - B}\right)^{1/2} \qquad z < z_R - \frac{FWHM}{2}$$

(2) Background Maxwellian electrons. The density of these is given by

$$n_{em} = n_o (1-\tau_e) \exp\left(\frac{e(\phi-\phi_o)}{kT_e}\right) \qquad (6.5.2)$$

(3) Background Maxwellian ions. The density of these is given by

$$n_{im} = n_o (1-\tau_i) \exp(-e(\phi-\phi_o)/kT_i) \qquad (6.5.3)$$

(4) Streaming ions. These are introduced to maintain similarity with tandem mirror models. In this experiment their role is to represent the ions passing through the resonance zone with the "free-fall" energy obtained from their position of ionization near

the midplane. Their density is given by the condition that their parallel particle flux be constant within a magnetic flux tube.

$$n_{is} = n_o \tau_i \frac{B}{B_o} \left(\frac{E}{E-e(\phi-\phi_o)}\right)^{1/2} \qquad (6.5.4)$$

The input variables of the 4-species program are the Maxwellian electron temperature T_e, the ratio of resonance magnetic field to midplane magnetic field r, the length between midplane and resonance zone L, the ratio τ_i of passing ion density to total ion density at the midplane, the passing ion energy E, the Maxwellian ion temperature T_i, the ratio of density of resonance-turning electrons to total electron density at midplane τ_e, and the FWHM of the resonance turning electrons. α is chosen to maintain continuity of electron density across the transition point, and k is determined by the FWHM:

$$\alpha = 2 \tau_e r_h \left(\frac{r-1}{r-r_h}\right)^{1/2} \qquad (6.5.5a)$$

$$k = \frac{4 \ln 2}{(FWHM)^2} \qquad (6.5.5b)$$

where $r_h = B(z_h)/B(0)$.

Figure 6.21a and 6.21b show the plasma potential profiles consistent with a small and large density increase at resonance, respectively. The dip depth is found to scale as $\sim 1.1 \frac{kT_i}{e} \ln\left(\frac{n_{max}}{n_o}\right)$.

The scaling of dip depth with density peak ratio and T_i/T_e is shown in figures 6.22 and 6.23, respectively. It is clear from this model the reason why plasma potential dips are so small in the present experiment is that T_i is small. The incipent potential well is virtually filled by the cold ion component. Figure 6.24 shows the dependence of relative resonance dip $e\Delta V_p/kT_e$ and $n_{res}/n_o - 1$ on the fraction of resonance-trurning electrons, with conditions similar to those that prevail in the present experiment. From the engineering standpoint, this graph can be viewed with axes inverted to find the required midplane fraction of resonance-turning electrons to meet a goal of attaining a particular value of $e\Delta V_p/kT_e$.

6.6 Fluctuations

It is necessary to examine the role of noise near the resonance zone as a possible cause of the V_f dips. In the presence of a fluctuating potential between probe and plasma, due either to imposition of oscillation at the probe, to noise inherent in the plasma, the floating potential of the probe will be lower will be lower than in the absence of oscillation. The reason is the non-linearity of the IV trace. An oscillating sinusoidal potential of magnitude V_{ac} will cause an increase of the electron current of size,

$$\delta I_e = I_e(V_{dc})\, I_0\left(\frac{eV_{ac}}{kT_e}\right) \qquad (6.6.1)$$

where $I_e(V_{dc})$ is the electron current for the mean voltage value V_{dc}, I_0 is the modified Bessel function of the first kind of index 0, and $\frac{kT_e}{e}$ is the equivalent electron temperature in volts. This is altered by a multiplicative factor of order unity if the oscillation is not sinusoidal.[15]

The angular frequency of oscillation, ω, does not appear in (6.6.1). For low frequencies the increase in I_e is independent of ω, but as the plasma frequency ω_p is approached, the amplitude of δI_e increases. It decreases to zero if the oscillation frequency is increased still further. The structure of δI_e vs. ω is the province of "resonance probe" theory, which is detailed in references 2-9. The dc and ac components of V_f were measured point-by-point in the vicinity of the resonance zones. No correlation was seen between large amplitude noise and low V_f values, though there was some increase in small amplitude noise. Could fluctuations at this level account for the observed dips in V_f? The effect of oscillations on V_f is that the increase of electron current given by equation 6.6.1 must be matched by a more negative dc probe bias; the average electron current continues to equal the constant ion current:

$$\exp\left(\frac{-e\delta V_f}{kT_e}\right) = I_0\left(\frac{eV_{ac}}{kT_e}\right) \qquad (6.6.2a)$$

$$\delta V_f = -\frac{kT_e}{e} \ln I_0\left(\frac{eV_{ac}}{kT_e}\right) \qquad (6.6.2b)$$

The result is shown in figure 6.25, which reveals that a dip of $\delta V_f \sim \frac{kT_e}{e}$ requires an oscillation amplitude of $\frac{eV_{ac}}{kT_e} \sim 2$. The observed enhanced noise is only about $\sim .01-.02\ kT_e/e$, insufficient by more than an order of magnitude.

The attenuation of fluctuations in a probe circuit can be estimated from the model of figure 6.26. The sheath resistance, $R_s = \left(\frac{dI}{dV}\right)^{-1}\Big|_{V_f}$ is in series with a parallel combination of the probe capacitance to ground, C_s, and the input resistance and input capacitance of the measuring instrument, R_i and C_i, (e. g., 1 Mhz and 15 pF for a 1Al Tektronix plug-in.

The sheath resistance can be calculated for a given probe size and plasma, or can be measured directly from an IV plot. For typical conditions $R_s \sim .2\text{-}1\ M\Omega$. The value of C_s is the result of the ~30pF/foot capacitance of coaxial cables leading from the probe, in addition to capacitance to ground of the probe body itself. It is normally a few hundred picofarads. This means the normal probe circuit acts as a low pass filter with a corner frequency of only a few 10's of kilohertz:

$$\frac{|V_{out}|}{|V_{in}|} = \frac{R_i}{R_i + R_s\left(1 + \omega^2 R_i^2 (C_i + C_s)^2\right)^{1/2}} \qquad (6.6.3)$$

The LL5 spectrum analyzer shows the noise spectrum falling off rapidly well before the corner limit is reached. A typical noise spectrum is shown in figure 6.27. This suggests that the plasma noise is of such low frequency that no heroic methods need be employed in its measurement. To confirm this, a Hewlett-Packard 851B spectrum analyzer was connected via a short unshielded wire to a probe with only 15 pF capacitance to ground, and with a relatively large probe tip (2.85 cm^2) to reduce sheath resistance. In the frequency range 0-1 Ghz, which encompasses the plasma frequency, no plasma features were seen above 30 Mhz. The only observed effect was a broadening of the edge of the zero frequency peak, which may have been caused by noise much less than 30 Mhz. When plasma noise is observed on the oscilloscope, the trace may be erratic or show a 2-10 khz instability, but in either case is still well defined, implying the insignificance of higher frequency components.

The presence of a large fluctuating potential also reveals itself in the IV trace as an extended linear region around the inflection point, with a length on the order of the amplitude of the fluctuation. Thus one is warned when data may be suspect because of excessive noise. The observed length of the linear inflection regions gives a value of V_{ac} too small to cause the V_f dips.

6.7 Discussion of resonance zone dip size.

To find out how wide the resonance zone structure will be in other devices, it is useful to compare the widths with other mirror scale lengths.

Since the turning point is determined not by z explicitly, but rather by B, a more meaningful way of categorizing resonance width may be to express it in the dimensionless ratio $\frac{\Delta B}{B_r}$, where ΔB is the range of magnetic field value across the FWHM of the resonance zone I_{sat} peak, and B_r is the resonance value of magnetic field. There was considerable scatter in the data, which did not appear to be correlated with mirror ratio, gas pressure, or any other obvious variable. The mean values for the cases of greatest reliability are

Hydrogen, S-band source $\quad \frac{\Delta B}{B_r} = .09 \pm .035$

Helium, S-band source $\quad \frac{\Delta B}{B_r} = .16 \pm .085$

Argon, S-band source $\quad \frac{\Delta B}{B_r} = .105 \pm .065$

By comparison, the effective width of a resonance zone with the assumption of constant parallel speed is [16]

$$\Delta z \ (v_i \text{ constant}) = (v_i \ / \ \frac{d\omega}{dz})^{1/2} \qquad (6.7.1)$$

This is the "non-adiabatic region" outside of which the particle is effectively out of phase with the ECRH field and the particle velocity is not appreciably altered by the presence of ECRH. This means that the dimensionless width is

$$\frac{\Delta B}{B_r}\ (v_\parallel \text{ constant}) = \left[\frac{m v_\parallel}{e}\frac{dB}{dz}\right]^{1/2} \qquad (6.7.2)$$

For typical DC Machine parameters of $\frac{dB}{dz}\big|_r = .75$ T/m and $T_e = 10$ eV, $\Delta z\ (v_\parallel \text{ constant}) = .0033$ m, or $\Delta B/B_r = .0025$.

For an electron that turns at the resonance zone the acceleration near the turning point is $\frac{\mu}{m} B' = \frac{\mu}{e}\omega_c'$. Here μ is the magnetic moment, B' is the [locally constant] magnetic field gradient, and ω_c' is the gradient of the cyclotron frequency. This gives the time for a phase slip of $\pi/2$ radians between $\vec{v}$ and $\vec{E}$ from resonance:[18]

$$\Delta t\ (v_\parallel = 0) = \left(\frac{3\pi e}{\mu \omega_c'^2}\right)^{1/3} \qquad (6.7.3a)$$

The corresponding length is $$\Delta z = \left(\frac{9\pi^2 \mu}{e\omega_c}\right)^{1/3} \qquad (6.7.3b)$$

For typical numbers $\Delta z\ (v_\parallel = 0) = .0019$ m, or $\Delta B/B_r \sim .016$.

Cannobio[18] considers the situation in which μ varies and electrons are subject to space-charge constraints on $\dot{v}_\parallel$. He gives the resonance-turning interaction width as

$$\Delta z\ (v_\parallel = 0) \sim 1.4\ \left(\frac{m_e}{m_i}\frac{g^2}{\delta^3}\right)^{1/5} \qquad (6.7.4)$$

where $\delta = \frac{c}{\omega}\frac{1}{B_r}\frac{dB}{dz}\big|_r$ and $g = \frac{eE}{m\omega c} = \frac{E}{cB_r}$, with E the rf electric field intensity. For DC Machine parameters $\Delta z\ (v_\parallel = 0) \sim .0017$ m, or $\frac{\Delta B}{B_r} \sim .0013$.

The point of these calculations is to show that the observed peak of I_{sat} is significantly broader than can be expected from considering the width of the ECRH power absorption region. Thus collisionality or some other mechanism is responsible for broadening the peak. The purpose of the next chapter is to formulate models that can predict the resonance zone behavior by finding steady state distribution functions in the presence of both ECRH and collisions.

Table 6.1

Mean Values of Resonance Variables

Variable	Background gas type H_2	He	Ar
FWHM for ΔV_f	1.6 ± 1.1 cm	1.85 ± 1 cm	1.9 ± 1.3 cm
$\frac{\Delta V_f}{kT_e}$	.82 ± .39	1.27 ± .4	2.4 ± .85
$\frac{\Delta B}{B_r}$	.09 ± .035	.16 ± .085	.105 ± .065

Figure 6.1 Typical floating potential profile in the DC Machine.

Figure 6.2 Observed position of floating potential minimum vs. predicted resonance zone position.

Figure 6.3 Detail from a typical floating potential dip at the resonance zone.

Figure 6.4 Characteristic depths and widths of floating potential dips.

Figure 6.5 Floating potential and plasma potential with the Lisitano coil sourece.

Figure 6.6 Floating potential profile with the 300 MHz source.

Figure 6.7 Floating potential vs. position for three power levels.
Argon data at 3.7×10^{-5} torr $I_e = 252$ A, $I_H = 150$ A, $I_r = -1100$.
The V_f profile is not changed greatly at different powers.

Figure 6.8 Normalized dip depth $\frac{e\Delta V_f}{kT_e}$ vs. pressure.
Data is taken with $I_e = 221$, $I_H = 150$, $I_r = -525$, and an S-band power of 750 W in helium. Dips persist over the pressure range studied.

Figure 6.9a Ion saturation current profile.
A prominant peak is seen at the resonance zone position. Usually there is a steep fall-off on the wall side of the resonance zone.

Figure 6.9b Electron saturation current profile.
The resonance peak exists, but a weak central magnetic field allows a strong electron current near midplane, causing the peak to look less impressive.

Figure 6.10 Ratio of electron saturation current to ion saturation current vs. magnetic field strength.
The electron current falls off as $\sim B^{-.39}$, relative to the ion current.

Figure 6.11 Normalized electron saturation current and ion saturation current vs. position.

Figures 6.9a, 6.9b, 6.10 and 6.11 refer to the same experiment, in which $B_{Max} = 1195$ g, $B_{min} = 93$ g, mircrowave power was 750 W at 2.45 GHz and the gauge pressure was 10.5×10^{-5} torr helium.

Figure 6.12 Two surface probe for turning point study.

Figure 6.13 $I_\perp/I_\parallel$ vs. position.
Trace was obtained with the probe of figure 6.12. The anomalous peak is evidence for an accumulation of turning points.

Figure 6.14 Ion saturation current vs. z for three successive trials.
The resonance structure is reproducible.

Figure 6.15a $\frac{I_{peak}}{I_{base}}$ vs. pressure.

Figure 6.15b FWHM of ion saturation current peak vs. pressure.

In figure 6.15a and 6.15b the tank gas is helium. Coil currents for these data points are $I_e = 220$, $I_H = 150$, $I_r = -525$. The relative peak size decreases slowly with pressure. The peaks are narrower at higher pressure, an unexpected finding. The inclusion of loss region effects is essential to understanding this dependence.

Figure 6.16 Electron temperature at midplane and resonance zone as a function of tank pressure.

Figure 6.17 ΔV_f at resonance vs. ΔT_e.
Local T_e increases are apparently responsible for the V_f dips.

Figure 6.18 Density and temperature profile near resonance.
Coil settings: $I_e = 220$, $I_H = 158$, $I_r = -530$.
RF Power: 750 W. Gas: Helium, 8×10^{-5} torr gauge.
Both T_e and density peak at the resonance zone.

Figure 6.19 Resonance width and other length scales of interest in the DC Machine.

Figure 6.20 V_f and V_p profiles compared.
RF Power 695 W @2.45GHz. Argon gas, 10^{-4} torr gauge. $I_e = 265$ A, $I_H = 150$ A, $I_r = -670$ A. The dips in V_p at resonance are very small compared to the V_f dips.

Figure 6.21a Density and potential profiles from the 4-species model (small peak).

Figure 6.21b Density and potential profiles from the 4-species model (large peak).
In 6.21a and 6.21b the FWHM of the peak is fixed at .04 m.

Figure 6.22 Plasma potential dip at resonance zone vs. density peak ratio, from the 4-species model.
The behavior is logarithmic in $\frac{n_{res}}{n_o}$ for a given T_i.

Figure 6.23 Relative plasma potential dip at resonance zone vs. relative ion temperature, from the 4-species model.
The normalized dip depth is directly proportional to T_i for a given density peak ratio, 2.3 in this case.

Figure 6.24 Dependence of relative density peak and potential dip on fraction of resonance-turning electrons, from 4-species model.
The fraction of resonance turning electons at midplane, τ_e, is an independent parameter in the model. Both $\frac{e\Delta V}{kT_e}$ and $n_{res}/n_{cen} - 1$ are seen to scale approximately linearly with τ_e.

Figure 6.25 Normalized V_f dip caused by voltage oscillations vs. normalized oscillation amplitude.
The amplitude of the V_f dip is determined by the condition that the time-averaged ion and electron currents to the probe be equal. Note that the oscillation magnitude required to drive a spurious $\Delta V_f \sim \frac{kT_e}{e}$ is quite large.

Figure 6.26 Simplified model of probe-plasma circuit.
R_s = sheath impedance of probe. C_s = capacitance to ground of probe and cables, up to the measuring device. R_i, C_i = input resistance and capacitance of measuring device.
The probe-plasma circuit acts as a low-pass filter.

Figure 6.27 Spectrum of noise seen in the DC Machine during a typical experiment.
The noise falls off roughly exponentially with frequency, and is very small above 10 KHz.

FIGURE 6.1 TYPICAL FLOATING POTENTIAL PROFILE IN THE DC MACHINE

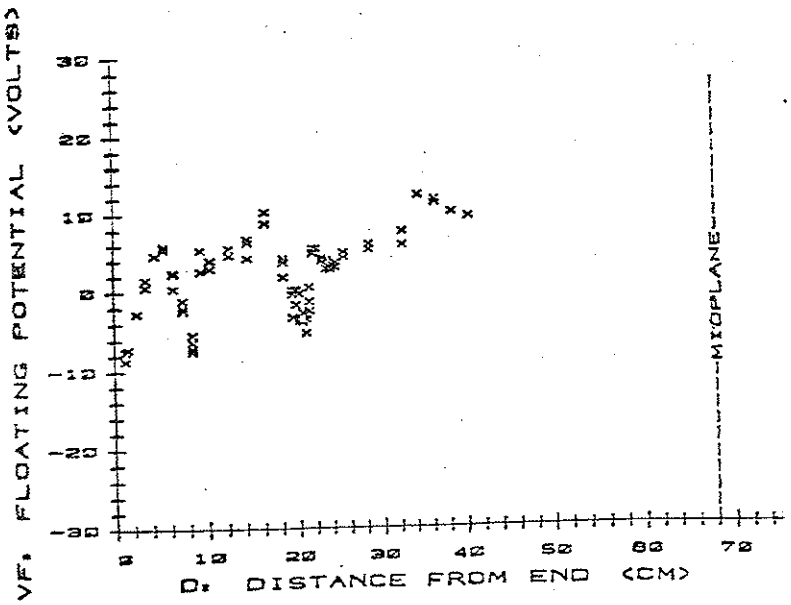

FIGURE 6.2 OBSERVED POSITION OF FLOATING POTENTIAL MINIMUM VS. PREDICTED RESONANCE POSITION

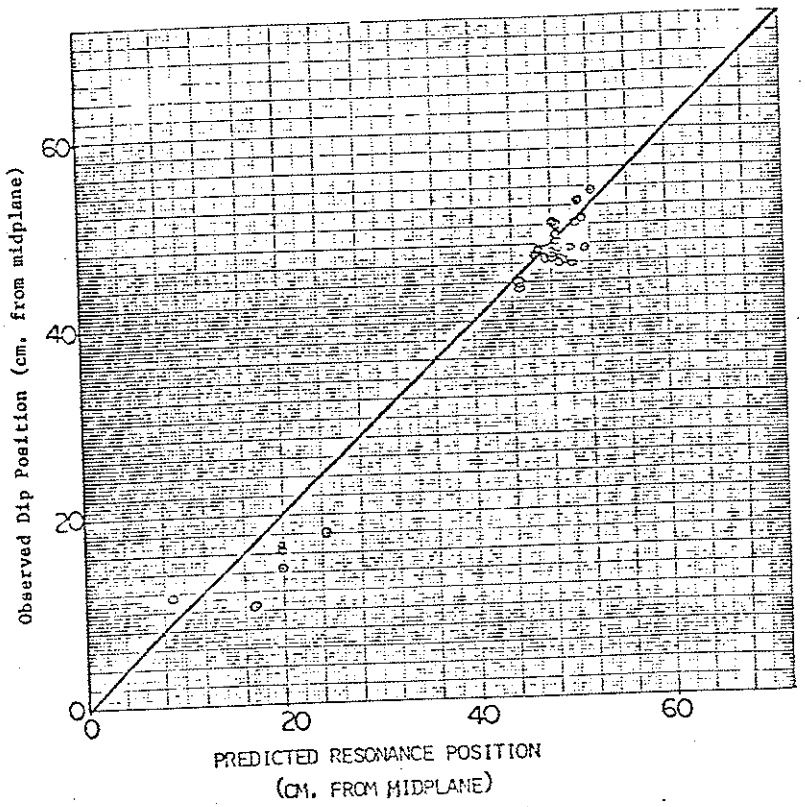

Figure 6.3

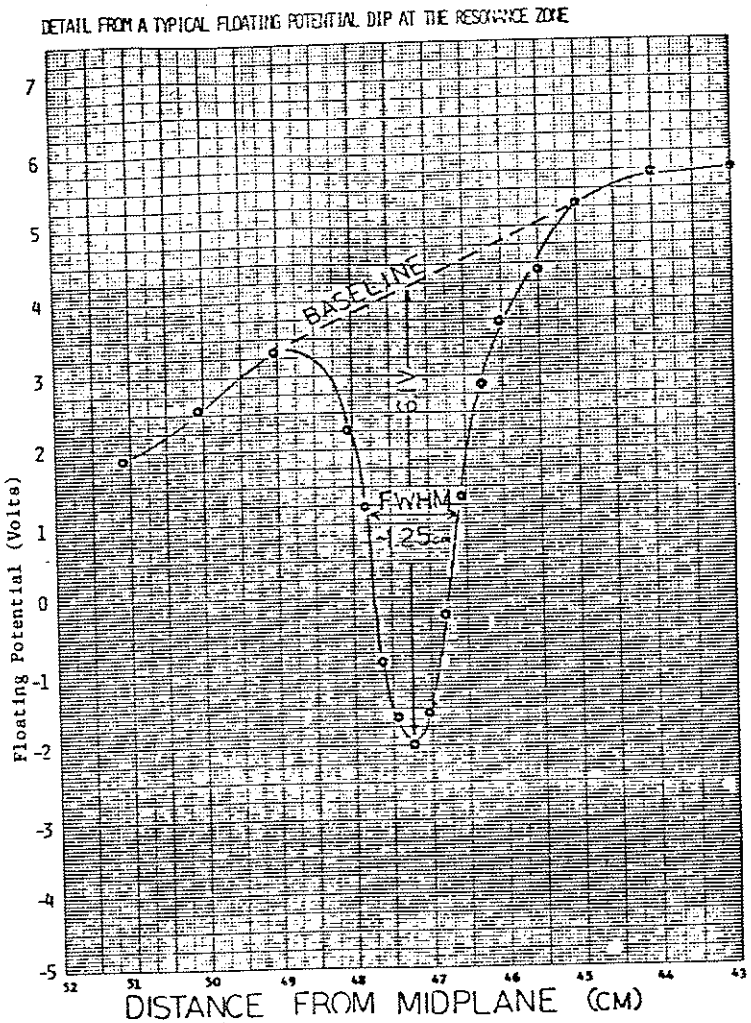

Figure 6.4 Characteristic values of V dip depth and FWHM

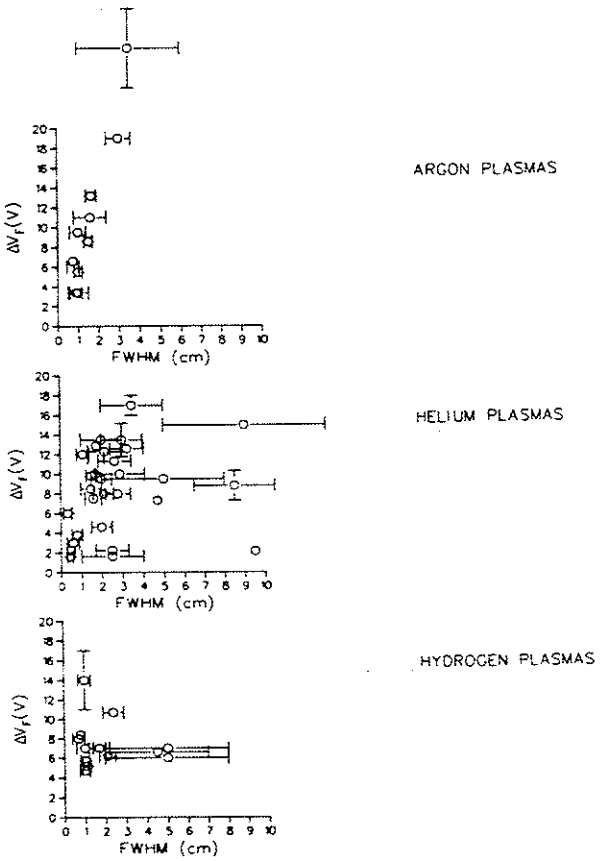

FIGURE 6.5 FLOATING POTENTIAL AND PLASMA POTENTIAL PROFILES WITH THE LISITANO SOURCE.

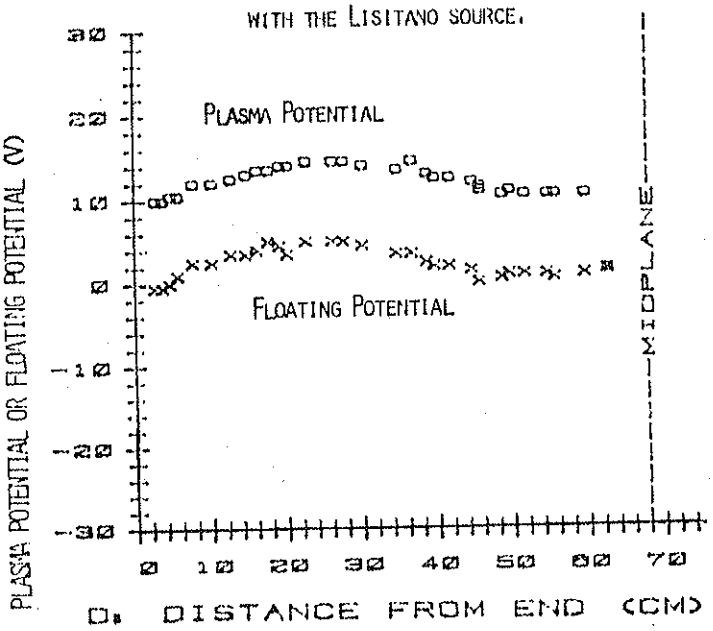

FIGURE 6.6 FLOATING POTENTIAL PROFILE WITH THE 300 MHz SOURCE.

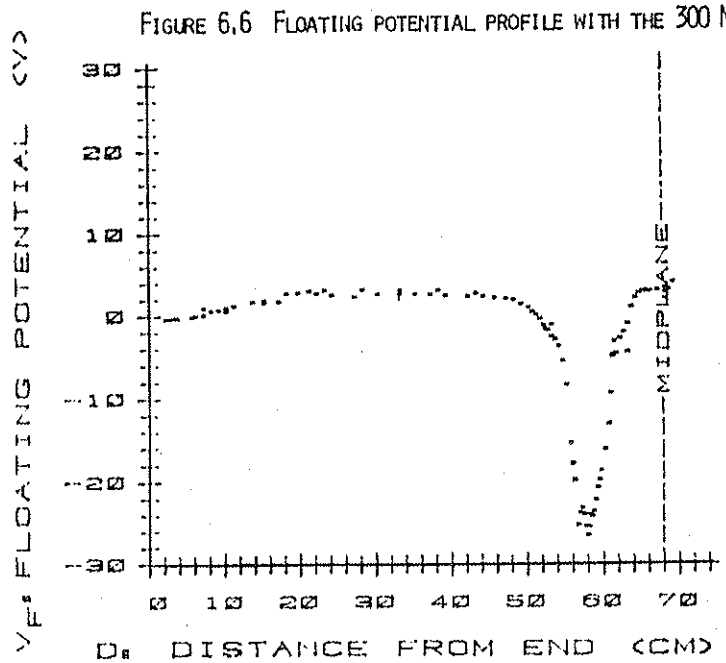

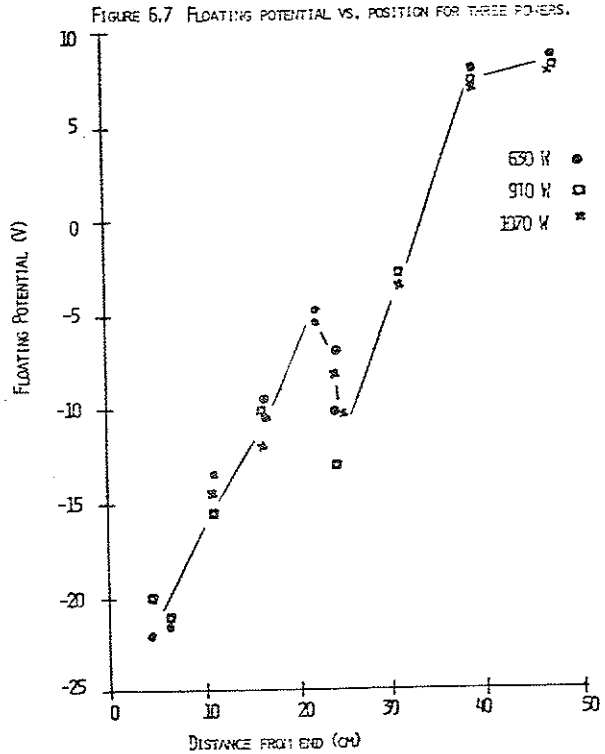
FIGURE 6.7 FLOATING POTENTIAL VS. POSITION FOR THREE POWERS.
FLOATING POTENTIAL (V)
DISTANCE FROM END (CM)
630 W
910 W
1270 W
10
5
0
-5
-10
-15
-20
-25
0
10
20
30
40
50

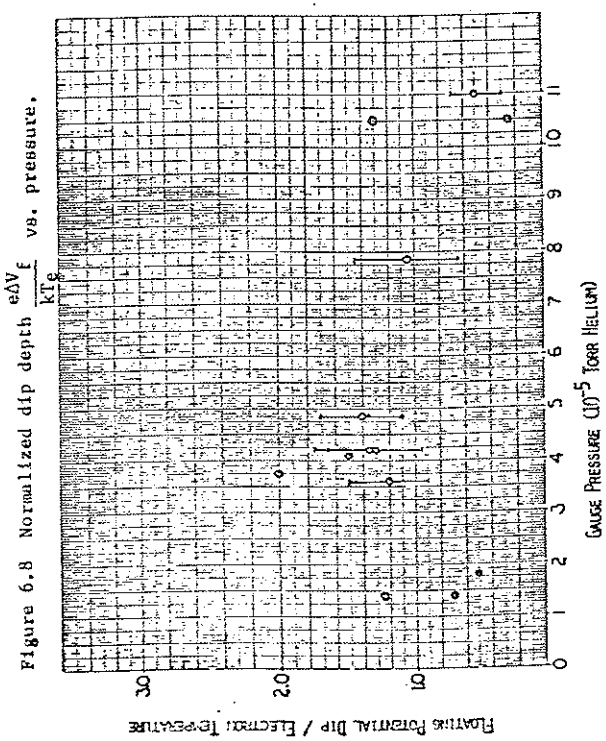
Figure 6.8 Normalized dip depth $\frac{e\Delta V_f}{kT_e}$ vs. pressure.
FLOATING POTENTIAL DIP / ELECTRON TEMPERATURE
GAUGE PRESSURE (10^{-5} TORR HELIUM)
3.0
2.0
1.0
0
1
2
3
4
5
6
7
8
9
10
11

Figure 6.9a Ion saturation current profile.

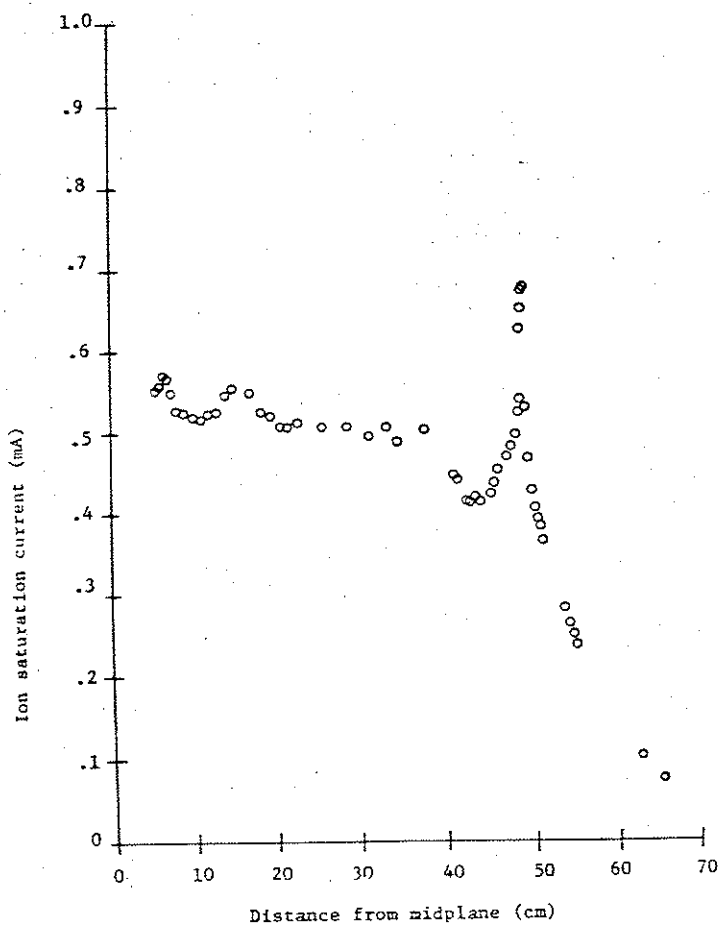

Figure 6.9b Electron saturation current profile.

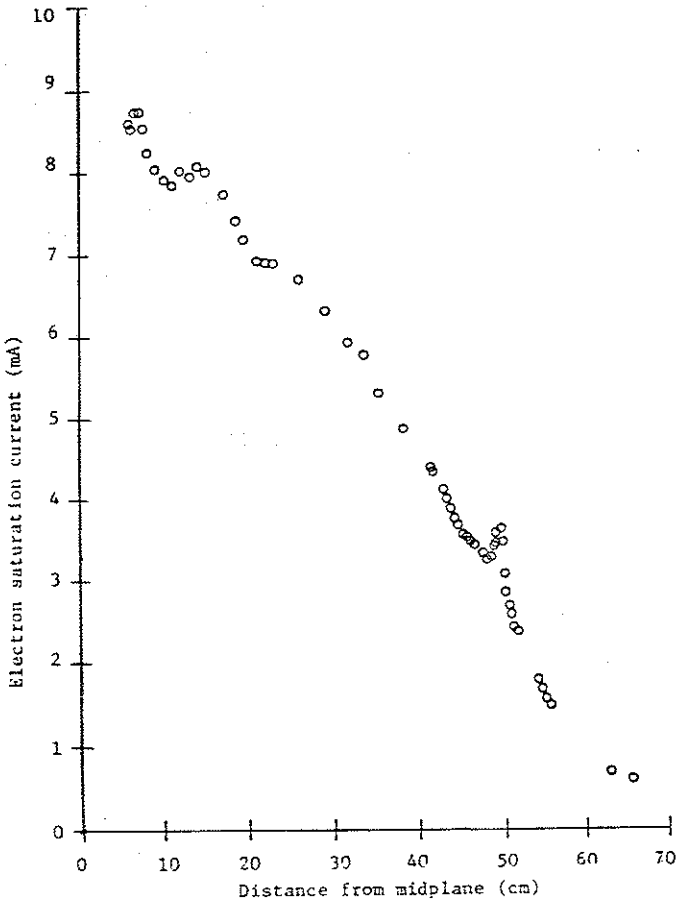

Figure 6.10

Ratio of Electron Saturation Current to Ion Saturation Current vs. Magnetic Field Strength.

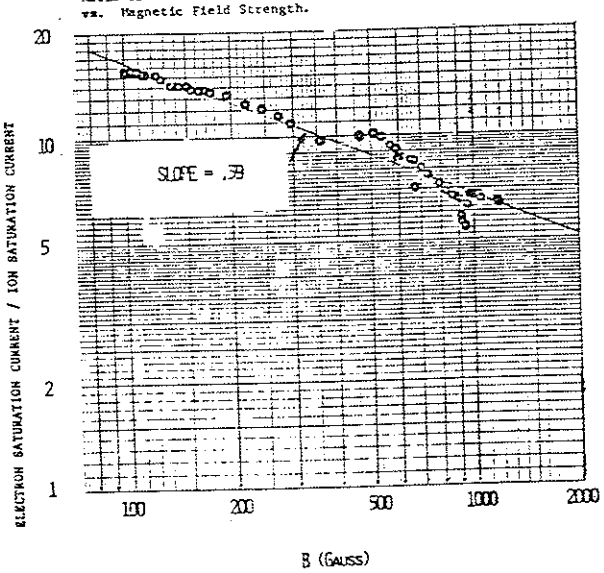

Figure 6.11 Normalized electron saturation current and ion saturation current vs. position.

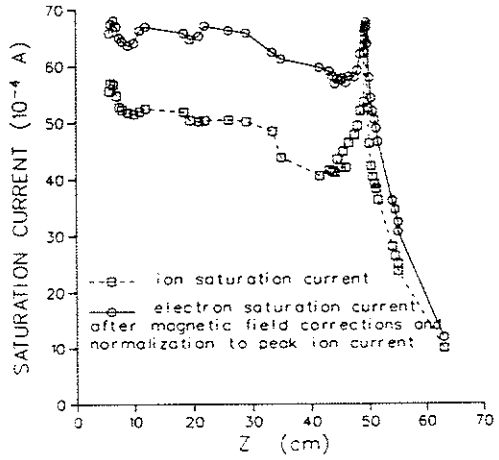

FIGURE 6.12 TWO SURFACE PROBE FOR TURNING POINT STUDY.

FIGURE 6.13 $I_\perp / I_\parallel$ VS. POSITION.

FIGURE 6.14 Typical ion saturation current profiles.

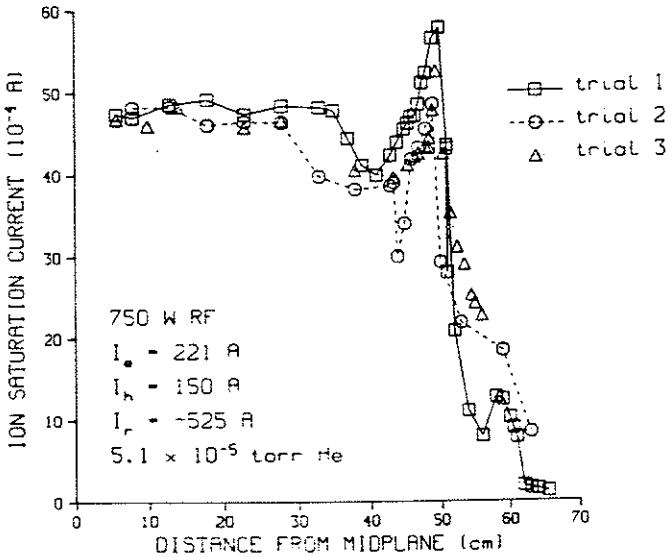

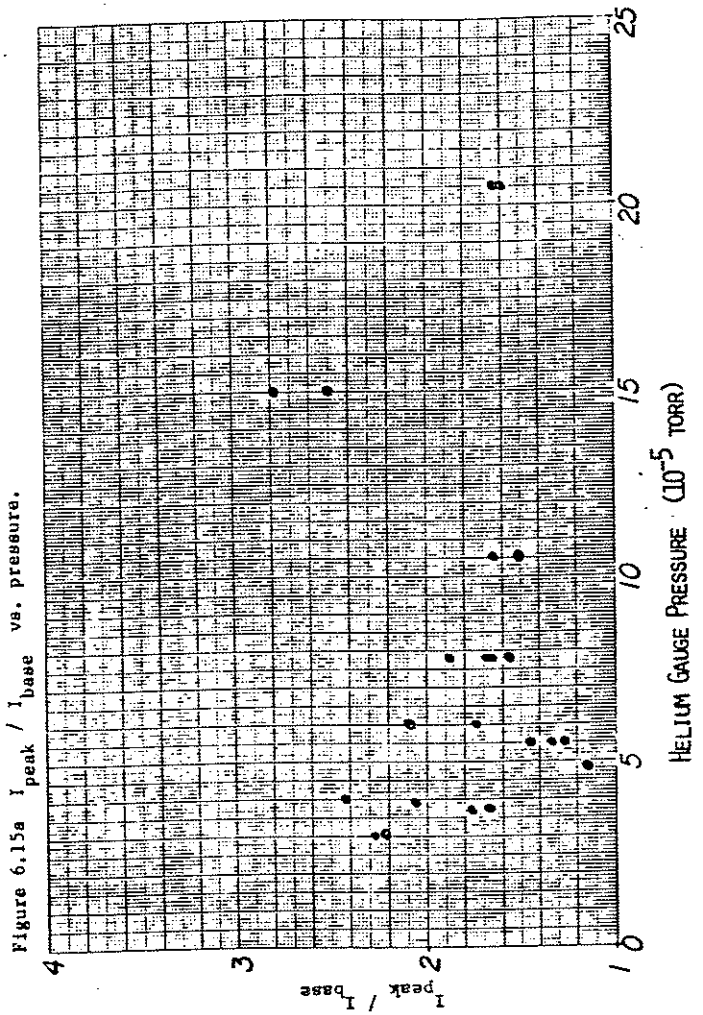

Figure 6.15a I_{peak} / I_{base} vs. pressure.

FIGURE 6.15a FWHM OF ION SATURATION CURRENT PEAK VS. PRESSURE.

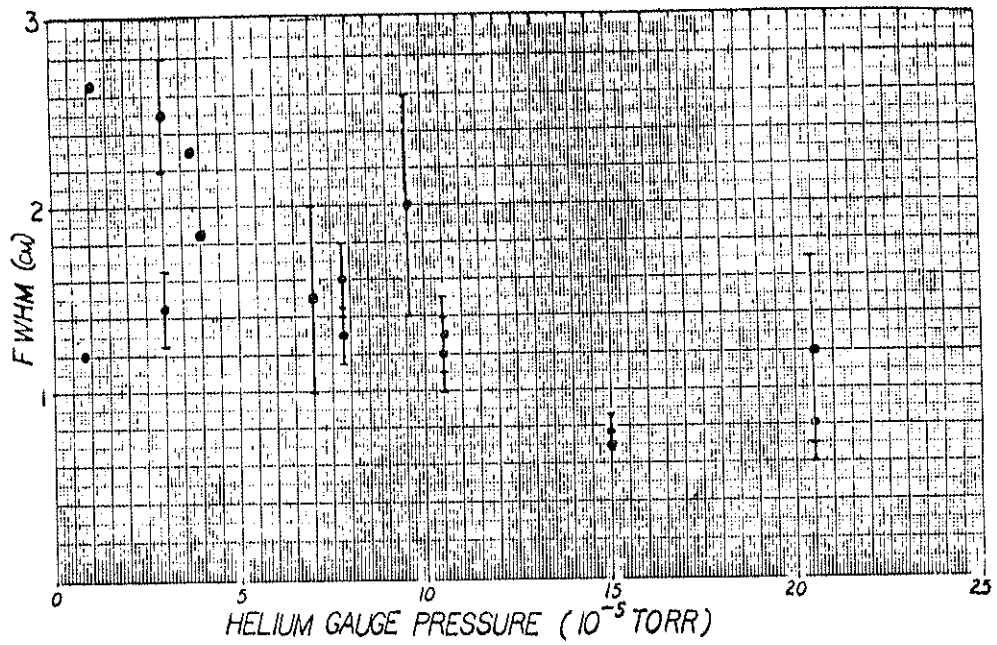

Figure 6.16 ELECTRON TEMPERATURE AT MIDPLANE AND RESONANCE ZONE VS. PRESSURE.

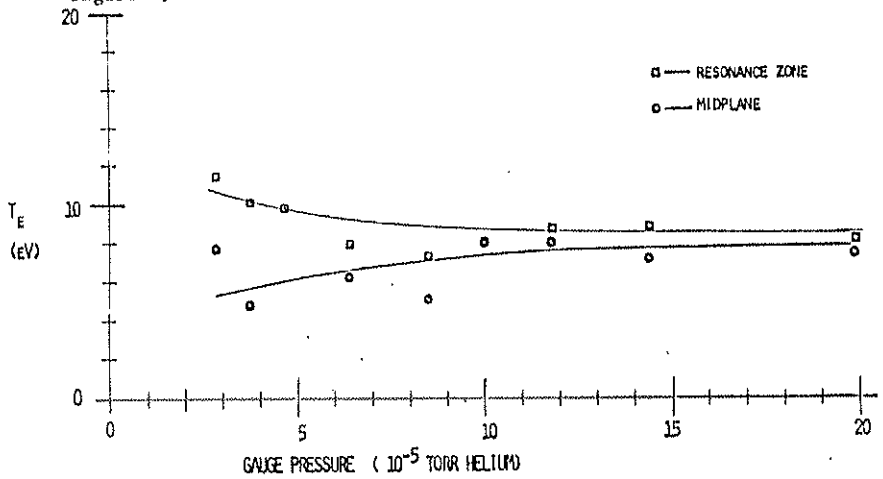

FIGURE 6.17 ΔV_F AT RESONANCE VS. ΔT_E.

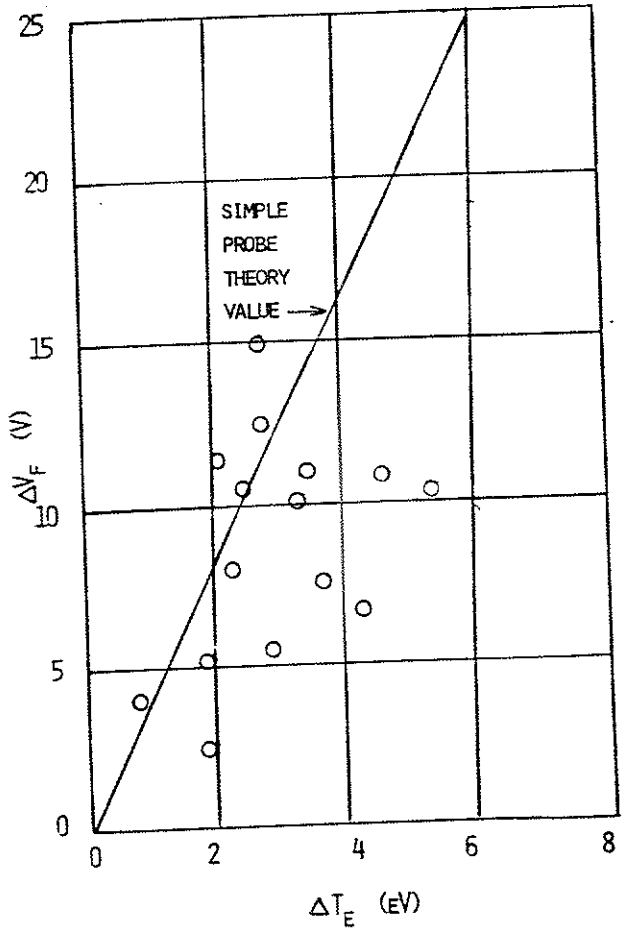

Figure 6.18 Density and temperature profile near resonance.

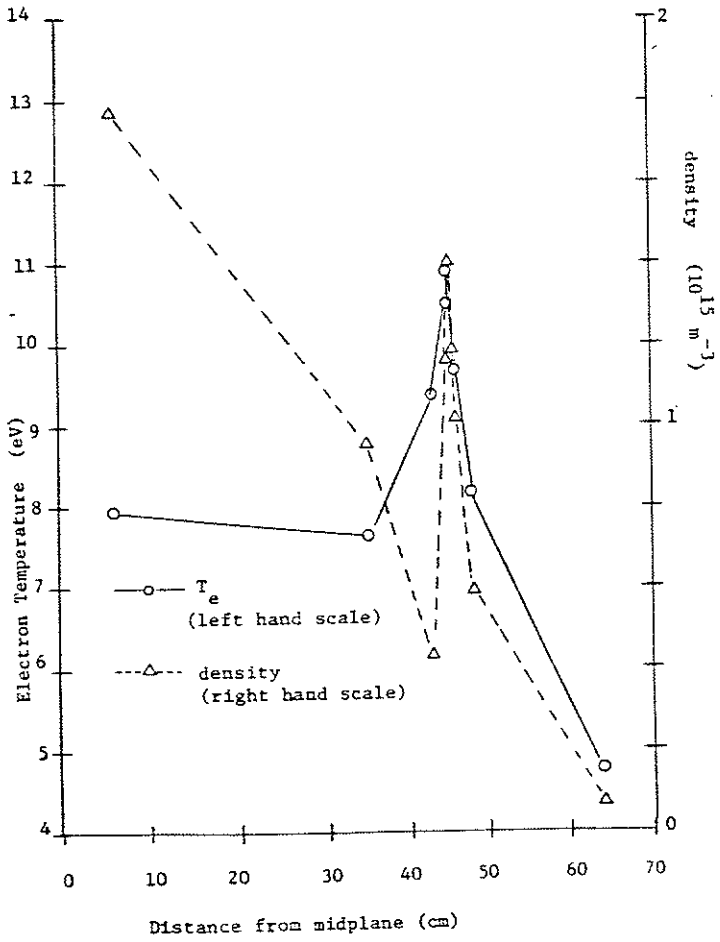

FIGURE 6.19 COMPARISON OF LENGTH SCALES

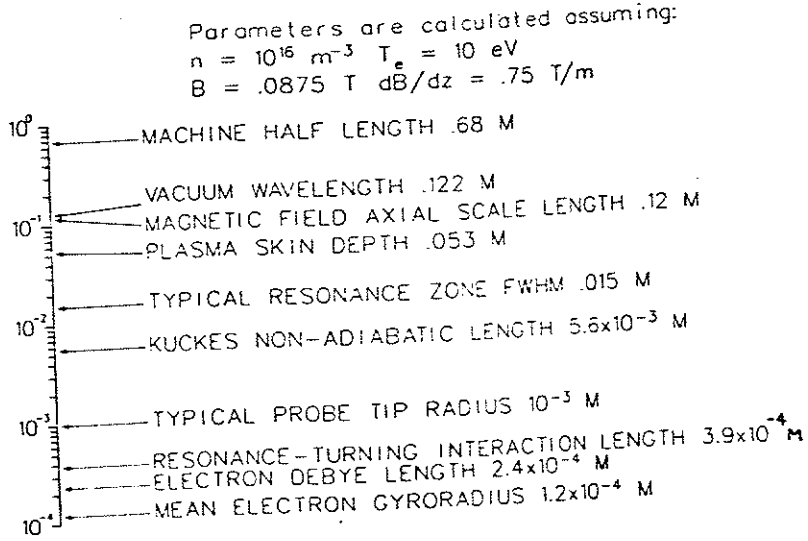

FIGURE 6.20 COMPARISON OF V_P AND V_F PROFILES ACROSS RESONANCE.

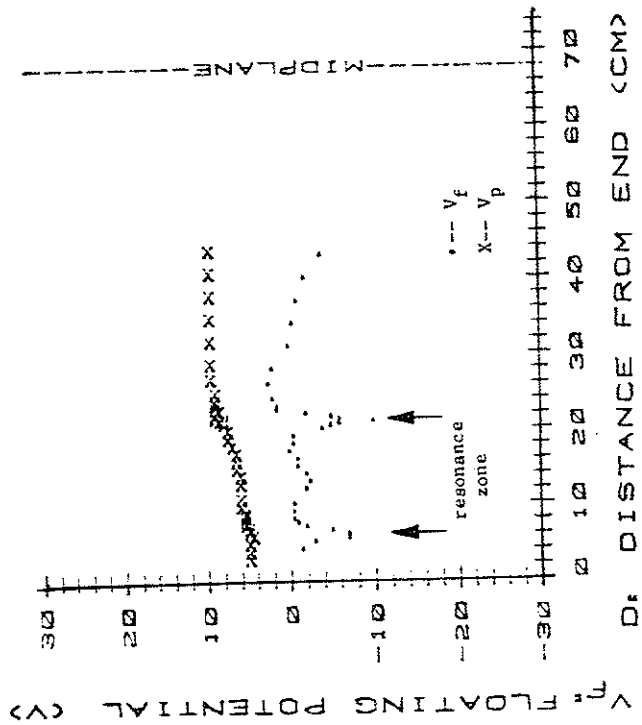

FIGURE 6.21A DENSITY AND POTENTIAL PROFILES FROM THE 4-SPECIES MODEL (SMALL PEAK)

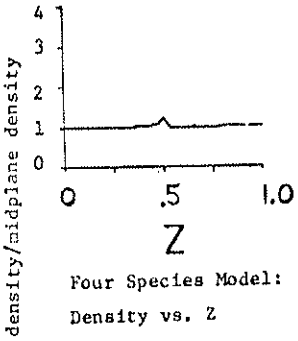

Four Species Model:
Density vs. Z

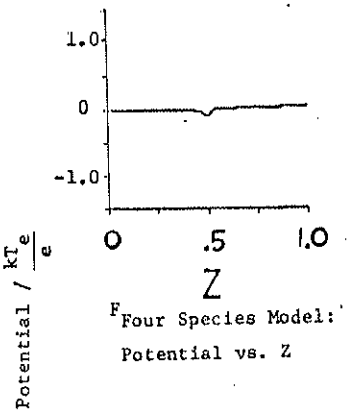

Four Species Model:
Potential vs. Z

FIGURE 6.21B DENSITY AND POTENTIAL PROFILES FROM THE 4-SPECIES CASE (LARGE PEAK)

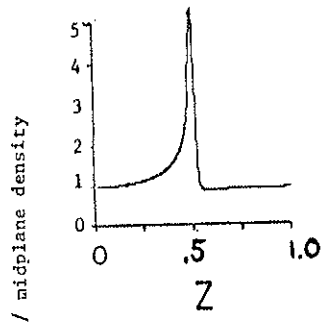

Four Species Model:
Density vs. Z

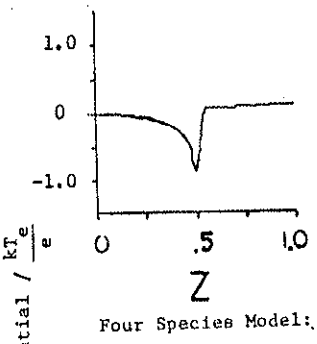

Four Species Model:
Potential vs. Z

FIGURE 6.22 PLASMA POTENTIAL DIP AT RESONANCE ZONE VS. DENSITY PEAK RATIO, FROM THE 4-SPECIES MODEL.

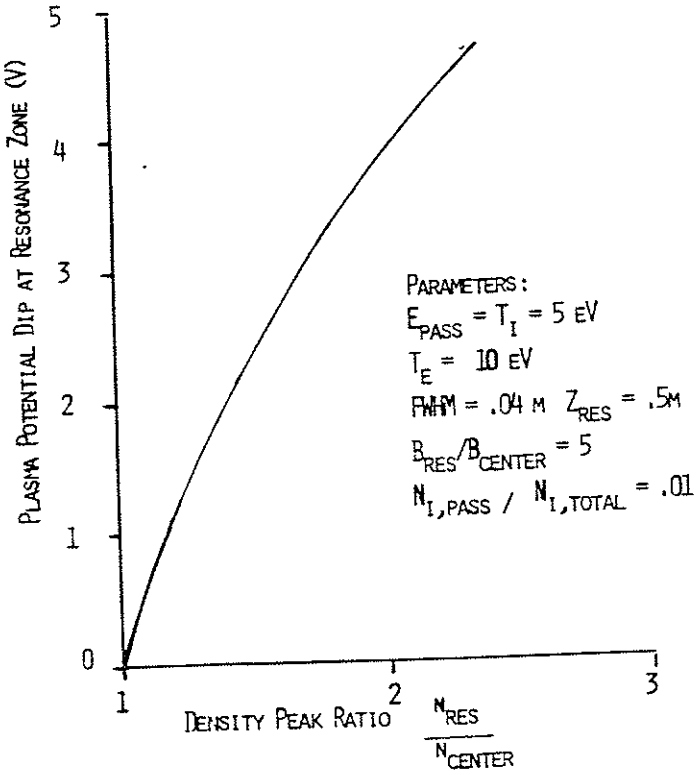

FIGURE 6.23 RELATIVE PLASMA POTENTIAL DIP AT RESONANCE ZONE VS. RELATIVE ION TEMPERATURE, FROM THE 4-SPECIES MODEL

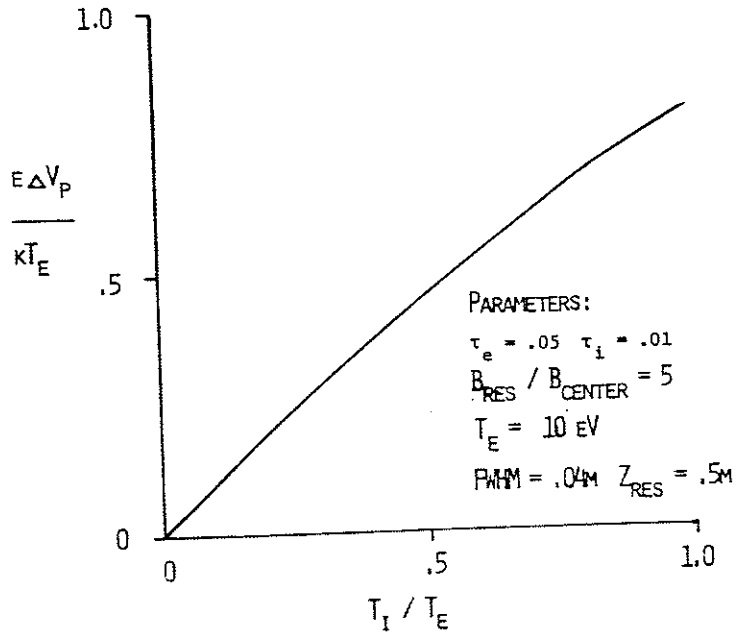

FIGURE 6.24 DEPENDENCE OF RELATIVE DENSITY PEAK AND POTENTIAL DIP ON FRACTION OF RESONANCE-TURNING ELECTRONS.

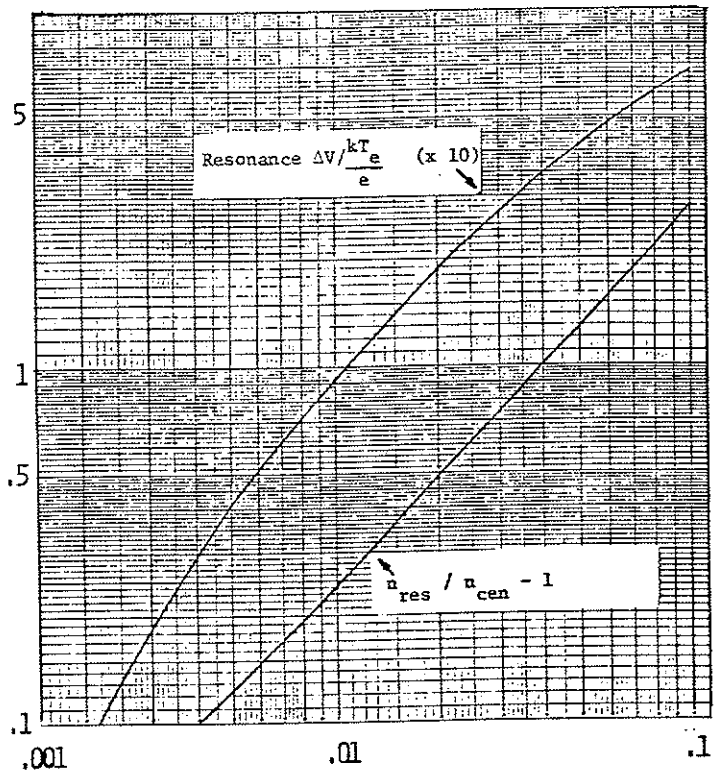

FIGURE 6.25 NORMALIZED V_F DIP VS.

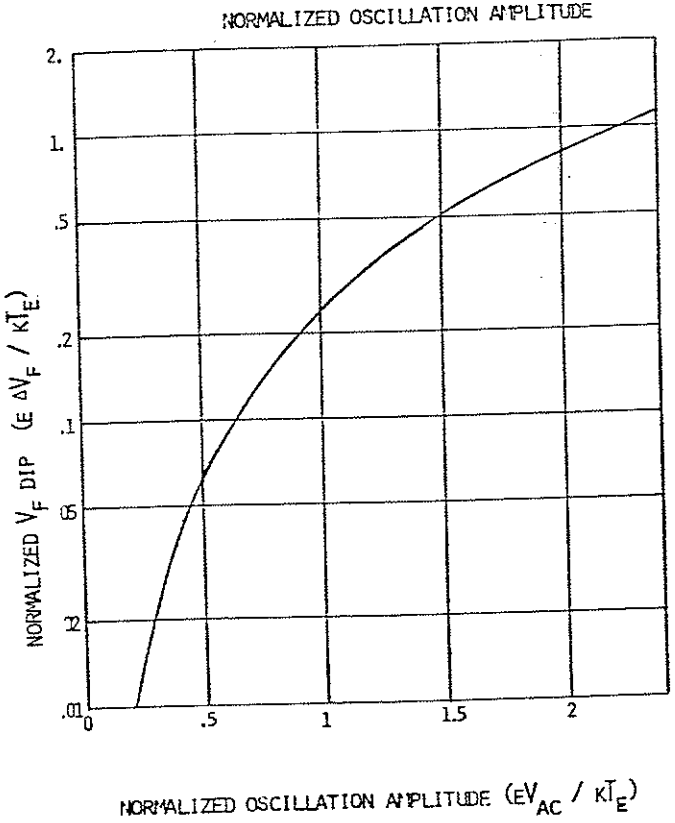

FIGURE 6.26 PROBE-PLASMA CIRCUIT (EQUIVALENT)

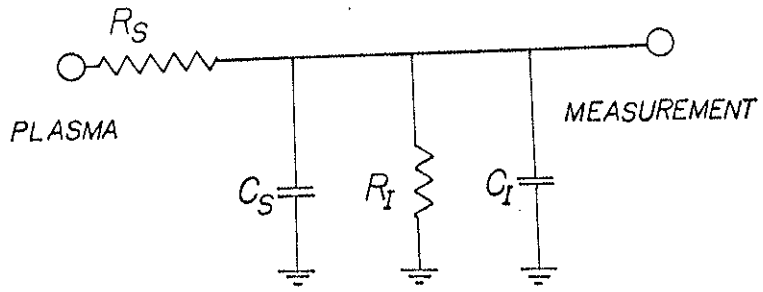

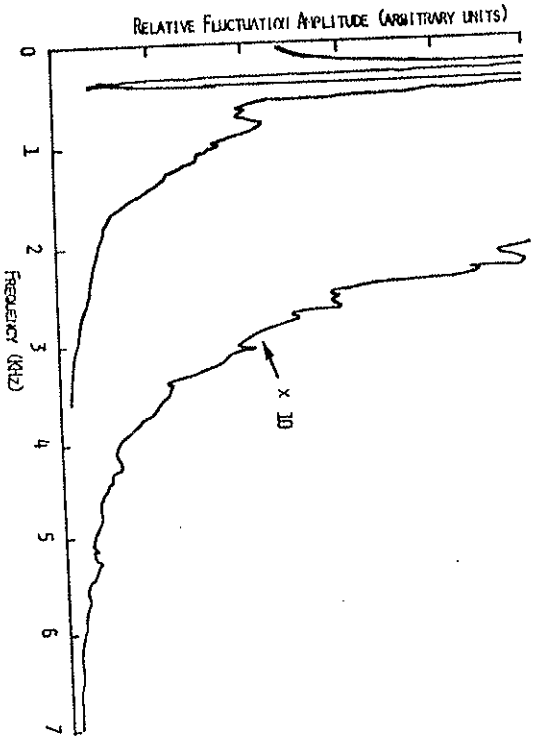

FIGURE 6.27 NOISE SPECTRUM FOR TYPICAL DC MACHINE OPERATION.

REFERENCES AND NOTES FOR CHAPTER 6

[1]Since the ion current normally increases linearly as probe bias becomes more negative, the absolute value of the misnamed "saturation" is somewhat arbitrary. However, by all criteria used--measurement at a fixed, highly negative bias, at a fixed negative bias with respect to V_f, or at the linear-exponential boundary, the result is the same: a resonance peak.

[2]N. R. Whettan in Handbook of Chemistry and Physics, 54th ed., (CRC Press, Cleveland, 1973) p. E214.

[3]M. S. Ioffe, et. al., Sov. Phys.-JETP 40, 1064 (1975).

[4]J. D. Swift and M. J. R. Schwar, Electrical Probes for Plasma Diagnostics, (Iliffe Books: London, 1969).

[5]H. Ikegami, et. al. Nuc. Fusion 13, 351 (1973).

[6]H. Ikegami, S. Aihira and M. Hosokawa, Phys. Fluids 15, 2054 (1972).

[7]H. Ikegami, et. al. Phys. Rev. Lett. 19, 441 (1967).

[8]H. Ikezi, IPPJ-67, Nagoya, Japan (May, 1965).

[9]R. A. Dandl, et. al. Nuc. Fusion 13, 693 (1973); also in Plasma Physics and Controlled Nuclear Fusion Research (Proc. 4th Int. Conf., Madison, Wisconsin, 1971), 2, (IAEA, Vienna, 1971)

[10]V. D. Dougar-Jabon, K. S. Golovanivsky, and V. D. Schepilov, Physica Scripta 18, 506 (1978).

[11]B. I. Patrushev, V. P. Gozak, and D. A. Frank-Kamentskii, Sov. Phys-Tech. Phys. 15, 1058 (1971).

[12]B. W. Clark, et. al. Phys. Fluids 17, 1322 (1974).

[13]B. V. Galaktionov, et. al.,Sov. Phys.-Tech. Phys. 13, 838 (1968).

[14]I. G. Brown, A. Compher and W. Kunkel, Phys. Fluids 14, 1377 (1971).

[15]M. Sugawara and Y. Hatta, J. Phys. Soc. Japan 19, 1908 (1964).

[16]A. Kuckes, Plas. Phys. 10, 367 (1968).

[17]J. C. Sprott and P. H. Edmonds, Phys. Fluids 14, 2703 (1971).

[18]E. Canobbio, Nuc. Fusion 9, 27 (1969).

Chapter 7. Modeling of resonance zone behavior

In this chapter the emphasis is on obtaining the electron distribution function in the presence of ECRH. An adequate description of the observed resonance zone phenomena is possible with relatively simple models of collisions and loss. In the course of the discussion the ECRH rate is derived. The choice of a proper normalization variable representing the relative efficacy of collisions and ECRH in changing electron velocity, is also discussed.

7.1 Simple analytic model of an ECRH mirror plasma

The objective of this section is to find a simple expression for the electron distribution function for a parabolic magnetic mirror with ECRH. The distribution function is determined by both resonance absorption effects and collision effects. To include these effects yet maintain mathematical tractability, the first order approximation used here is to average the Boltzmann equation over a bounce, assuming constant collision frequency ν for all electrons, and constant heating rate $\dot{W}$ for those electrons that have a turning point beyond the resonance zone. Particles whose turning points lie within the resonance zone are assumed not to be heated. The density and "temperature" profile are then obtained from this solution.

One starts with the Boltzmann equation with a Krook type collision term:

$$\frac{\partial f}{\partial t} + v\cdot\nabla_r f + a\cdot\nabla_v f = -\nu(f-f_o) \qquad (7.1.1)$$

In steady state the first term is zero. When averaged over a bounce and over all phase angles,

$$\langle v\cdot\nabla_r f\rangle = \langle v\rangle\cdot\nabla_r f = 0 \quad \text{and}$$

$$\langle a\cdot\nabla_v f\rangle = \langle \dot{v}_\perp\rangle \frac{\partial f}{\partial v_\perp} + \langle \dot{v}_\parallel\rangle \frac{\partial f}{\partial v_\parallel}$$

In the cold plasma limit the heating takes the form of impulsive changes of $v_\perp$ at the resonance zone. If m is the mass of the electron and $\dot{W}$ is the constant heating rate for resonance crossing electrons, then the bounce average of this term is $\langle a\cdot\nabla_v f\rangle = \frac{\dot{W}}{m v_\perp}\frac{\partial f}{\partial v_\perp}$. The bounce average of the RHS is just $\langle -\nu(f-f_o)\rangle = -\nu(f-f_o)$, due to the assumptions of steady state of f and constancy of ν. Here f_o is the equilibrium (Maxwellian) distribution one would expect in the absence of heating:

$$f_o(v_\parallel, v_\perp) = n_R \left(\frac{m}{2\pi kT}\right)^{3/2} \exp\left[-\frac{m}{2kT}(v_\parallel^2 + v_\perp^2)\right] \qquad (7.1.2)$$

In (7.1.2) n_R is the density at the resonance zone, T is the electron temperature, and k is Boltzmann's constant.

With the simplifications just described the Boltzmann equation for the resonance zone distribution function becomes

$$\frac{\partial f}{\partial v_\perp} = P(v_\perp)\, f + Q(v_\perp) \tag{7.1.3}$$

$$\text{with} \quad P(v_\perp) = -\frac{\nu m v_\perp}{\dot{W}} \tag{7.1.4a}$$

$$Q(v_\perp) = n_R \frac{\nu m v_\perp}{\dot{W}} \left(\frac{m}{2\pi kT}\right)^{3/2} \exp\left[-\frac{m}{2kT}(v_\parallel^2 + v_\perp^2)\right] \tag{7.1.4b}$$

The solution for this first order differential equation is

$$f = \exp\left(\int^{v_\perp} P(v_\perp)\, dv_\perp\right) \left[\int Q(v_\perp) \exp\left(-\int^{v_\perp} P(v_\perp')\, dv_\perp\right) dv_\perp + C\right]$$

where C is a function of $v_\parallel$ only. From (7.1.4a) one has

$$\exp\left(\int P(v_\perp)\, dv_\perp\right) = \exp\left(-\frac{\nu m}{\dot{W}} \int v_\perp\, dv_\perp\right)$$

$$= \exp\left(-\frac{\nu m v_\perp^2}{2\dot{W}}\right) = \exp\left(-\frac{\nu kT}{\dot{W}} \frac{m v_\perp^2}{2kT}\right) = \exp\left(-\psi \frac{m v_\perp^2}{2kT}\right).$$

ψ is a dimensionless parameter that indicates the relative effectiveness of collisions as compared with rf heating in changing the velocity distribution function.

Upon integrating the solution integral one obtains

$$f_R(v_\parallel, v_\perp) = C(v_\parallel) \exp\left(-\psi \frac{m v_\perp^2}{2kT}\right) \tag{7.1.5}$$

$$+ \frac{\psi}{\psi - 1} n_R \left(\frac{m}{2\pi kT}\right)^{3/2} \exp\left(-\frac{m v_\parallel^2}{2kT}\right) \left[\exp\left(-\frac{m v_\perp^2}{2kT}\right) - \exp\left(-\psi \frac{m v_\perp^2}{2kT}\right)\right]$$

The condition for proper normalization is that $n_R = \int d^3v\, f_R$. It is found that the integral of the second term of (7.1.5) is n_R, so that C must be zero. The velocity distribution at the resonance zone is therefore

$$f_R(v_\parallel, v_\perp) = \tag{7.1.6}$$

$$\frac{\psi}{\psi - 1} n_R \left(\frac{m}{2\pi kT}\right)^{\frac{3}{2}} \exp\left(-\frac{m v_\parallel^2}{2kT}\right) \left[\exp\left(-\frac{m v_\perp^2}{2kT}\right) - \exp\left(-\psi \frac{m v_\perp^2}{2kT}\right)\right]$$

For positions exterior to the resonance zone, $z > z_R$, the density is found by integrating (7.1.6) over velocity space, with the weighting factors $\frac{B(z)}{B_R}$ and $v_\parallel(z_R)/v_\parallel(z)$, over that portion of resonance zone velocity space in which the turning point satisfies $z_T > z$. The integration is made more convenient by the introduction of the dimensionless variables $x = \frac{m v_\parallel^2}{2kT}$ and $y = \frac{m v_\perp^2}{2kT}$. Then the expression for density for $z > z_R$ becomes

$$n(z) =$$

$$\frac{B(z)}{B_R} \frac{\psi}{\psi - 1} \frac{n_R}{\sqrt{\pi}} \int_0^\infty dy\, (e^{-y} - e^{-\psi y}) \int_{\left(\frac{B}{B_R} - 1\right)y}^\infty dx\, e^{-x} \left(x - \left(\frac{B}{B_R} - 1\right)y\right)^{-1/2}$$

$$= \frac{B}{B_R}\frac{\psi}{\psi-1} n_R \int_0^\infty dy\ (\exp(-\frac{B}{B_R}y) - \exp((1-\psi-\frac{B}{B_R})y)$$

$$= n_R \frac{\psi}{\psi + \frac{B}{B_R} - 1} \qquad (7.1.7)$$

Note that for $\psi >> 1$ the density approaches n_R. This is what one would expect in a collision dominated plasma. The distribution function is then virtually a Maxwellian, which in a lossless mirror has constant density. Note that if the magnetic field intensity continues to increase beyond the resonance zone, the value of magnetic field B_H for which the density declines to half of its resonance zone value is given by

$$B_H = B_R(\psi + 1) \qquad (7.1.8)$$

For $z < z_R$ the contributions of both (7.1.6) and the non-resonance passing particles must be considered. The contribution to density of (7.1.6) can be written in terms of dimensionless variables x and y as

$$n_I(z) = \frac{B}{B_R} n_R \frac{\psi}{\psi-1}\frac{1}{\sqrt{\pi}}\int_0^\infty dy\ [e^{-y} - e^{-\psi y}] \int_0^\infty dx\ e^{-x}\ (x+(\frac{B}{B_R}-1)y)^{-1/2}$$

$$= n_R \frac{B}{B_R}\frac{\psi}{\psi-1}\{\int_0^\infty dy\ \exp(-\frac{B}{B_R}y) - \int_0^\infty dy\ \exp((1-\frac{B}{B_R}-\psi)y)$$

$$-\int_0^\infty dy\ \exp(-\frac{B}{B_R}y)\ \mathrm{erf}([(1-\frac{B}{B_R})y]^{1/2})$$

$$+\int_0^\infty dy\ \exp((1-\frac{B}{B_R}-\psi)y)\ \mathrm{erf}([(1-\frac{B}{B_R})y]^{1/2})\} \qquad (7.1.9)$$

Applying the integrals from appendix A, one has

$$n_I(z) = n_R \frac{\psi}{\psi-1}\{1 - (1-\frac{B}{B_R})\frac{1}{2} - \frac{1}{\psi + \frac{B_R}{B} - 1}\ (1 - [\frac{1-\frac{B}{B_R}}{\psi}]^{1/2}\ )\} \qquad (7.1.10)$$

In this model particles are divided into two classes; those that cross resonance (class I); and those that do not (class II). Those particles which do not pass resonance are assumed not to be heated and their distribution function is taken to be a Maxwellian. In the absence of electrostatic potential effects, the density of such particles is given by the familiar "loss cone" formula:

$$n_{II}(z) = n_{io}\ (1-\frac{B}{B_R})^{1/2} \qquad (7.1.11)$$

In (7.1.11) n_{io} is the density of non-resonance passing particles at the midplane. In the absence of heating the "resonance zone" is non-existent. It can be dealt with by setting $B_R = \infty$. In this case one sees that $n_{io} = n_o$, the total midplane density. When heating is applied to a plasma which is initially Maxwellian, the distribution changes <u>only</u> in those regions with turning points $z_T > z_R$. Thus one is justified in retaining the identification $n_{io} = n_o$. The density for $z < z_R$ is then given by

$$n(z) = n_I(z) + n_{II}(z) = \tag{7.1.12}$$

$$n_o \sqrt{1-\frac{B}{B_R}} + n_R \frac{\psi}{\psi-1}\{1-[1-\frac{B}{B_R}]^{1/2} - \frac{1}{1+\frac{B_R}{B}(\psi-1)}(1-[\frac{1-\frac{B}{B_R}}{\psi}])^{1/2})\}$$

The requirement that the contribution of both terms gives a density of n_o at the midplane means that

$$n_R = n_o \frac{\psi-1}{\psi}\{1 - \frac{1}{1+r(\psi-1)} \frac{1-[\frac{(1-\frac{1}{r})}{\psi}]^{1/2}}{1-[1-\frac{1}{r}]^{1/2}}\}^{-1} \tag{7.1.13}$$

where r is the ratio of the resonance magnetic field to the midplane field. In terms of the central density one has, for $z < z_R$,

$$n(z) = n_o \{(1-\frac{B}{B_R})^{1/2} + (1-(1-\frac{B}{B_R})^{1/2} - \frac{1}{1+\frac{B_R}{B}(\psi-1)}(1-[\frac{1-\frac{B}{B_R}}{\psi}])^{1/2})$$

$$[1-\frac{1}{1+r(\psi-1)} \frac{1-\sqrt{(\frac{r-1}{\psi r})}}{1-\sqrt{\frac{r-1}{r}}}]^{-1}\} \tag{7.1.14}$$

Figure 7.1 shows density as a function of magnetic field value for this mode. The essential feature is a peak at the resonance position whose width and height depend strongly on ψ. Figure 7.2a shows the dependence of $\frac{n_R}{n_o}$ vs. ψ. Figure 7.2b shows the dependence of the full width at half maximum (FWHM) in magnetic field units, normalized to the resonance field B_R.

It turns out that there is a very simple relation, in this model, between FWHM, ψ, and the peak height:

$$\frac{FWHM}{B_R} = .58\ \psi\ (\frac{n_R}{n_o} - 1) \tag{7.1.15}$$

This is an approximation but it is a very good one, as shown in figure 7.3 for various ψ values.

The altered distribution function will also change the collection characteristics of probes. The new parallel electron flux at the plasma potential can be found by integrating $v_\parallel$ over the new distribution function. For $z < z_R$ one finds

$$\Gamma_\parallel = n_o (\frac{kT}{2\pi m})^{\frac{1}{2}}\{1 - \frac{B}{B_R} + \frac{B}{B_R}\frac{\psi-1}{\psi}\{1 - \frac{1}{1+r(\psi-1)} \frac{1-\sqrt{\frac{r-1}{\psi r}}}{1-\sqrt{\frac{r-1}{r}}}\}^{-1}\} \tag{7.1.16}$$

For $z > z_R$: $\Gamma_\parallel = n_R (\frac{kT}{2\pi m})^{\frac{1}{2}} \frac{\psi}{\frac{B}{B_R}+\psi-1}$

$$= n_o (\frac{kT}{2\pi m})^{\frac{1}{2}}\{1 - \frac{1}{1+r(\psi-1)} \frac{1-\sqrt{\frac{r-1}{\psi r}}}{1-\sqrt{\frac{r-1}{r}}}\}^{-1} \frac{\psi-1}{\frac{B}{B_R}+\psi-1} \tag{7.1.17}$$

For a probe at the resonance zone biased at V volts in a plasma whose potential is V_p, one finds for the parallel flux

$$\Gamma_{R\parallel}(V) = n_R (\frac{kT}{2\pi m})^{\frac{1}{2}} \exp(\frac{e(V-V_p)}{kT}) \tag{7.1.18}$$

This is the same as for a Maxwellian plasma of density n_R, which is consistent with the assumption of this model that heating does not change the parallel velocity at resonance. However, for a plane whose surface is tangent to the magnetic field, the perpendicular flux is

$$\Gamma_{R\perp}(V) = \frac{\psi}{\psi-1} n_R \left(\frac{kT}{2\pi m}\right)^{\frac{1}{2}} \left[\exp\left(\frac{e(V-V_p)}{kT}\right) - \psi^{-3/2} \exp\left(-\psi \frac{e(V-V_p)}{kT}\right)\right] \quad (\psi \neq 1) \qquad (7.1.19a)$$

$$= n_R \left(\frac{kT}{2\pi m}\right)^{\frac{1}{2}} \left(\frac{3}{2} - \frac{e(V-V_p)}{kT}\right) \exp\left(\frac{e(V-V_p)}{kT}\right) \quad (\psi = 1) \qquad (7.1.19b)$$

For perpendicular flux the effect of the heated distribution is not only to increase the total perpendicular current, but to reduce the rate of fall off with negative bias. The altered probe response for $I_{e\perp}$ is shown in figure 7.4 A real probe will generally collect a substantial parallel flux, for which the current characteristics remain Maxwellian. The probe response is thus a mixture of a normal Maxwellian response and a perturbed ECRH response. Use of simple probe theory at resonance is liable to yield ambiguous results without this consideration.

7.2 Numerical simulation of an ECRH plasma density profile

In the previous section a simple analytical model for the density along the axis of an ECRH mirror was found. The two assumptions responsible for the great simplicity of the model—constancy of collision rate and heating rate throughout velocity space—are not realistic. One would like a second look in which these assumptions are relaxed, to see if the basic resonance features persist.

To meet this need, Fortran programs were written, incorporating somewhat different approximations to ionization, scattering, and loss. They have the following features in common:

(1) The velocity space is divided into an NxN grid, 30^2 in early models, 60^2 in latter ones. The bins extended up to 3 $v_{th} \equiv 3 \times (2kT_e/e)^{1/2}$ in both $v_\perp$ and $v_\parallel$. Well over 99% of Maxwellian-weighted velocity space is represented here. The ij-th bin is centered at parallel speed $v_\parallel = v_i = (i - \frac{1}{2})\, v_{th}$ and perpendicular speed $v_\perp = v_j = (j - \frac{1}{2})\, v_{th}$.

(2) The effect of heating on particles on the center of each bin is considered to determine the relative probability of scattering into adjacent bins. For this purpose "heating" may result in a lower $v_\perp$, depending on the relative gyrophase angle at resonance, so that the velocity space diffusion due to ECRH is accounted for. The earlier model neglected this. Furthermore a more realistic model, that of Sprott and Edmonds[2], and Kawamura and Terashima[8] is used for the mean heating rate, truncated at the maximum possible

$v_\perp$ change, that of resonance turning particles. This model assumes that the change in $W_\perp$ during a single resonance passage is governed by the constant parallel speed model of Kuckes[1], adjusted for the actual speed of the particle at resonance and integrated over the distribution of speeds.

(3) For each bin of velocity space, a collision rate ν_{ij} is found appropriate to the center of the bin. Collisions of electrons with ions, other electrons, and neutrals summed to find ν_{ij}.

$$\nu_e = \nu_{en} + \nu_{ei} + \nu_{ee} \qquad (7.2.1)$$

Within the ij-th bin, the effect of collisions is assumed to be an exponential relaxation of the local distribution function value f_{ij} the Maxwellian value $f_{Max,ij}$ at rate ν_e.

$$f_{ij}(t + \Delta t) = f_{Max,ij} + (f_{ij}(t) - f_{Max,ij})\exp(-\nu_e \Delta t) \qquad (7.2.2)$$

where Δt is the time step during which the distribution function value f_{ij} is to be iterated.

(4) The time step Δt is chosen so that the relative changes due to collisions or heating during Δt, are small. Then time is iterated and the transfers between bins due to heating, and collisional relaxation of the perturbed distribution is applied until the worst relative bin change during an iteration is < 1%.

(5) The parabolic approximation to the magnetic field is retained.

(6) Electrostatic fields are neglected.

(7) As a result of points (5) and (6), all electrons in the system

transit through the midplane. So if the midplane distribution function is found, the distribution function is known everywhere. This is integrated numerically (simply a weighted summation of f_{ij} lues in this model) to find the density n(z), parallel particle flux $\Gamma(z)$, mean parallel energy $W_\parallel$, and mean perpendicular energy $W_\perp$. These are evaluated at several points along the axis to get a good idea of their spatial dependence. The values of mean collision rate, mean heating rate, resonance peak and resonance width are also found. In some later versions resolution of variables in the resonance zone region was improved by taking the velocity space at the resonance zone, not the midplane. Appendix E gives further details. Figure 7.6 shows a diagram of contours in velocity space for a resonance mirror ratio of 5, and a ξ value of .755. Figures 7.7, 7.8, 7.9, and 7.10 show the values of density, mean perpendicular energy, mean parallel energy, and parallel particle flux for this case, respectively.

The mean heating rate for the derived distribution function is increased considerably over a Maxwellian, as shown in Figure 7.11 as a function of tank pressure. In this model, as in the model of section 7.1, the half-width increases with fill pressure, shown in figure 7.12. Figure 7.13 shows the dependence of density peak ratio on system pressure as the normalized rf-electric field is kept constant. A summary of the results of this program, DISREX, for various neutral pressures is given in table 7.2.

7.3 KKP distributions.

In section 7.1 the resonance zone distribution function was found under the assumptions of constant heating rate and constant collision frequency. This was useful in order to obtain explicit, relatively simple expressions for the distribution function $f(v_\parallel, v_\perp)$ and derived density $n(z)$. In section 7.2 a procedure was described to obtain a realistic distribution function, but it is a purely numerical process, so that the numbers coming out of the computer do not always make it clear what the dominant physics of the situation is. It is desirable to treat heating and collisions realistically, while not entirely deserting the analytical process. The distributions of this section are an attempt to bridge the gap between the ultra simple model of 7.1 and the powerful but cumbersome numerical model of 7.2.

These will be denoted as KKP distributions. The acronym is short for "Kuckes heating, Krook relaxation with a Power law dependence of collision rate on velocity."

The heating rate for particles passing through the resonance zone with constant parallel speed $v_\parallel$ has been derived by Kuckes[1], Sprott and Edmonds[2], and Eldridge[3]. At each resonance zone transit the perpendicular energy gain, averaged over phase angles, is

$$\overline{\Delta W_\perp} = \frac{\pi e E^2}{4 B_r' v_\parallel} \tag{7.3.1}$$

E is the magnitude of the perpendicular component of the oscillating electric field, and B′ is the absolute value of the gradient of the magnetic field along the field lines, both evaluated at resonance.

In the parabolic mirror the frequency of resonance transits for an electron of resonance perpendicular speed $v_\perp$ is

$$F_t = \frac{2}{\pi} v_\perp \left(\frac{\beta}{r}\right)^{\frac{1}{2}} \tag{7.3.2}$$

The mean heating rate per particle is then

$$\overline{\dot{W}_\perp} = F_t \overline{\Delta W_\perp} = \frac{e E^2}{2 B_r'} \frac{v_\perp}{v_\parallel} \left(\frac{\beta}{r}\right)^{\frac{1}{2}} \tag{7.3.3}$$

In terms of the midplane magnetic field B_o and turning point mirror ratio R_t, (7.3.3) is equivalent to

$$\overline{\dot{W}_\perp} = \frac{eE^2}{4B_o} (r-1)^{-1/2} (R_t - r)^{-1/2} \tag{7.3.4}$$

The effective perpendicular acceleration is then

$$\dot{v}_\perp = \frac{\overline{\dot{W}_\perp}}{m v_\perp} = \left[\frac{e E^2}{2mB'Z_r} \left(\frac{r-1}{r}\right)^{1/2}\right] / v_\parallel \equiv \frac{\kappa}{v_\parallel} \tag{7.3.5}$$

The variable κ depends only on the fields and device geometry, not on electron velocity. Z_r is the distance between midplane and resonance zone.

The collision term in the Boltzmann equation is represented by a Krook-type relaxation to a Maxwellian distribution f_M at the local velocity space rate

$$\left.\frac{\delta f}{\delta t}\right|_{col} = -\nu(\vec{v})\,(f(\vec{v}) - f_M(\vec{v})) \tag{7.3.6}$$

where $\nu(\vec{v}) = \Pi\, v^s$ (7.3.7)

Π is a normalizing constant and $v = (v_\perp^2 + v_\parallel^2)^{1/2}$.

These assumptions lead to a class of electron velocity distribution functions which, in the region of velocity space designated as I in figure 7.5 solutions to the equation

$$\frac{\kappa}{v_\parallel}\frac{\partial f}{\partial v_\perp} = -\Pi\,(v_\perp^2 + v_\parallel^2)^{\frac{s}{2}}\,(f - f_M) \tag{7.3.8}$$

Or, $$\frac{\partial f}{\partial v_\perp} = Pf + Q \tag{7.3.9}$$

where $P \equiv -\frac{\Pi}{\kappa}\,(v_\perp^2 + v_\parallel^2)^{\frac{s}{2}}\,v_\parallel$ (7.3.10a)

and $Q \equiv \frac{\Pi}{\kappa}\,(v_\perp^2 + v_\parallel^2)^{\frac{s}{2}}\,v_\parallel\, n_r\,(\frac{m}{2\pi kT})^{\frac{3}{2}}\exp[-\frac{m}{2kT}(v_\perp^2 + v_\parallel^2)]$ (7.3.10b)

The solution of $f(v_\parallel, v_\perp)$ is given by

$$f = \exp[\int_0^{v_\perp} P\,dv_\perp]\,\{\int_0^{v_\perp} Q\exp[-\int_0^{v_\perp} P\,dv_\perp] + C\} \tag{7.3.11}$$

The constant of integration C is chosen so that the Maxwellian limit is obtained in the limit $v_\perp \to 0$ and $\kappa \to 0$:

$$C = n_r\,(\frac{m}{2\pi kT})^{3/2}\exp[-\frac{mv_\parallel^2}{2kT}] \tag{7.3.12}$$

Within the trapped region of resonance zone velocity space the KKP distribution of type s is given by

$$f = n_r\,(\frac{m}{2\pi kT})^{3/2}\exp[-\frac{mv_\parallel^2}{2kT} - \frac{\Pi}{\kappa}v_\parallel\int_0^{v_\perp}(v_\parallel^2 + v_\perp^2)^{\frac{s}{2}}\,dv_\perp] \times \tag{7.3.13}$$

$$\{1 + \frac{\Pi}{\kappa}v_\parallel\int_0^{v_\perp}(v_\parallel^2+v_\perp^2)^{\frac{s}{2}}\exp[-\frac{mv_\perp^2}{2kT} + \frac{\Pi}{\kappa}v_\parallel\int_0^{v_\perp}(v_\parallel^2 + v_\perp^2)^{\frac{s}{2}}\,dv_\perp]\,dv_\perp\}$$

The simplest case is that of $s = 0$; a collision rate independent of velocity. This is the same assumption used in the resistive dielectric heating model[4].

For the Kuckes-type[1] heating one finds that

$$f = n_r\,(\frac{m}{2\pi kT})^{3/2}\exp[-\frac{mv_\parallel^2}{2kT}]\exp[-\frac{\nu}{\kappa}v_\parallel v_\perp] \times$$

$$\{1 + \frac{\nu}{\kappa}v_\parallel(\frac{\pi kT}{2m})^{\frac{1}{2}}\exp[\frac{kT}{2m}\frac{\nu^2}{\kappa^2}v_\parallel^2] \times \tag{7.3.14}$$

$$\{\mathrm{erf}((\frac{kT}{2m})^{\frac{1}{2}}\frac{\nu}{\kappa}v_\parallel) - \mathrm{erf}((\frac{kT}{2m})^{\frac{1}{2}}\frac{\nu}{\kappa}v_\parallel - (\frac{m}{2kT})^{\frac{1}{2}}v_\perp)]\}$$

Another case of interest is that of $s = 1$. This corresponds to a constant collision cross section, which is the limiting case for low energy electrons in a neutral-dominated plasma where $\nu \sim \nu_{en}$. In this case (7.3.13) reduces to

$$f = n_r \left(\frac{m}{2\pi kT}\right)^{3/2} \exp\left[-\frac{mv_\parallel^2}{2kT} - \frac{\Pi}{2\kappa} v_\parallel v_\perp v\right] \left(\frac{v_\perp + v}{v_\parallel}\right)^{-\frac{\Pi v_\parallel^3}{2\kappa}} \times$$

$$\left\{1 + \frac{\Pi}{\kappa} v_\parallel \int_0^{v_\perp} dv_\perp \, v \exp\left[-\frac{mv_\perp^2}{2kT} + \frac{\Pi}{2\kappa} v_\parallel v_\perp v\right] \left(\frac{v_\perp + v}{v_\parallel}\right)^{\frac{\Pi v_\parallel^3}{2\kappa}}\right\} \qquad (7.3.15)$$

For Coulomb scattering, $\nu \sim v^{-3}$. Then (7.3.13) becomes

$$f = n_r \left(\frac{m}{2\pi kT}\right)^{3/2} \exp\left[-\frac{mv_\parallel^2}{2kT} - \frac{\Pi v_\perp}{\kappa v_\parallel v}\right] \times$$

$$\left\{1 + \frac{\Pi}{\kappa} v_\parallel \int_0^{v_\perp} dv_\perp \, v^{-3} \exp\left[-\frac{mv_\perp^2}{2kT} + \frac{\Pi v_\perp}{\kappa v_\parallel v}\right]\right\} \qquad (7.3.16)$$

The loss region in velocity space will be approximated with the idealized "hybrid simplex" form described in chapter 4. The regions where different computational procedures must be used are labelled in figure 7.5 as I, II, and III. This is appropriate for a mirror with all the electrostatic potential drop ϕ at the wall. Particles are confined magnetically if they turn before the maximum field position L, $v_\parallel < \left(\frac{B_L}{B_R} - 1\right)^{1/2} v_\perp$, and electrostatically if $v_\parallel < \left(\frac{2e\phi}{m}\right)^{1/2}$.

Within the region II of figure 7.5 the Boltzmann-Krook equation has an additional term representing outflux of particles,

$$\frac{\kappa}{v_\parallel} \frac{\partial f}{\partial v_\perp} = -\Pi \left(v_\perp^2 + v_\parallel^2\right)^{\frac{s}{2}} (f - f_M) - \frac{f}{\tau_\ell} \qquad (7.3.17)$$

where τ_ℓ is the effective loss time. In a parabolic mirror without internal electrostatic fields, taking into account the fact that the exit time is different for positive and negative $v_\parallel$,

$$\tau_\ell = \frac{\left(\sin^{-1}\left[\frac{(r-1)\left(\frac{L}{Z_R}\right)^2}{r\left(\frac{v_\parallel}{v_\perp}\right)^2 - 1}\right]^{1/2}\right)^2 - \left(\sin^{-1}\left[\frac{r-1}{r\left(\frac{v_\parallel}{v_\perp}\right)^2 - 1}\right]^{1/2}\right)^2}{v_\perp \left(\frac{\beta}{r}\right)^{1/2} \sin^{-1}\left[\frac{(r-1)\left(\frac{L}{Z_R}\right)^2}{r\left(\frac{v_\parallel}{v_\perp}\right)^2 - 1}\right]^{1/2}} \qquad (7.3.18)$$

For mathematical tractability the limiting form will be used:

$$\lim_{v_\perp \to 0} \tau_\ell = \frac{L^2 - Z_r^2}{v_\parallel L} \equiv \frac{1}{\alpha v_\parallel} \qquad (7.3.19)$$

If the LHS heating term of (7.3.17) is set to zero, then in region II,

$$f = \frac{1}{1 + \frac{1}{\nu(\vec{v})\tau_\ell}} f_M \qquad (7.3.20)$$

The new constant of integration C for region II is then

$$C = \frac{1}{1 + \frac{\Pi}{\alpha} v_\parallel^{s-1}} n_r \left(\frac{m}{2\pi kT}\right)^{3/2} \exp\left[-\frac{mv_\parallel^2}{2kT}\right] \qquad (7.3.21)$$

With these considerations the expressions for the loss region II distribution functions are,

$$f = n_r \left(\frac{m}{2\pi kT}\right)^{3/2} \exp\left[-\frac{mv_\parallel^2}{2kT} - \frac{\nu v_\parallel v_\perp}{\kappa} - \alpha v_\parallel v_\perp\right] \times \qquad (s = 0)$$

$$\left\{\frac{1}{1 + \frac{\alpha}{\nu} v_\parallel} + \frac{\nu}{\kappa} v_\parallel \int_0^{v_\perp} dv_\perp \exp\left[-\frac{mv_\perp^2}{2kT} + \frac{\nu v_\parallel v_\perp}{\kappa} + \alpha v_\parallel v_\perp\right]\right\} \qquad (7.3.22)$$

$$f = n_r \left(\frac{m}{2\pi kT}\right)^{3/2} \exp\left[-\frac{mv_\parallel^2}{2kT} - \frac{\Pi v_\perp}{\kappa v_\parallel v} - \alpha v_\parallel v_\perp\right] \left(\frac{v_\perp + v}{v_\parallel}\right)^{-\frac{\Pi v_\parallel^3}{2\kappa}} \times \qquad (s = 1)$$

$$\left\{\frac{1}{1 + \frac{\alpha}{\Pi}} + \frac{\Pi}{\kappa} v_\parallel \int_0^{v_\perp} dv_\perp \, v \exp\left[-\frac{mv_\perp^2}{2kT} + \frac{\Pi v_\perp}{\kappa v_\parallel v} + \alpha v_\parallel v_\perp\right] \left(\frac{v_\perp + v}{v_\parallel}\right)^{\frac{\Pi v_\parallel^3}{2\kappa}}\right\} \qquad (7.3.23)$$

$$f = n_r \left(\frac{m}{2\pi kT}\right)^{3/2} \exp\left[-\frac{mv_\parallel^2}{2kT} - \frac{\Pi}{2\kappa} v_\parallel v_\perp v - \alpha v_\parallel v_\perp\right] \qquad (s = -3)$$

$$\left\{\frac{1}{1 + \frac{\alpha}{\Pi} v_\parallel^4} + \frac{\Pi}{\kappa} v_\parallel \int_0^{v_\perp} dv_\perp \, v^{-3} \exp\left[-\frac{mv_\perp^2}{2kT} + \frac{\Pi}{2\kappa} v_\parallel v_\perp v + \alpha v_\parallel v_\perp\right]\right\} \qquad (7.3.24)$$

These forms are valid up to $v_{\perp *} \equiv v_\parallel \left(\frac{B_L}{B_r} - 1\right)^{-1/2}$.

For the magnetically confined region III,

$$f = \exp\left[\int_{v_{\perp *}}^{v_\perp} P \, dv_\perp\right] \left\{\int_{v_{\perp *}}^{v_\perp} Q \exp\left[-\int_{v_{\perp *}}^{v_\perp} P \, dv_\perp\right] + f(v_\parallel, v_{\perp *})\right\} \qquad (7.3.25)$$

where $f(v_\parallel, v_{\perp *})$ is found from the appropriate region II expression.

A dimensionless parameter analogous to the $\psi \equiv \nu kT/\dot{W}$ of section 7.2 is now introduced for KKP distributions, representing the relative effectiveness of collisions in changing particle velocity compared with the heating rate. When ν and $\dot{W}$ vary with particle velocity, this parameter will be generalized to $\langle\nu\rangle kT/\langle\dot{W}\rangle$, where "$\langle\ \rangle$" is the velocity space average of the enclosed quantity. The distribution function is expected to be dependent on ψ. To have ψ unambiguously defined from the onset, Maxwellian velocity space averages will be used: $\psi = kT/\langle\tau_c\rangle_M \langle\dot{W}\rangle_M$.

Here τ_c is the collision time. $\langle\nu\rangle_M$ is not used because, from (7.3.7),

$$\langle\nu\rangle_M = 4\pi \left(\frac{m}{2\pi kT}\right)^{\frac{3}{2}} \Pi \int_0^\infty v^{s+2} \exp\left(-\frac{mv^2}{2kT}\right) dv$$

$$= \frac{s}{\sqrt{\pi}} \Pi \left(\frac{2kT}{m}\right)^{\frac{s}{2}} \int_0^\infty dx \, x^{((s+1)/2)} \, e^{-x} \qquad (7.3.26)$$

$$= \frac{2}{\sqrt{\pi}} \Pi \left(\frac{2kT}{m}\right)^{\frac{s}{2}} \Gamma\left(\frac{s+3}{2}\right)$$

For $s < -3$, rapid scattering near $v = 0$ causes $\langle\nu\rangle$ to diverge. To avoid this problem it is more meaningful to use the reciprocal of the mean collision time τ:

$$\frac{1}{\langle \tau_c \rangle} = \frac{\sqrt{\pi}\ \Pi\ (\frac{2kT}{m})^{s/2}}{2\ \Gamma(\frac{3-s}{2})} \qquad (7.3.27)$$

$\langle \dot{W} \rangle_M$ can be evaluated from the power absorption implied by (7.3.3) and the number of particles crossing the resonance zone.

The power absorption for the energy increment given by (7.3.3) depends on how many particles of each $v_\parallel$ cross an area A_r of resonance zone surface per second. For a symmetrical magnetic mirror with two resonance zones, the power absorbed is

$$P = 2A_r \int_{-\infty}^{\infty} v_\parallel\, dv_\parallel \int_0^{\infty} 2\pi v_\perp\, dv_\perp\, f(v_\parallel, v_\perp)\, \overline{\Delta W_\perp} = \frac{\pi e E^2}{2B_r'} A_r n_r \qquad (7.3.28)$$

Note that this result does not depend on the form of the distribution function. If the radial profile of density at the resonance zone falls off as $n(r, z_{res}) = n_{ro} \exp(-\frac{r^2}{L^2})$, where L is the radial scale length, then the total power absorbed is

$$P = \frac{\pi^2 e E^2 L^2}{2B_r'} n_{ro} \qquad (7.3.29)$$

The number of particles passing through both resonance zones across area A_r per unit time is

$$\dot{N} = 2A_r \int_{-\infty}^{\infty} dv_\parallel\, v_\parallel \int_0^{\infty} 2\pi v_\perp\, dv_\perp\, f(v_\parallel, v_\perp) \equiv 2A_r n_{res} \langle v_\parallel \rangle \qquad (7.3.30a)$$

For a Maxwellian, $\dot{N}_M = A_r\, n_r\, (\frac{8kT}{\pi m})^{1/2}$ (7.3.30b)

The mean absorption per particle is

$$\langle \Delta W \rangle_M = \frac{P}{\dot{N}_M} = \frac{\pi e E^2}{2B_r'} (\frac{8kT}{\pi m})^{-1/2} \qquad (7.3.31)$$

The number of particles penetrating the resonance zone is

$$N = 16\pi \int_0^{\infty} v_\perp\, dv_\perp \int_0^{\infty} dv_\parallel\, v_\parallel\, f(v_\parallel, v_\perp) \int_0^{z_u} \frac{dz}{v_\parallel(z)} \qquad (7.3.32a)$$

where z_u is the turning point for trapped particles and the wall position for untrapped particles. For a parabolic mirror this reduces to

$$N = 2\pi\, (\frac{r}{\beta})^{1/2}\, A_r\, n_r \left\langle \frac{v_\parallel}{v_\perp} \right\rangle \qquad (7.3.32b)$$

In a Maxwellian plasma, this is $N = 2\, (\frac{r}{\beta})^{1/2}\, A_r\, n_r$ (7.3.32c)

Thus the mean rate of energy absorption is

$$\overline{\dot{W}}_M = \frac{P}{\dot{N}_M} = \frac{\pi e E^2}{4B_o} (r(r-1))^{-1/2} \qquad (7.3.33)$$

Consequently, for a Maxwellian plasma in a parabolic mirror the dimensionless parameter characterizing a KKP distribution is

$$\psi = \frac{mB_o\ \Pi\ (\frac{r}{\pi}(r-1))^{\frac{1}{2}}\ (\frac{2kT}{m})^{1+\frac{s}{2}}}{eE^2\ \Gamma(\frac{3-s}{2})} \qquad (7.3.34)$$

Table 7.1 lists these dimensionless parameters for the principal cases of interest.

The Fortran program DISREXF1 was written to numerically obtain KKP distribution of type 1, since this seemed to be the power law dependence most appropriate for the plasmas in this investigation. The value of wall potential ϕ was adjusted so as to bring the outflow particle flux in the loss region equal to the ionization rate between resonance zone and midplane. This is analogous to the ϕ solutions of Chapter 5, but the modeling should be much closer to actuality, since both scattering and ECRH effects are included. However, the results of this program did not quite measure up to the hopes of its maker. For realistic values of collision rate (evaluated for each velocity space bin separately), the potential at the wall tended toward zero, signaling the breakdown of the hybrid simplex approximation. This means that there has to be a potential increase between the resonance zone and the maximum magnetic field position, to open up the loss region just enough to establish equality of fluxes. The density peak ratios and half widths were small in this model, as as indicated in figure 7.14.

To eliminate the possiblility that unknown errors were occurring in the numerical evaluation of the KKP type 1 distribution, the program DISREXH was writen which incoprates the KKP type 0 form. In the loss cone the value of $f(\vec{v})$ was reduced by the factor, $(1 + \frac{1}{\nu_e \tau_i})^{-1}$. For a highly collisional case, the loss cone is filled in so that the distribution function approaches the KKP expression of the trapped region. If the loss

time is quite short, this factor tends to zero, and the loss region is empty. This model was successful in predicting the observed features of the resonance zone. The density profile has the correct shape, and the half width decreases with increasing pressure, as does the density peak ratio. The major change between this model and those of section 7.2, which predicted an increase of FWHM with neutral density is the inclusion of loss region effects. Table 7.3 summarizes the results of DISREXH for a series of runs in which the system pressure was varied.

The argument as to why peaks get narrower when pressure gets higher is as follows:

(1) Increased scattering will always affect particles with large resonance values of $v_{\parallel}$ more than those of low $v_{\parallel}$, which will still be strongly heated. The parallel velocity for which heating is of greater influence than collisions becomes progressively smaller as neutral pressure is increased. Thus, the strongly heated particles comprise a set with mean turning points ever closer to the resonance zone as pressure increases.

(2) In an ECRH distribution (in resonance zone velocity space) particles are spread out in $v_{\perp}$ rather widely compared with a Maxwellian. Particles are not as concentrated at low $v_{\perp}$, where the loss region is located. Collisions tend to restore isotropic contours, which means that particles enter the loss cone and escape. This reduces the background density. Even though the number of strongly heated particles is decreased with higher

neutral pressure, so is the background plasma. Thus the density peak ratio does not decrease with system pressure as steeply as might be expected. This is shown in the sequence of profile variables given in figures 7.15-7.24. The preservation of peak sharpness as backgound particles are removed is also evident.

Figures 7.15, 7.16, 7.17 and 7.18 show the contours of the distribution, n vs. z, $\langle E_\perp \rangle$ vs. z and $\langle E_\parallel \rangle$ vs. z for for ψ = .081. The same variables are shown in figures 7.19-7.22 for ψ = .222, and in figures 7.23-7.26 for ψ = .379.

Except in very special cases, the ion saturation current FWHM is very close in value to the density FWHM, as shown in Appendix G. This justifies the comparison of I_{isat} FWHM's observed experimentally with the density FWHM's of the previous models, given in figure 7.27. The models incorporating the finite grid approximation have had their values adjusted for finite grid effects, from the results of Appendix C. The 30x30 midplane grid of DISREX has a multiplicative factor of $\sim\frac{1}{2}$ correction factor for its lowest FWHM values, while For the 60x60 resonance grid plan of DISREX the factor is ~2. Only the DISREXH model has both the proper magnitude of FWHM's and the proper dependence with pressure.

7.4 Comparison with other ECRH distribution models.

Lieberman and Lichtenberg[5] used a Fokker-Planck operator on an isotropic distribution to find $f(\vec{v})$. The assumption of an isotropic distribution is not a good one in light of the present results, so that such models will have limited applicability.

A recent bounce averaged Fokker-Planck code for rf-heated plasmas has been presented by Stallard, Matsuda, and Nevins.[6] Their program gives detailed information about scattering rates, loss rates, and power flow between particle species. The density profile is a specified boundary condition, so that it is not possible to calculate resonance density effects self-consistently.

Cohen[7] assumed Maxwellian passing populations in a square well, Fokker-Planck code. Trapped fractions of velocity space similar to those of Chapter 4 were used. The plasma potential was determined from an electron Boltzmann relation, $\phi = (kT_e/e)\ \ell n\ (n_e/n_{eo})$.

A program for finding $f(\vec{v})$ can be done to any level of complexity, and the list given here by no means exhausts what has been done in the recent past. The writer attempted a one-dimensional code for self-consistent calculation for finding n(z) and ϕ(z) along a field line of a mirror with ECRH with ionization, charge exhange, loss region, and scattering terms all included. The code swelled to over 800 Fortran lines before it was given up as being too time consuming a project. And those were just the initialization of variables.

The important issue, in the opinion of this writer, is not whether a simulation mimics the physical reality of an experiment in all its devious complexities, but rather whether one is including the relevant physics at reasonable computational cost. In view of the fact that the experimental results are in accord with the programs which include a potential modified loss cone, a generalized scattering term, and a relatively simple ECRH rate, it is my contention that this has been accomplished.

Table 7.1

Maxwellian Means for Power Law Scattering

s	case	$\langle\nu\rangle_M$	$\langle\tau_c\rangle^{-1}$	Π	$\frac{\psi}{\frac{mB_o\Pi}{eE^2}\left[\frac{\Gamma}{\pi}(r-1)\right]^{1/2}}$
1	constant σ;	$\Pi\left(\frac{8kT}{\pi m}\right)^{\frac{1}{2}}$	$\Pi\left(\frac{\pi kT}{2m}\right)^{\frac{1}{2}}$ $n_n\sigma$		$\left(\frac{2kT}{m}\right)^2$
0	constant ν	Π	Π^{-1}	ν	$\frac{2}{\sqrt{\pi}}\left(\frac{2kT}{m}\right)^{3/2}$
-3	Coulomb scattering	---	$\frac{\Pi}{2\pi}\left(\frac{\pi kT}{2m}\right)^{\frac{3}{2}} 8\pi n \left(\frac{e^2}{4\pi\varepsilon_o m}\right)^2 \ln \Lambda \frac{1}{2}\left(\frac{2kT}{m}\right)^{-1/2}$ $= (\nu_{ee}+\nu_{ei})v^3$		

Table 7.2

Summary of DISREX predictions for a DC Machine-like device

Input variables: $n_p = 5\times10^{15}$ m^{-3} $T_e = 10$ eV

$B_o = .0175$ T $B_r = .0875$ T $r = 5.$

$Z_{res} = .5$ m gas: He

$g = 10^{-4}$ (E = 2625 V/m)

Pressure (gauge torr)	$\bar{\nu}$ (s^{-1})	$\dot{W}_{mean}$ (eV/s)	$\bar{\dot{W}}_{res}$ (eV/s)	ψ	$\frac{n_r}{n_o}$	FWHM (cm)	$\frac{\Delta B}{B_r}$
0.0	1.34×10^5	3.98×10^6	3.68×10^7	.336	3.392	6.64	.195
5×10^{-6}	2.09×10^5	4.34×10^6	3.43×10^7	.482	2.756	7.38	.217
10^{-5}	2.85×10^5	4.03×10^6	3.04×10^7	.707	2.273	8.36	.245
2×10^{-5}	4.35×10^5	3.22×10^6	2.4×10^7	1.35	1.859	9.81	.287
3×10^{-5}	5.85×10^5	2.57×10^6	1.93×10^7	2.28	1.610	12.65	.375
5×10^{-5}	8.82×10^5	1.83×10^6	1.40×10^7	4.82	1.398	15.56	.464
7×10^{-5}	1.18×10^6	1.39×10^6	1.09×10^7	8.49	1.279	18.29	.542
10^{-4}	1.63×10^6	1.04×10^6	8.25×10^6	15.7	1.194	22.58	.657
1.5×10^{-4}	2.37×10^6	7.85×10^5	6.29×10^6	30.2	1.136	34.06	.906
2×10^{-4}	3.11×10^6	6.49×10^5	5.31×10^6	47.1	1.109	56.89	1.16

NOTES FOR TABLE 7.2

This model evaluates ν and $\dot{W}$ in every bin of a 30x30 grid in midplane velocity space. Loss effects are not included.

$\dot{W}_{mean}$ is the mean heating rate averaged over all midplane particles.

$\dot{W}_{res}$ is the mean heating rate, averaged only over those partilces that have turning points past resonance.

True neutral density is 1.83×10^{23} times the value of gauge pressure.

$\bar{\nu}$ is the distribution-averaged collision frequency.

$\psi \equiv \nu kT/\dot{\Omega}_{mean}$

Table 7.3

Summary of DISREXH predictions for a DC Machine-like device.

Input variables: $n_p = 10^{16}\ m^{-3}$ $T_e = 10$ eV

$B_o = .0175$ T $B_r = .0875$ T $r = 5$

$Z_{res} = .5$ m gas: He

$g = 10^{-4}$ ($E = 2625$ V/m)

neutral density	$\bar{\nu}$ (s^{-1})	ψ	ϕ (V)	$\frac{n_r}{n_{base}}$	FWHM (cm)	$\frac{\Delta B}{B_r}$
5×10^{16}	1.72×10^5	.06714	21.5	4.42	3.26	.105
10^{17}	1.76×10^5	.0687	16.1	4.38	3.17	.102
2×10^{17}	1.84×10^5	.07183	9.52	4.32	3.01	.0969
5×10^{17}	2.08×10^5	.08122	<0	4.12	2.54	.0812
5×10^{18}	5.7×10^5	.221	<0	2.48	.78	.0249
10^{19}	9.71×10^5	.379	<0	2.06	.56	.0178
3×10^{19}	2.58×10^6	1.005	<0	1.75	.41	.0131

NOTES FOR TABLE 7.3

$\nu = 90^o$ collision rate for the Maxwellian distribution with the given neutral density.

"Neutral pressure" is true, not gauge, pressure for helium.

ϕ is the predicted potential drop to the wall, if positive. If $\phi < 0$, an increase of potential is predicted from resonance zone to maximum B position.

The distribution is KKP type 0, attentuated in the loss region by the factor $(1 + 1/(\tau_{loss}\nu))^{-1}$.

Hybrid simplex approximation is used for the loss region.

Figure 7.1 $\frac{n}{n_o}$ vs. $\frac{B}{B_r}$ (simple model).

Figure 7.2a $\frac{n_r}{n_o}$ vs ψ (simple model).

Figure 7.2b FWHM/B_r vs ψ (simple model).

Figure 7.3 FWHM/B_r vs $\frac{n_r}{n_o} - 1$ (simple model).

NOTE: In figures 7.1-7.3 $r = B_r/B_o$ and $\psi = \frac{\nu\ kT}{\dot{W}}$.

Figure 7.4 $I_{e\perp}$ vs. probe bias (simple model) .

Figure 7.5 Divisions of velocity space for the KKP distribution.

I—trapped at any perpendicular speed

II—-untrapped region

III--trapped region. Integration of $f(v_\parallel, v_\perp)$ proceeds from the line separating this region from region II.

Figure 7.6 Midplane velocity space distribution function solution of DISREX.

Figure 7.7 Density profile solution of DISREX.

Figure 7.8 Mean perpendicular energy profile found by DISREX.

Figure 7.9 Mean parallel energy profile found by DISREX.

Figure 7.10 Mean parallel particle flux found by DISREX.

Parameters for plots 7.6-7.10:

T_e = 10 eV ε = .0001 B_r = .0875 B_o = .0175 Z_{res} = .5 n_g = 1.83×10^{16} (helium) ψ = .755

Figure 7.11 Mean heating rate vs. pressure, from DISREX code.

Figure 7.12 FWHM of density peak vs. pressure, from DISREX code.

Figure 7.13 $\frac{n_r}{n_o}$ vs. pressure, from DISREX code.

Figure 7.14 Predictions of KKP type 1 distribution for a helium plasma in the DC Machine.

Figure 7.15 Midplane velocity distribution.

Figure 7.16 Density vs. z.

Figure 7.17 Mean perpendicular energy vs. z.

Figure 7.18 Mean parallel energy vs. z.

NOTE: DISREXH predictions with ψ = .081

Input variables: T_e = 10 eV

$n_o = 10^{16}$ m^{-3} $n_g = 5\times10^{17}$ m^{-3}

B_o = .0175 T B_r = .0875 T

B_L = .125 T z_r = .50 m

Figure 7.19 Midplane velocity distribution.

Figure 7.20 Density vs. z.

Figure 7.21 Mean perpendicular energy vs. z.

Figure 7.22 Mean parallel energy vs. z.

NOTE: DISREXH predictions with ψ = .22

Input variables: T_e = 10 eV

$n_o = 10^{16}\ m^{-3}$ $n_g = 5\times10^{17}\ m^{-3}$

B_o = .0175 T B_r = .0875 T

B_L = .125 T z_r = .50 m

Figure 7.23 Midplane velocity distribution

Figure 7.24 Density vs. z.

Figure 7.25 Mean perpendicular energy vs. z

Figure 7.26 Mean parallel energy vs. z

NOTE: DISREXH predictions with ψ = .38

Input variables: T_e = 10 eV

$n_o = 10^{16}\ m^{-3}$ $n_g = 5\times10^{17}\ m^{-3}$

B_o = .0175 T B_r = .0875 T

B_L = .125 T z_r = .50 m

Figure 7.27 Comparison of predicted half-widths of three models with experimental values, vs. pressure.

FIGURE 7.1 DENSITY AS A FUNCTION OF MAGNETIC FIELD (SIMPLE MODEL).

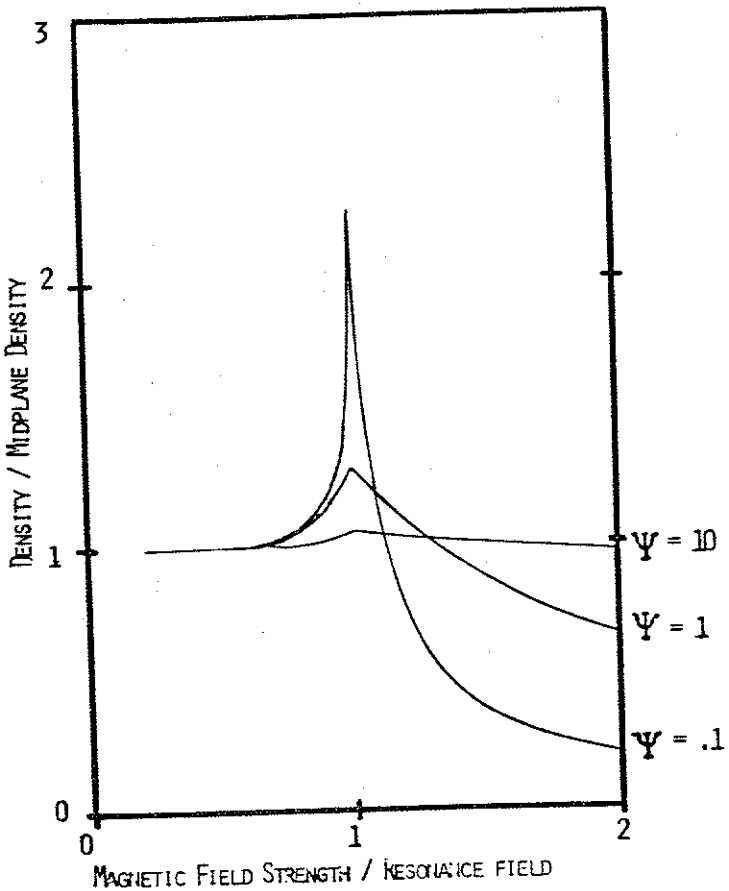

FIGURE 7.2 A $\frac{N_T}{N_0} - 1$ VS Ψ (SIMPLE MODEL)

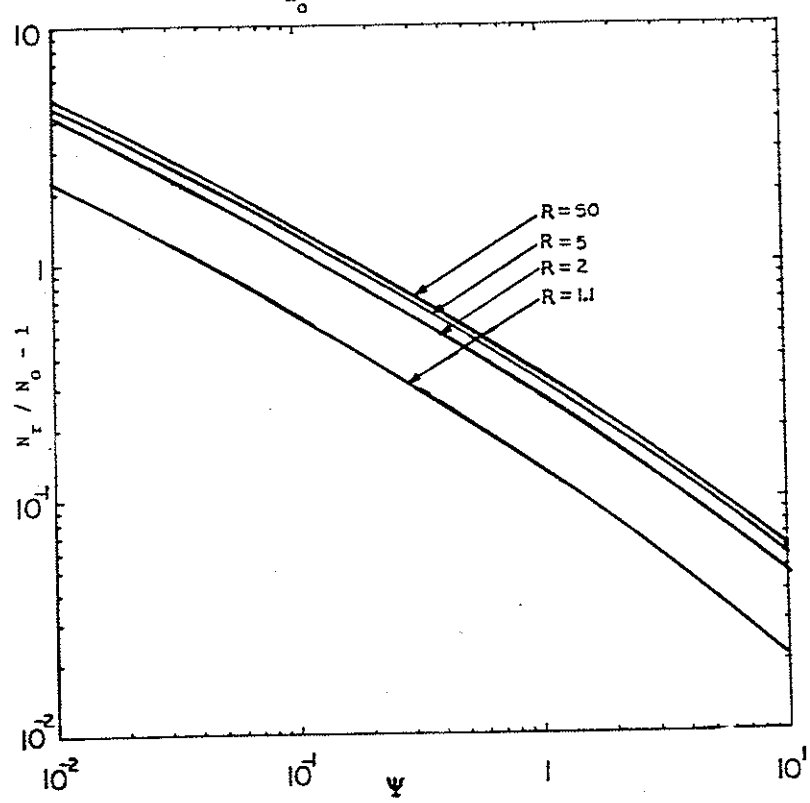

FIGURE 7.2B DENSITY FWHM VS. ψ (SIMPLE MODEL)

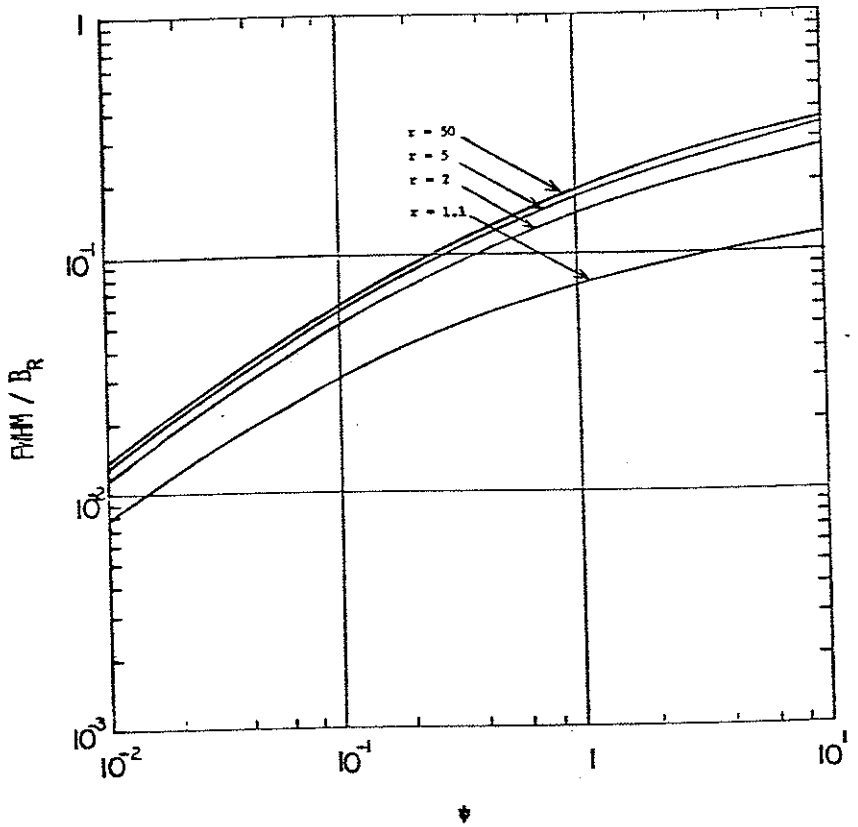

FIGURE 7.3 $\Delta B/B_R$ VS. $\frac{N_R}{N_0} - 1$ (SIMPLE MODEL)

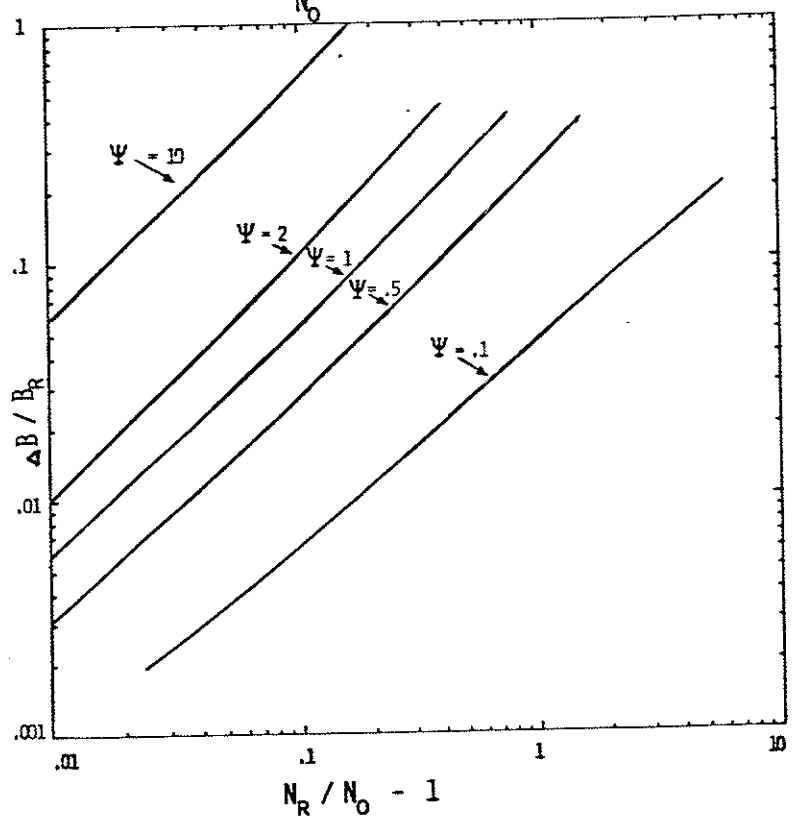

FIGURE 7.4 $I_{E\perp}$ VS. eV / kT_E FOR SIMPLE ANALYTIC MODEL.

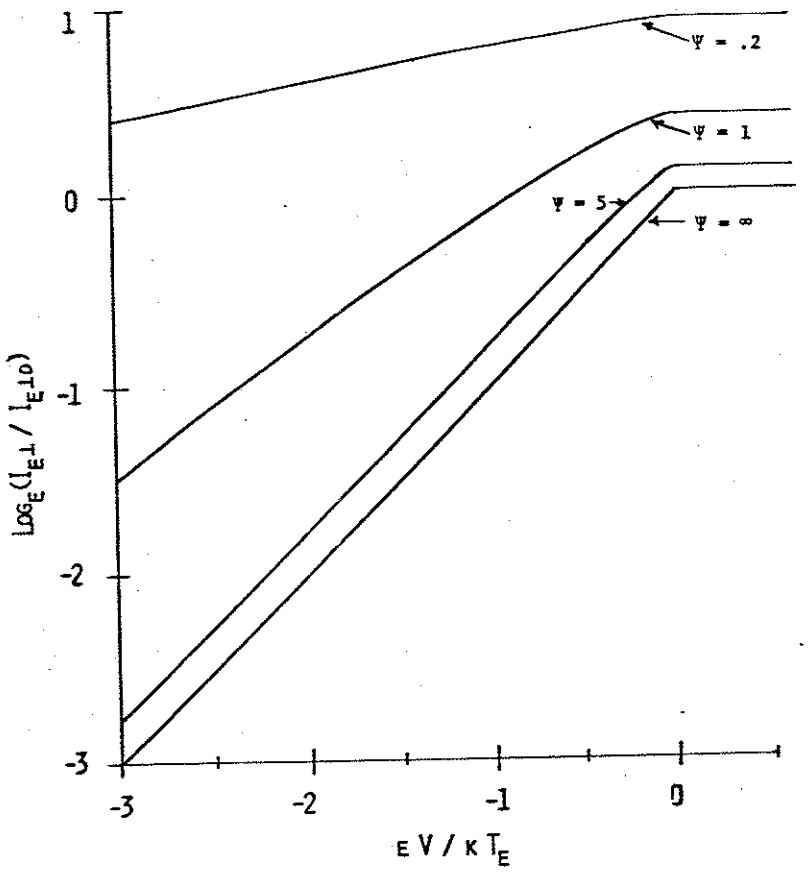

FIGURE 7.5

Regions of resonance zone velocity space (idealized)

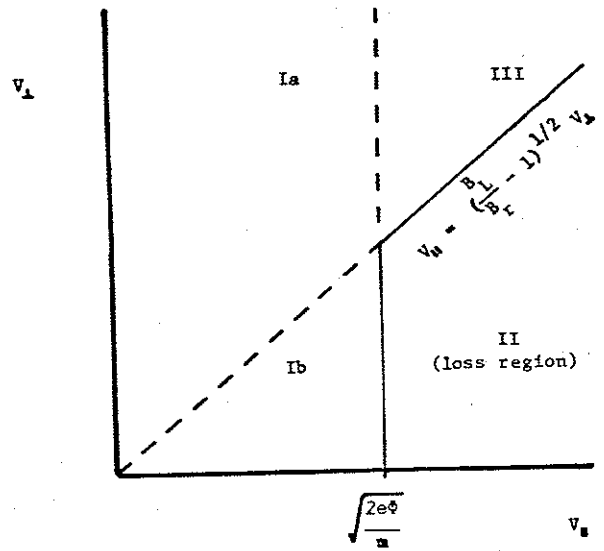

FIGURE 7.6

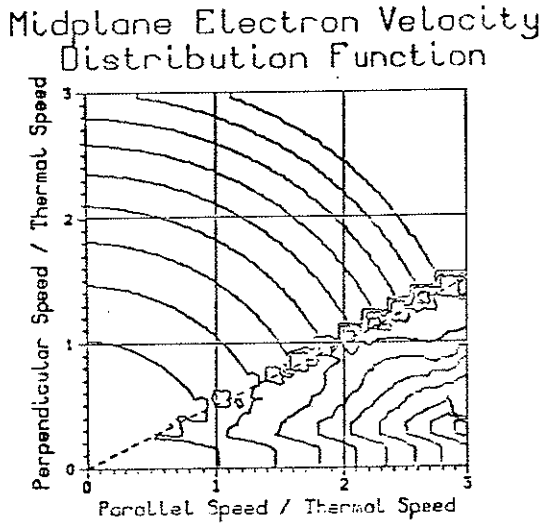

Solid curves are contours representing a $\sqrt{10}$ change in the value of the distribution. The dotted line shows the condition for a turning point at the resonance zone.

FIGURE 7.7

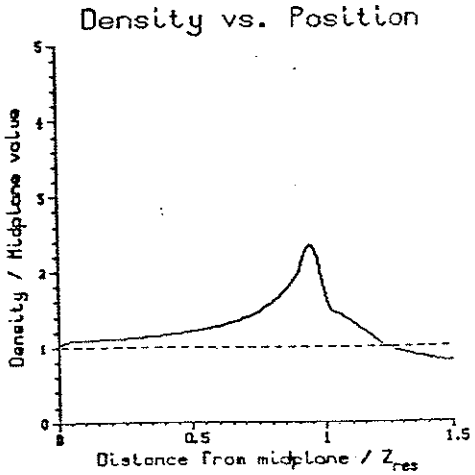

Density vs. distance from midplane for the distribution function represented in figure 7.6. The dashed line is the (constant) Maxwellian value.

FIGURE 7.8

Perpendicular Energy vs. Position

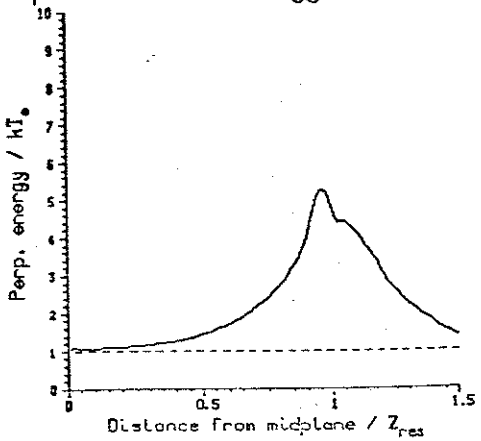

Mean value of perpendicular energy for the distribution function represented in figure 7.6. The dashed line shows the Maxwellian value.

FIGURE 7.9

Parallel Energy vs. Position

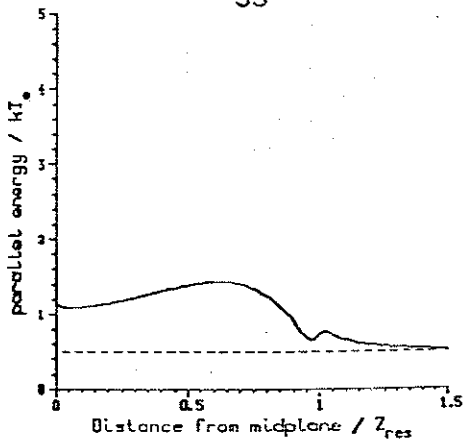

Mean value of parallel energy vs. distance from midplane, for the distribution function represented in figure 7.6. Dashed line shows the Maxwellian value.

FIGURE 7.10

Parallel Particle Flux vs. Position

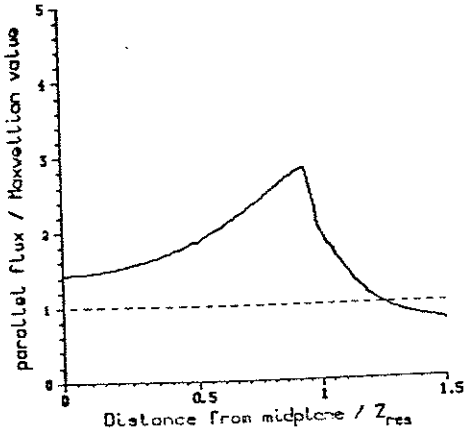

Product of the value of density and mean parallel speed for the distribution function represented in figure 7.6. Dashed line shows the Maxwellian value.

Figure 7.11 Mean heating rate vs. pressure, from DISREX code.

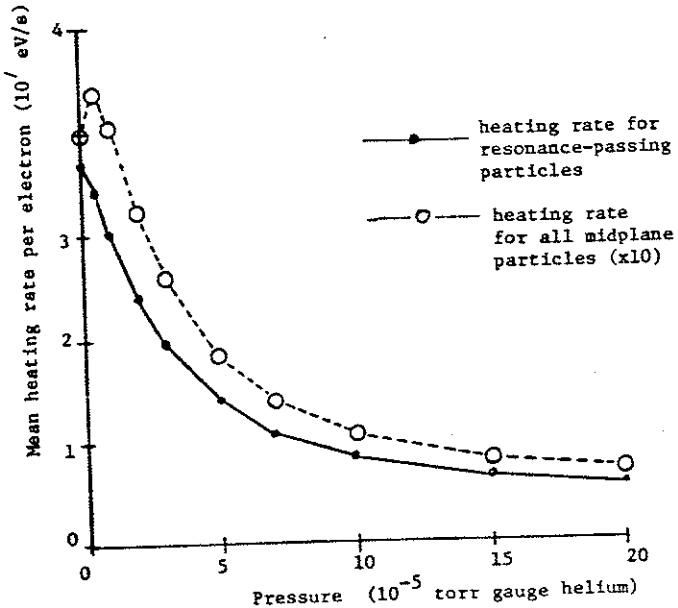

FIGURE 7.12 FWHM OF DENSITY PEAK VS. PRESSURE, PREDICTED BY DISREX CODE.

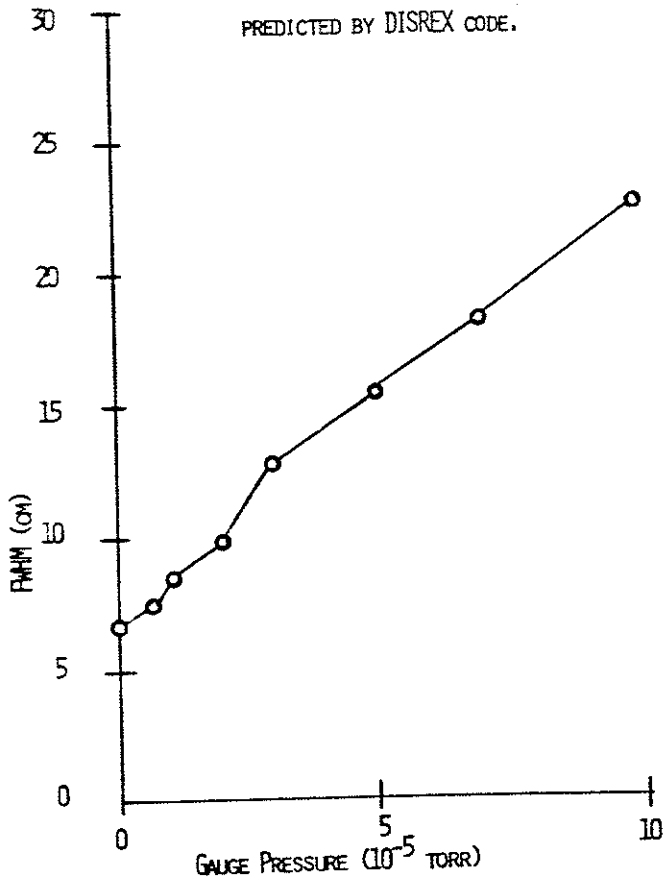

Figure 7.13 n_r / n_o vs. pressure, from DISREX code.

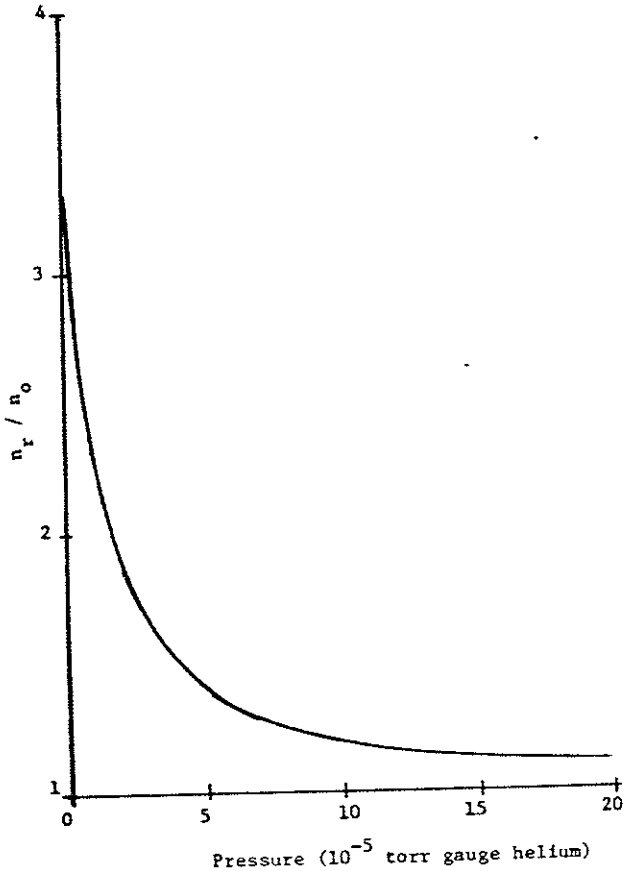

FIGURE 7.14 PREDICTIONS OF KKP TYPE 1 DISTRIBUTION FOR A HELIUM PLASMA WITH DC MACHINE-LIKE PARAMETERS.

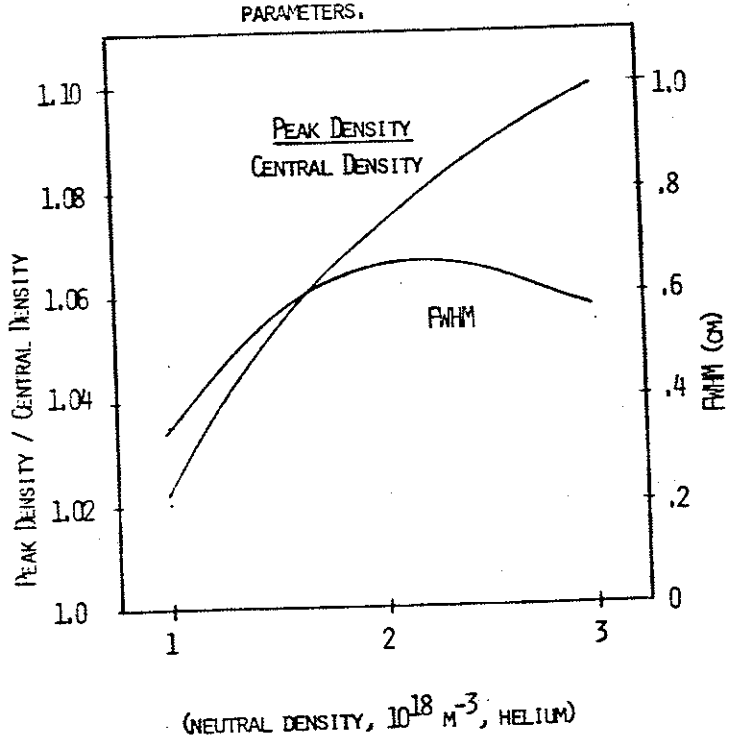

FIGURE 7.15

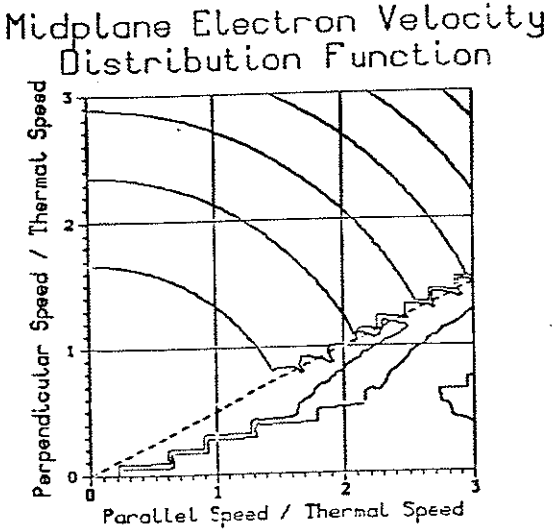

Solid curves are contours representing a factor-of-two change in the value of the distribution function. The dashed line shows the condition for a turning point at the resonance zone.

FIGURE 7.16

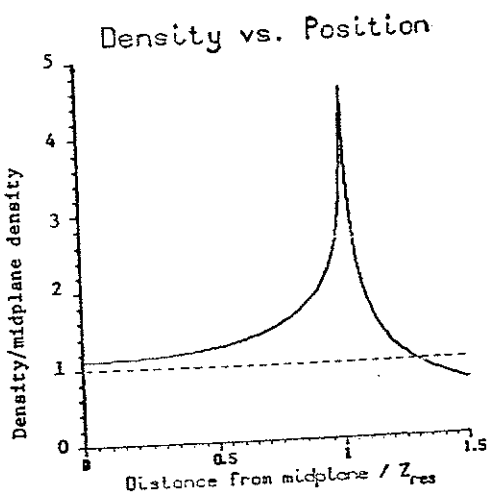

Density vs. distance from midplane for the distribution function represented in figure 7.15. The dashed line is the (constant) Maxwellian value.

FIGURE 7.17

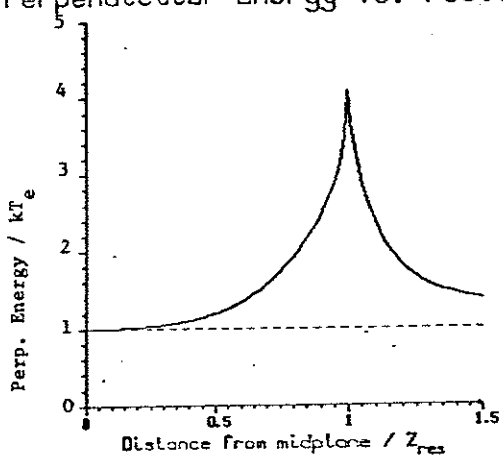

Mean value of perpendicular energy for the distribution function represented in figure 7.15. The dashed line gives the Maxwellian value.

FIGURE 7.18

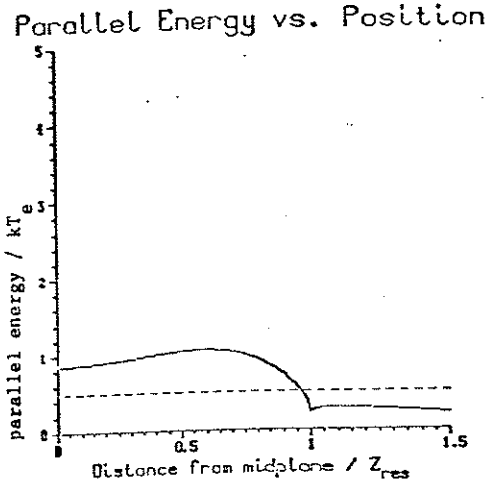

Mean value of parallel energy vs. distance from midplane, for the distribution function represented in figure 7.15. Dashed line shows the Maxwellian value.

FIGURE 7.19

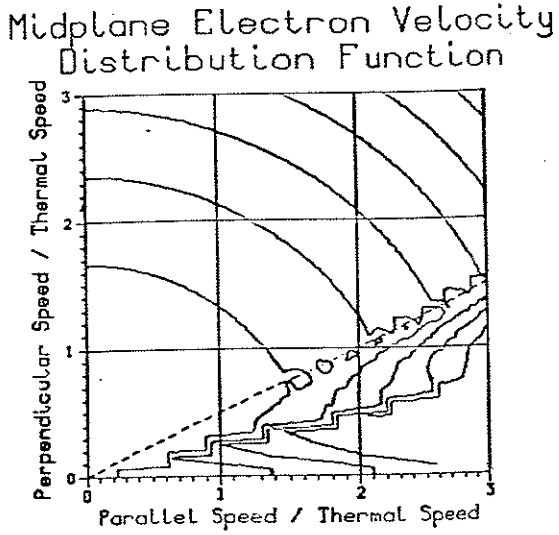

Solid curves are contours representing a factor-of-two change in the value of the distribution function. The dashed line shows the condition for a turning point at the resonance zone.

FIGURE 7.20

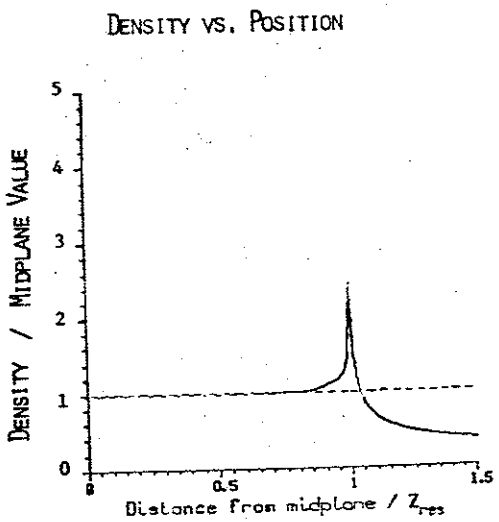

Relative density of electrons in a parabolic mirror. Solid curve gives values from the calculated distribution. Dashed curve gives result for a Maxwellian distribution.

FIGURE 7.21

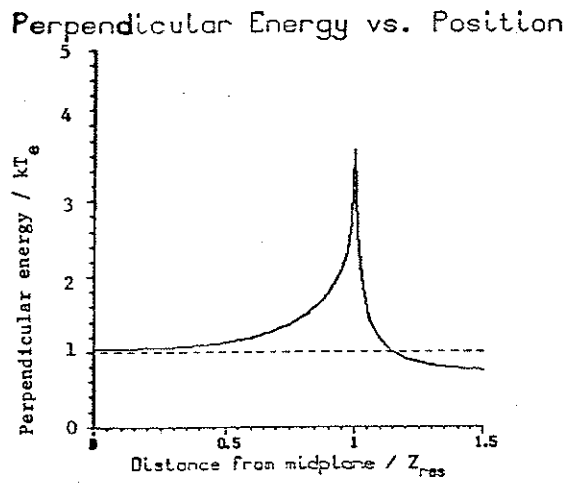

Mean value of perpendicular energy for the distribution function represented in figure 7.19. The dashed line shows the Maxwellian value.

FIGURE 7.22

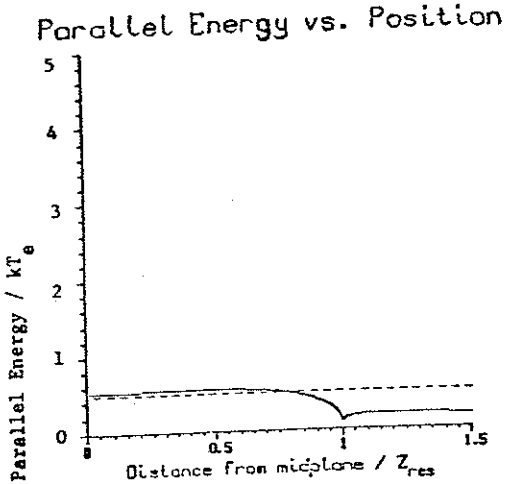

Mean value of parallel energy vs. distance from midplane, for the distribution function represented in figure 7.19. Dashed line shows the Maxwellian value.

FIGURE 7.23

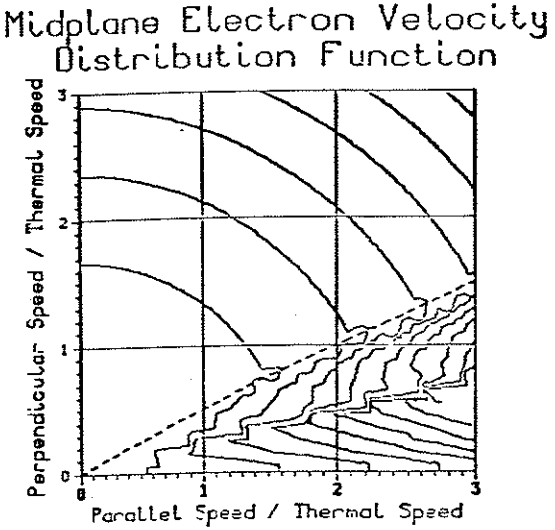

Solid curves are contours representing a factor-of-two change in the value of the distribution function. The dashed line shows the condition for a turning point at the resonance zone.

FIGURE 7.24

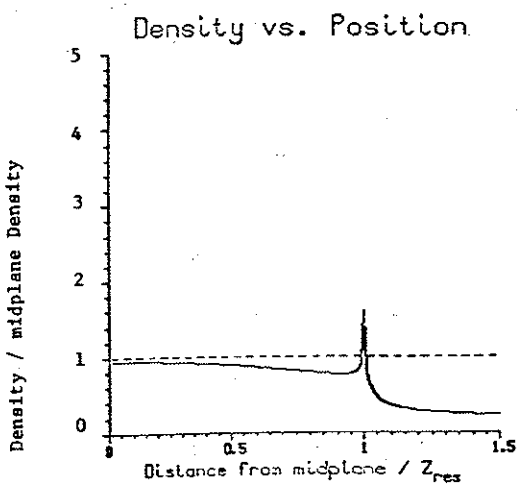

Density vs. distance from midplane for the distribution function represented in figure 7.23. The dashed line is the (constant) Maxwellian value.

FIGURE 7.25

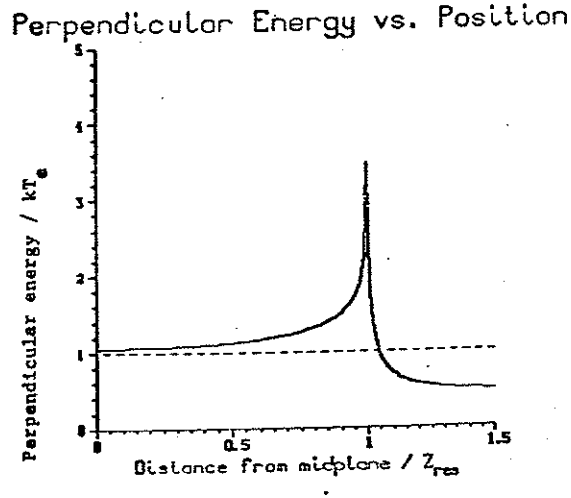

Relative values of perpendicular energy in a parabolic mirror. Solid curve is mean value for the calculated distribution. Dashed curve shows the mean value for a Maxwellian.

FIGURE 7.26

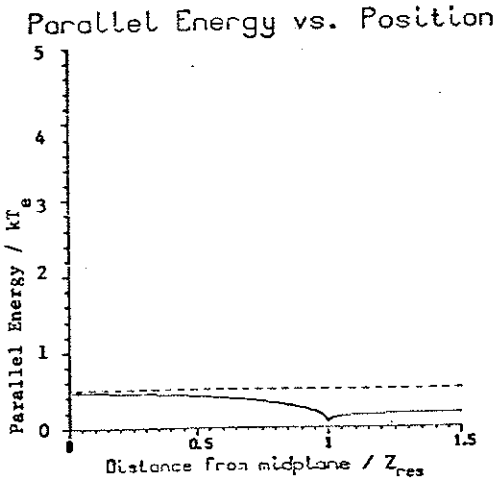

Mean value of parallel energy vs. distance from midplane, for the distribution function represented in figure 7.23. Dashed line shows the Maxwellian value.

Figure 7.27 Comparison of observed I_{isat} FWHM's with model predictions for density FWHM , vs. pressure.

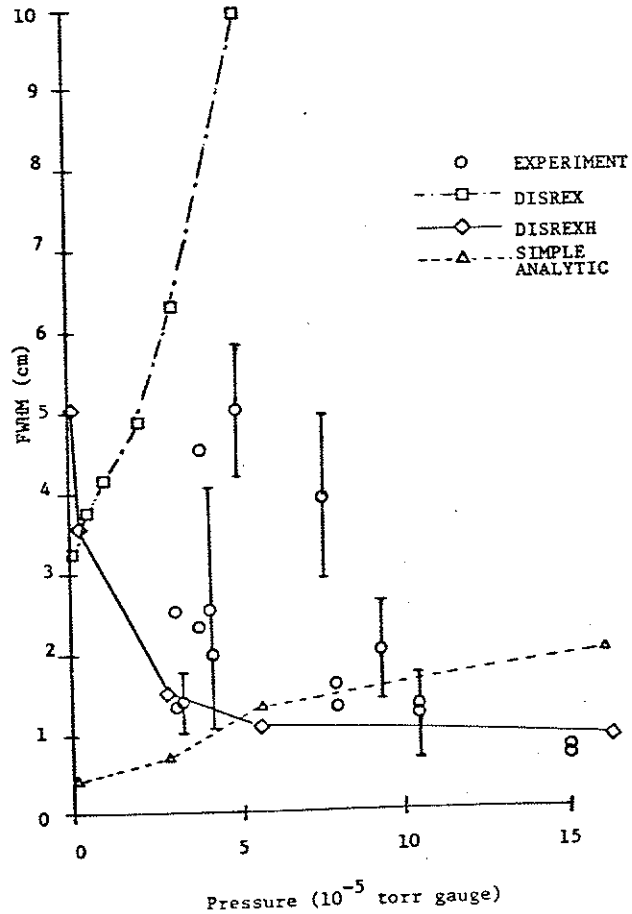

REFERENCES FOR CHAPTER 7

[1]A. F. Kuckes, Plasma Physics 10, 381 (1967).

[2]J. C. Sprott and P. Edmonds, Phys. Fluids 14, 2703 (1971).

[3]O. Eldridge, Bull. Am. Phys. Soc. 15, 407 (1970).

[4]J. C. Sprott, Phys. Fluids 14, 1795 (1971).

[5]Lieberman and A. J. Lichtenberg,, Plasma Physics 15, 125 (1973).

[6]B. R. Stallard, Y. Matsuda and W. M. Nevins, UCRL 87674, (Lawrence Livermore Laboratory, 1982).

[7]R. H. Cohen, Nuc. Fusion 21, 209 (1982).

[8]H. Ikegami, H. Ikezi, T. Kawamura, H. Momota, K. Takayama, and Y. Terashima, in Plasma Physics and Controlled Nuclear Fusion Research (Intl. At. Energy Agency, Vienna, 1969), Vol. II, p. 423.

Chapter 8

Conclusions and Implications

8.1 Uses of the cut-out Maxwellian results

The "cut-out Maxwellian" densities of chapter 4 are essentially weighted trapped-velocity-space fractions. These will find applicability wherever the thermal transit time for a particle in the loss region is much less than the 90^{o} scattering time. Areas of possible use include calculations of magnetospheric currents,[1] calculation of densities and losses in plasmas with interior grids,[2] and currents through divertors.[3]

8.2 Discussion of basic mirror models

The general models of chapter 5 predict the scaling of central plasma potential. They fail to predict resonance phenomena, and become increasingly dubious when n_{res}/n_o increases to a significant ratio. The correlations between theory and observation is given in Table 8.1 for plasma potential values at midplane. The best of the models examined is based on a balance of mean loss, ionization, and scattering rates between partial Maxwellian distributions across the boundary between trapped and untrapped space. To model other devices, the true trapped-untrapped boundary must be used. The procedure of section 4.5 is then to be applied to the revised boundary.

8.3 Resonance zone models

The width of the resonance zone is determined by the degree to which turning points are clustered in the resonance region. Calculating this effect requires explicit determination of the electron distribution function as affected by ECRH. Models of increasing order of sophistication have been presented which are capable of explaining the more obvious resonance zone phenomena.

The most puzzling experimental obervation, the narrowing of resonance dips at increased pressure, is explained by models which include enhanced scattering into the loss cone.

Collision rates, lengths, and heating rates will have to be changed for modeling an experiment other than the present device, but the procedures used to determine the ECRH-modified distribution remain the same.

For devices with ψ and parabolic field parameter β similar to the DC machine (~.1 to 1 and ~ 15 m^{-2}, respectively), the resonance zone density peak is expected to be on the order of $\frac{\Delta B}{B_{res}}$ ~ .25±.1 The ratio of resonance density to values slightly off-resonance is expected to be ~1.2 to 4.

8.4 Power absorption with ECRH-modified distribution functions

As shown in section 7.3, resonance zone density is the most important feature for power absorption. The temperature, on the other hand, depends on how many system particles share this power. Thus by adjustment of the density profile one can optimize mean energy and heating. The resonance density peak means that heating estimates based on the midplane density values can be seriously in error.

The mean heating rate per particle will change for three reasons:

(1) The bounce time is decreased, on the average, for particles because the ratio $\frac{v_\perp}{v_\parallel}$ is increased. The magnitude of this effect can be calculated from the KKP distributions and the numerical models of chapter 7.

(2) The commonly used ECRH rate which assumes $v_\parallel$ constant through a resonance zone interaction, fails to hold for many particles of the ECRH perturbed distribution. These feature a large fraction of particles that have turning points relatively near the resonance zone. The maximum energy gain does not approach ∞ as parallel electron speed at resonance approaches zero, as predicted by the Kuckes[7] model. Instead the energy gain appraches the finite value given by Lieberman and Lichtenberg:[8]

$$\Delta W_\perp < 1.65\ e\ E\ Z_{res}\{\frac{\omega_{co}}{4\pi}\ (\frac{m}{eE\sqrt{\beta}})^{1/2}\ r^{5/4}\}^{1/2} \qquad (8.4.1)$$

The replacement of an infinite gain with a finite one decreases

the heating rate from that expected in the constant-$v_{\parallel}$ model. The calculation of this correction requires some form of the finite grid approximation, with the heating rate corrected from the simple model in applicable bins. The models developed here can give the heating rate as modified by both these effects.

(3) If a small potential dip exists at resonance, the heating rate per particle is increased slightly. As indicated in Appendix B, this is a negligible effect in the current experiment.

8.5 Potential dip depths

The depth of the potential dip at resonance is given by an ion Boltzmann equation. These are small in the present study, both in theory and experiment, because T_i is small and no mechanism is used to extract trapped ions from an incipient dip. It is necessary to use some form of ion pumping--removal of trapped ions--to set up a usable thermal barrier at resonance. The motivation in obtaining such a thermal barrier is to inhibit electron energy transport between central cell and plug in a tandem mirror. Passive pumping schemes such as that proposed by Kesner,[4] were never observed to occur naturally, despite studies over a wide range of operating parmeters.

8.6 Perturbed averages.

Due to the perturbation of the distribution function by ECRH, the use of Maxwellian averages for such things as collision rates and heating rates can be risky. The interpretation of Langmuir probe data especially, must be done with care, due to the combination of the effects of anisotropic velocity distribution and the non-symmetric collection characteristics of a probe in a magnetic field. Much information can still be gained with Langmuir probes if proper analysis is performed.

8.7 Use of sloshing electron distributions in high temperature plasmas.

A question of relevance to tandem mirror operation is, "how much ECRH power is needed to induce a potential dip of a given size?" This depends on how large a density ratio can be built up at a given position. For a distribution that is of a highly sloshing nature, the proportion of resonance turning particles is almost unity at the resonance zone, and very small at the midplane. Under these conditions at the midplane one has

$$n_{eo} = n_{io} = (1 - \frac{1}{g})n_{io} + \frac{1}{g} n_{io} \qquad (8.7.1)$$

where the first term is the "Maxwellian" ion component whose density is given by

$$n_{i,Boltzmann} = (1 - \frac{1}{g}) n_{io} \exp(-\frac{q\phi}{kT_i}) \qquad (8.7.2)$$

The second term on the RHS of (8.7.1) is the "streaming", or "passing" ion component, whose density along a field line is given by

$$n_{i,pass} = \frac{1}{g} n_{io} [1 - \frac{q\phi}{E_p}]^{-1/2} \qquad (8.7.3)$$

The parameter g of tandem mirror theory is the ratio of passing ions to total ions at the midplane. For simplicity the energy of the passing ions E_i is taken to be kT_i. Then if an electron density peak is established at the resonance zone, with a density peak ratio of $\frac{n_p}{n_{eo}}$ to midplane density, relations (8.7.1), (8.7.2) and (8.7.3) force the quasineutrality relation,

$$\frac{n_p}{n_{eo}} = (1 - \frac{1}{g}) e^x + \frac{1}{g} [1 + x]^{-1/2} \qquad (8.7.4)$$

In (8.7.4) $x \equiv -q\phi/kT_i$. Table 8.1 gives the required density peak ratios for a series of values of g and of the dimensionless potential dip size x.

A series of DISREXH runs, which worked well with DC Machine parameters, were executed with the parameters of a hypothetical large mirror ("GBM I"), with parameters in the range of those that exist or will exist in the near future. Table 8.2 gives the input variables used. Aside from these, the program was not modified

for the new device. The output values show that the values of density peak ratio tend to asymptotically approach 4 as the normalized hf-electric field, $\frac{E_{hf}}{cB_{res}}$, increases. In combination with table 8.1, this means that there is a limit to normalized dip depth x for for a given g. This is because there is a limit to the value of n_p/n_{base} that can be obtained. Figure 8.1 shows the "best possible" x values as a function of g. This means that ECRH at the fundamental should be capable of driving strong dips if ion pumping is efficient.

Table 8.1 also shows that there is a point of diminishing returns in using ECRH power to gain greater values of $\frac{n_{res}}{n_o}$. About 75% of the limiting value is achieved with a dimensionless electric field of $E_{hf} = .0003\ c\ B_{res}$. Still lower values may prove better, since the resonance zone is narrower in that case. Despite the fact that $\frac{n_{res}}{n_o}$ will not be as high, the smaller resonance zone volume means that ion pumping could possibly be made more efficient, with compensatingly higher "g" values. s/.

Thus this model is capable of predicting the quantitative aspects of resonance zones in large devices.

Another issue is that the resonance magnetic field is changed in fusion grade plasmas from its "cold plasma resonance value" B_{cpr} to[5]

$$B_{res} = B_{cpr}\ \gamma\ [1 \pm \cos\theta \cos\varphi\ (1 - \frac{1}{\gamma^2})] \qquad (8.7.5)$$

where $\gamma = (1 - v^2/c^2)^{-1/2}$, θ is the angle between the electron velocity $\vec{v}$ and magnetic field $\vec{B}$, and ϕ is the angle between the wave vector $\vec{k}$ and $\vec{B}$. The "$\pm$" term in (7.8.5) is a doppler shift, while the leading γ accounts for the shift due to relavistic mass increase. Since γ and θ vary from particle to particle there is no longer a unique value for B_{res}. This means local features based on ECRH will broaden. For sloshing particles, however, note that $\cos\theta \to 0$. This means that doppler broadening is lost, and the resonance width is due to the spread in γ alone. The order of magnitude of relativistic broadening of the resonance zone in a plasma of near-resonance-turning particles is

$$\frac{\Delta B}{B_{cpr}}\Big|_{\gamma} = 2(\bar{\gamma} - 1) = \frac{kT_e}{170\ KeV} \qquad (8.7.6)$$

For plasmas with $kT_e/e > 30$ KeV, this spread will be larger than the observed resonance widths.

Table 8.1

Required density peak ratios for given values of x and g

	g					
x	1.5	2.	3.	5.	10.	∞
.2	1.016	1.067	1.119	1.160	1.191	1.221
.5	1.094	1.233	1.371	1.482	1.565	1.649
1.0	1.377	1.713	2.048	2.316	2.517	2.718
2.0	2.848	2.982	5.118	6.027	6.708	7.389
5.0	49.743	74.411	99.078	118.8	133.6	148.4
10.	7542	11013	14680	17620	19820	22030

x = dimensionless dip depth = $-\frac{e\Delta\Phi}{kT_i}$.

$g = \frac{\text{total ion density}}{\text{passing ion density}}$ (at midplane).

Energy of passing ions is set equal to kT_i in this table.

Table 8.2

Summary of DISREXH runs for GBM I

common data for all runs:

$T_e = 10^4$ eV

$n = 10^{20}$ m^{-3} $\quad n_g = 10^1$ m^{-3}

$B_{min} = 1$ T $\quad B_{res} = 2$ T $\quad B_{max} = 3$ T

$Z_{res} = 4$ m $\quad R = 3$

ion species He^+ $\quad \frac{dB}{dz}\Big|_{res} = .5$ T/m

g	ψ	$\frac{n_{res}}{n_{base}}$	$\frac{n_{res}}{n_{mid}}$	FWHM (m)	$\frac{\Delta B}{B_{res}}$
.0001	1.116	1.75	.774	.033	.016
.0002	.279	2.26	2.21	.0601	.053
.0003	.124	3.09	2.85	.1687	.0424
.001	.0116	3.88	3.88	.6549	.169
.003	.00124	3.92	3.92	.750	.195

$$g = \frac{eE_{hf}}{m\omega c} = \frac{E_{hf}}{cB_{res}}$$

Figure 8.1 Maximum practical limits on dip size from ECRH in GBM I

The parameters of this hypothetical large mirror are given in table 8.2

g = total ion density / passing ion density

$$x = \frac{e\Delta V}{kT_i}$$

FIGURE 8.1 MAXIMUM PRACTICAL LIMITS ON DIMENSIONLESS DIP SIZE FROM ECRH

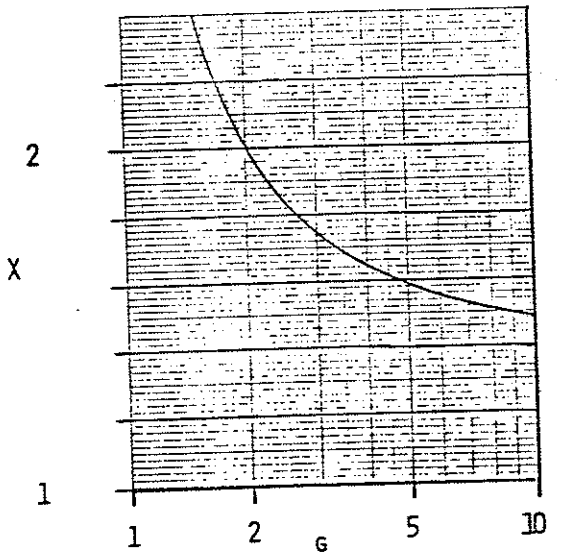

G = ION DENSITY / PASSING ION DENSITY

X = DIP AMPLITUDE / ION TEMPERATURE

REFERENCES FOR CHAPTER 8

[1]S. Knight, Planet. Space. Sci 22, 741 (1973).

[2]A. A. Ware and J. E. Faulkner, Nuc. Fusion 9, 353 (1969).

[3]E. Strait, Ph. D. Thesis, University of Wisconsin, Madison (PLP 813), (Sept., 1979).

[4]J. Kesner, Comments Plasma Phys. Contr. Fus. 5, 123 (1979).

[5]J. W. Schrearer, UCID-19577, (Lawerence Livermore Laboratory, 1982).

[7]A. F. Kuckes, Plasma Physics 10, 367 (1968).

APPENDIX A

Supporting integrals

In the expressions that follow a, b, and c are positive constants, unless otherwise stated. The following definitions are used:

$$\mathrm{erf}(x) = \frac{2}{\sqrt{\pi}} \int_0^x \exp(-t^2)\, dt$$

$$H(x) = \frac{2}{\sqrt{\pi}} \int_0^x \exp(+t^2)\, dt$$

H(x), the error function analog, can be evaluated in terms of the reduced Dawson integral[1]:

$$D_r(x) = \exp(-x^2) \int_0^x \exp(+t^2)dt$$

For $0 \leq x \leq 2$ a good approximation to D_r is

$$D_r(x) = x(.991787 + .104686x - 1.063175x^2 + .610486x^3 - .105105x^4)$$

For $x \geq 2$ a good approximation is

$$D_r(x) = \frac{1}{x}(.5 + .24876877x^{-2} + .57706784x^{-4} - 6.7426249x^{-6} + 105.12441x^{-8} - 464.08774x^{-10} + 623.84286x^{-12})$$

1. $\int dw \exp(-aw)\,[bw+c]^{1/2} =$
$\frac{1}{a}(\frac{b}{a})^{\frac{1}{2}} \exp(ac/b)\,\{\frac{\sqrt{\pi}}{2}\,\mathrm{erf}\,[\frac{a}{b}(bw+c)]^{1/2} - [\frac{a}{b}(bw+c)]^{1/2}\exp[-\frac{a}{b}(bw+c)]\}$

2. $\int dw\,[c-bw]^{1/2}\exp(-aw) =$
$\frac{1}{a}(\frac{b}{a})^{\frac{1}{2}} \exp(-ac/b)\{\frac{\sqrt{\pi}}{2}\,H[\frac{a}{b}(c-bw)]^{1/2} - [\frac{a}{b}(c-bw)]^{1/2}\exp[]^{1/2}\,\frac{a}{b}(c-bw)]\}$

3. $\int dw \exp(-aw)\,[bw+c]^{-1/2} = \sqrt{\frac{\pi}{ba}}\exp(ac/b)\,\mathrm{erf}[\frac{a}{b}(bw+c)]^{1/2}$

4. $\int dw \exp(-aw)\,[c-bw]^{-1/2} = -\sqrt{\frac{\pi}{ba}}\exp(-ac/b)\,H[\frac{a}{b}(c-bw)]^{1/2}$

5. $\int dw\, w \exp(-aw)\,[bw+c]^{-1/2} = \frac{\exp(\frac{ac}{b})}{ab} \times$
$\{(\frac{1}{2} - \frac{ac}{b})\,(\frac{b}{a})^{1/2}\,\mathrm{erf}[\frac{a}{b}(bw+c)]^{1/2} - (bw+c)^{1/2}\exp(-\frac{a}{b}(bw+c))\}$

6. $\int dw \exp(-aw^2) = \frac{1}{2}\sqrt{\frac{\pi}{a}}\,\mathrm{erf}[aw]^{1/2}$

7. $\int dw \exp(bw^2) = \frac{1}{2}\sqrt{\frac{\pi}{b}}\,H[bw]^{1/2}$

8. $\int dw\,\mathrm{erf}(bw+c) = \frac{1}{b}\{(bw+c)\,\mathrm{erf}(bw+c) - \frac{1}{\sqrt{\pi}}\exp[-(bw+c)^2]\}$

9. $\int dw\, H(bw+c) = \frac{1}{b}\{(bw+c)\,H(bw+c) - \frac{1}{\sqrt{\pi}}\exp\,(bw+c)^2\}$

10. $\int dw\,\mathrm{erf}[bw+c]^{1/2} =$
$\frac{1}{b}\{(bw + c - \frac{1}{2})\,\mathrm{erf}[bw+c]^{1/2} + [\frac{bw+c}{\pi}]^{1/2}\exp[-(bw+c)]\}$

11. $\int dw\ H[bw+c]^{1/2} =$

$$\frac{1}{b}\{(bw + c + \frac{1}{2})\ H[bw+c]^{1/2} + [\frac{bw+c}{\pi}]^{1/2} \exp[-(bw+c)]\}$$

12. $\int dw\ \mathrm{erf}[bw+c]^{1/2} \exp(-aw) = -\frac{1}{a} \exp(-aw)\ \mathrm{erf}[bw+c]^{1/2}$

$$+ \frac{1}{a} \exp(\frac{ac}{b})\ (\frac{b}{b+a})^{1/2}\ \mathrm{erf}[\frac{b+a}{b}(bw+c)]^{1/2} \qquad (\text{if } \frac{a+b}{b} > 0)$$

$$+ \frac{1}{a} \exp(\frac{ac}{b})\ (\frac{-b}{b+a})^{1/2}\ \mathrm{erf}[-\frac{b+a}{b}(bw+c)]^{1/2} \qquad (\text{if } \frac{a+b}{b} < 0)$$

13. $\int dw\ \mathrm{erf}[c-bw]^{1/2} \exp(-aw) = -\frac{1}{a} \exp(-aw)\ \mathrm{erf}[c-bw]^{1/2}$

$$+ \frac{1}{a}\ (\frac{b}{a-b})^{1/2} \exp(-\frac{ac}{b})\ H[\frac{a-b}{b}(c-bw)]^{1/2} \qquad (\text{if } a > b)$$

$$+ \frac{1}{a}\ (\frac{b}{b-a})^{1/2} \exp(-\frac{ac}{b})\ \mathrm{erf}[\frac{b-a}{b}(c-bw)]^{1/2} \qquad (\text{if } a < b)$$

$$+ \frac{2}{a} \exp(-c)\ [\frac{c-bw}{\pi}]^{1/2} \qquad (\text{if } a = b)$$

14. $\int dw\ H[bw+c]^{1/2} \exp(-aw) = -\frac{1}{a} \exp(-aw)\ H[bw+c]^{1/2}$

$$+ \frac{1}{a} \exp(\frac{ac}{b})\ (\frac{b}{a-b})^{1/2}\ \mathrm{erf}[\frac{a-b}{b}(bw+c)]^{1/2} \qquad (\text{if } a > b > 0)$$

$$+ \frac{1}{a} \exp(\frac{ac}{b})\ (\frac{-b}{b-a})^{1/2}\ \mathrm{erf}[\frac{a-b}{b}(bw+c)]^{1/2} \qquad (\text{if } a > 0 > b)$$

15. $\int dw\ w \exp(-aw)\ \mathrm{erf}[bw]^{1/2} = \frac{1}{a}\{-(w + \frac{1}{a})\exp(-aw)\ \mathrm{erf}[bw]^{\frac{1}{2}}$

$$+ (\frac{1}{a} + \frac{1}{2(a+b)})\ (\frac{b}{a+b})^{\frac{1}{2}}\ \mathrm{erf}[(a+b)w]^{\frac{1}{2}} - \frac{1}{a+b}\ (\frac{bw}{\pi})^{1/2} \exp[-(a+b)w]\}$$

16. $\int dw\ w \exp(-w)\ \mathrm{erf}[bw+c]^{1/2} =$

$$-(1+w) \exp(-w)\ \mathrm{erf}[bw+c]^{1/2}$$

$$+ (\frac{b}{b+1})^{1/2} \exp(\frac{c}{b})\ [1 + \frac{1}{2(b+1)} - \frac{c}{b}]\ \mathrm{erf}[\frac{b+1}{b}(bw+c)]^{1/2}$$

$$- \frac{\exp(-c)}{b+1}\ (\frac{bw+c}{\pi})^{1/2} \exp[-(b+1)w]$$

17. $\int dw\ w^{-1/2}\ \mathrm{erf}[aw]^{1/2} = 2\sqrt{w}\ \mathrm{erf}[aw]^{1/2} + \frac{2}{\sqrt{(a\pi)}}\ e^{-aw}$

18. $\int dw\ w^{-3/2} \exp(-aw) = 2(\frac{\pi}{a})^{1/2}\ \mathrm{erf}[aw]^{1/2} - \frac{2}{\sqrt{\pi}}\ e^{-aw}$

APPENDIX B

Effect of resonance zone potential dip on ECRH rate

One of the results of section 7.3 for a parabolic mirror is that the power absorption depends only on the resonance zone density:

$$(B1)\quad P = \frac{\pi e E^2}{2B'}\, n\, A_r$$

where A_r is the resonance zone area, E is the local high frequency electric field, and B' is the local gradient of the magnetic field.

The accumulation of turning points as a result of ECRH cause the power absorption to increase as n_{res}/n_o, the resonance zone-to-midplane density ratio, increases. The heating rate per particle will also be affected by the occurrence of a potential dip near resonance. Consider a potential profile which is zero throughout a parabolic mirror, except in a region of width $2\Delta w$, centered on the resonance zone position z_{res}, where the potential is $q\phi$. The mean absorption per particle per resonance zone passage is still the same as before, when expressed in resonance zone velocity space variables:

$$(B2)\quad \Delta W = \frac{\pi e E^2}{4 B' v_\parallel}$$

However, the time per resonance zone transit is changed to

$$(B3)\quad t_q = \frac{1}{v_\perp}\left(\frac{r}{\beta}\right)^{\frac{1}{2}} \left\{\frac{\pi}{2} + \sin^{-1}\left[\frac{\beta(z_r-\Delta w)^2 v_\perp^2}{r\left(v_\parallel^2 + \frac{2q\phi}{m}\right) + (r-1)v_\perp^2}\right]^{1/2} - \sin^{-1}\left[\frac{\beta(z_r-\Delta w)^2 v_\perp^2}{r v_\parallel^2 + (r-1)v_\perp^2}\right]^{1/2} + \sin^{-1}\left[\frac{\beta(z_r+\Delta w)^2 v_\perp^2}{r v_\parallel^2 + (r-1)v_\perp^2}\right]^{1/2} - \sin^{-1}\left[\frac{\beta(z_r+\Delta w)^2 v_\perp^2}{r\left(v_\parallel^2 + \frac{2q\phi}{m}\right) + (r-1)v_\perp^2}\right]^{1/2}\right\}$$

when the turning point z_t is greater than $z_r+\Delta w$, or $(v_\parallel^2/v_\perp^2) > \frac{\beta}{r}(2\Delta w\, z_r + (\Delta w)^2)$. When $z_t \le z_r + \Delta w$, or $(v_\parallel^2/v_\perp^2) < \frac{\beta}{r}(2\Delta w\, z_r + (\Delta w)^2)$ the quarter bounce time is

$$(B4)\quad t_q = \frac{1}{v_\perp}\left(\frac{r}{\beta}\right)^{\frac{1}{2}} \left\{\frac{\pi}{2} + \sin^{-1}\left[\frac{\beta(z_r-\Delta w)^2 v_\perp^2}{r\left(v_\parallel^2 + \frac{2q\phi}{m}\right) + (r-1)v_\perp^2}\right]^{1/2} - \sin^{-1}\left[\frac{\beta(z_r-\Delta w)^2 v_\perp^2}{r v_\parallel^2 + (r-1)v_\perp^2}\right]^{1/2}\right\}$$

With the definitions $\varepsilon \equiv \frac{\Delta W}{z_r}$ and $v_p^2 \equiv \frac{2q\phi}{m}$, (B3) and (B4) become

$$(B5)\quad t_q = \frac{1}{v_\perp}\left(\frac{r}{\beta}\right)^{\frac{1}{2}}\left\{\frac{\pi}{2} + \sin^{-1}\left[\frac{(1-\varepsilon)^2}{1+\frac{r}{r-1}\frac{v_\parallel^2+v_p^2}{v_\perp^2}}\right]^{1/2} - \sin^{-1}\left[\frac{(1-\varepsilon)^2}{1+\frac{r}{r-1}\frac{v_\parallel^2}{v_\perp^2}}\right]^{1/2} - \sin^{-1}\left[\frac{(1+\varepsilon)^2}{1+\frac{r}{r-1}\frac{v_\parallel^2}{v_\perp^2}}\right]^{1/2} + \sin^{-1}\left[\frac{(1+\varepsilon)^2}{1+\frac{r}{r-1}\frac{v_\parallel^2+v_p^2}{v_\perp^2}}\right]^{1/2}\right\}$$

$$\left(\frac{v_\parallel^2}{v_\perp^2} > \frac{r-1}{r}(2\varepsilon+\varepsilon^2)\right)$$

$$(B6)\quad t_q = \frac{1}{v_\perp}\left(\frac{r}{\beta}\right)^{\frac{1}{2}}\left\{\frac{\pi}{2} + \sin^{-1}\left[\frac{(1-\varepsilon)^2}{1+\frac{r}{r-1}\frac{v_\parallel^2+v_p^2}{v_\perp^2}}\right]^{1/2} - \sin^{-1}\left[\frac{(1-\varepsilon)^2}{1+\frac{r}{r-1}\frac{v_\parallel^2}{v_\perp^2}}\right]^{1/2}\right\}$$

$$\left(\frac{v_\parallel^2}{v_\perp^2} < \frac{r-1}{r}(2\varepsilon+\varepsilon^2)\right)$$

The heating rate for a particular element of resonance zone velocity space is calculated from

$$(B7)\qquad \bar{\dot{W}} = \bar{\Delta W}/t_q$$

The ratio of the electron cyclotron heating rate with the case of a potential dip near resonance, to the case without a dip, is given in Table B.1 for a Maxwellian distribution. For ECRH-perturbed distributions the ratios will be somewhat closer to unity, depending on the degree to which $\frac{\langle v_\perp^2\rangle}{\langle v_\parallel^2\rangle}$ is increased.

The findings of relevance are that:

(1) For small potential dips ($\frac{e\phi}{kT_e} < .5$), the change in heating rate is negligible, differing from unity by only a few per cent.

(2) The optimum relative width for heating enhancement is $\varepsilon \sim .05$. (In the present experiment $\varepsilon \sim .03$.)

Table B.1

Ratio of mean heating rates with a local resonance potential dip to that without a dip, for a Maxwellian plasma in a parabolic mirror

r = 1.1

Potential Dip / Electron Temperature

w / Zres	0.010	0.020	0.050	0.100	0.200	0.500	1.000	2.000	5.000
0.005	0.997	0.996	0.994	0.993	0.992	0.991	0.990	0.989	0.989
0.010	0.995	0.992	0.989	0.987	0.985	0.984	0.984	0.985	0.987
0.020	0.992	0.990	0.988	0.989	0.994	1.007	1.022	1.043	1.075
0.050	0.996	0.998	1.007	1.024	1.052	1.107	1.162	1.223	1.304
0.100	1.000	1.005	1.022	1.047	1.086	1.157	1.221	1.287	1.370
0.200	1.000	1.005	1.022	1.046	1.081	1.144	1.197	1.249	1.310
0.500	1.005	1.009	1.020	1.035	1.054	1.085	1.109	1.131	1.155

r = 2.0

Potential Dip / Electron Temperature

w / Zres	0.010	0.020	0.050	0.100	0.200	0.500	1.000	2.000	5.000
0.005	0.996	0.995	0.996	0.998	1.002	1.015	1.033	1.061	1.116
0.010	1.000	1.002	1.009	1.020	1.040	1.087	1.146	1.231	1.366
0.020	1.000	1.002	1.011	1.027	1.054	1.119	1.197	1.305	1.494
0.050	1.004	1.009	1.023	1.046	1.086	1.175	1.276	1.408	1.620
0.100	1.003	1.008	1.021	1.043	1.080	1.164	1.257	1.375	1.556
0.200	1.004	1.008	1.020	1.038	1.070	1.140	1.215	1.308	1.442
0.500	1.002	1.004	1.011	1.020	1.036	1.070	1.106	1.148	1.204

r = 5.0

Potential Dip / Electron Temperature

w / Zres	0.010	0.020	0.050	0.100	0.200	0.500	1.000	2.000	5.000
0.005	0.998	0.998	1.000	1.005	1.015	1.039	1.070	1.119	1.218
0.010	1.001	1.004	1.012	1.025	1.048	1.102	1.171	1.270	1.460
0.020	1.002	1.006	1.016	1.033	1.063	1.133	1.220	1.342	1.564
0.050	1.004	1.008	1.022	1.042	1.078	1.161	1.261	1.397	1.627
0.100	1.004	1.008	1.020	1.039	1.072	1.150	1.241	1.361	1.557
0.200	1.003	1.006	1.016	1.031	1.058	1.119	1.190	1.282	1.426
0.500	1.002	1.004	1.010	1.018	1.032	1.063	1.097	1.140	1.203

Appendix C

Relationship between turning point distribution and density

Since the density buildup at the resonance zone is caused by an ECRH induced accumulation of turning points, it helps to understand the relation between the density of turning points per unit volume and the density of particles per unit volume. In section I the turning point distribution is derived for a parabolic mirror. In section II the density resulting from a Maxwellian distribution of particles within a given turning point span is derived, and in section III this "partial Maxwellian" density is used to check the accuracy of resonance zone density programs used in Chapter 7.

I. Derivation of turning point distribution.

Let the number of particles in a parabolic mirror turning within dz' of position z' across a flux tube of area A' be $dN(z') = g(z')\ A'\ dz'$. The "turning point density", $g(z)$, has the same units as $n(z)$. The relation between $n(z)$ and $g(z)$ is now found from the properties of idealized sloshing distributions (see Appendix D). Let $dn_o(z')$ be the number density at the midplane due to particles turning near z'. Then at other positions the density is

$$(C1) \quad dn(z) = dn_o(z') \frac{B}{B_o} \left(\frac{B(z')-B_o}{B(z')-B}\right)^{1/2}$$

Integrating over the volume of magnetic flux tube accessible to these particles gives the total number as

$$(C2) \quad dN(z') = \int_{-z'}^{z'} A \frac{B(z')}{B} dn(z')\, dz$$

$$= 2\, dn_o(z') \frac{A\, B(z')}{B} \left(\frac{B(z')}{B_o} - 1\right)^{1/2} \frac{1}{\sqrt{\beta}} \int_0^{z'} dz\, [z'^{-2} - z^2]^{-1/2}$$

$$= \pi A \frac{B(z')}{B} z'\, dn_o(z')$$

From (C2) and the definition of $g(z')$ one concludes

$$(C3) \quad dn_o(z') = \frac{1}{\pi z'} \frac{B}{B(z')} g(z')\, dz'$$

The density at a given z is a summation of contributions from turning points of all values $z' > z$:

$$n(z) = \int_z^\infty \frac{B}{B_o} \left(\frac{B(z')-B_o}{B(z')-B}\right)^{1/2} \frac{1}{\pi z'} \frac{B_o}{B(z')} g(z')\, dz'$$

$$\text{or (C4)} \quad n(z) = \frac{1 + \beta z^2}{\pi} \int_z^\infty \frac{dz'\, g(z')}{(1 + \beta z'^{-2}) \sqrt{[z'^{-2} - z^2]}}$$

For a Dirac-δ function turning point distribution, (C4) reduces to (C1). For a Maxwellian in a parabolic mirror the turning point density is calculated to be

$$(C5) \quad g_m(z) = \pi n_o \left(\frac{\beta z^2}{1 + \beta z^2}\right)^{3/2}$$

Substitution of (C5) into (C4) yields $n(z) = n_o$. The constant density is a characteristic of isotropic distributions in general.[1]

Haste and Lazar[2] pointed out that $n(z)$ and $g(z)$ form an Abel transform pair. This allows the expression of $g(z)$ in terms of $n(z)$. First, (C4) is re-written as

$$(C6) \quad \frac{\pi}{I} \frac{B_o}{B(z)} n(z) = \int_a^t \frac{U(t)\, dt}{(x - t)^{1/2}}$$

where $I \equiv \sqrt{(-1)}$, $t \equiv z'^{-2}$, $a = \infty$, $x = z^{-2}$, and

$$(C7) \quad U(t) \equiv \frac{g(\sqrt{t})}{2(1+\beta t)\sqrt{t}}$$

From the properties of the Abel transform[3],

if $\quad h(x) = \int_a^x \frac{U(t)}{(x-t)^q} dt \qquad$ with $0 < q < 1$,

$$\text{then} \quad U(t) = \frac{\sin q\pi}{\pi} \frac{d}{dt} \int_a^t \frac{h(x)}{(t-x)^{1-q}} dx$$

For (C6) and (C7) this means that

$$(C9) \quad g(z') = -(1+\beta z^2) \frac{d}{dz} \int_{z'}^\infty n(z) \frac{B_o}{B(z)} [z^2 - z'^{-2}]^{-1/2}$$

This is the desired expression for the turning points per unit

volume in a parabolic mirror. It is interesting that that with a constant density, (C9) yields (C5), so that the latter formula holds for all isotropic distrbutions, not just the Maxwellian.

II. Density from a partial Maxwellian with a given turning point span.

Consider a Maxwellian velocity distribution of particles at the midplane of a magnetic mirror. Neglecting electrostatic potential, the fraction of midplane particles which have turning points z_t such that $B(z_t) < B_L$ is

$$(C10) \quad n(z) = n_* \left(1 - \frac{B(z)}{B_L}\right)^{1/2}$$

where n_* is the density of the complete Maxwellian. Now suppose that all particles are deleted except those with turning points between z_1 and z_2, where the magnetic fields are B_1 and B_2, $(B_2 > B_1)$. Then for $B_o < B < B_1$,

$$(C11) \quad n = n_o \frac{\left(1 - \frac{B}{B_2}\right)^{1/2} - \left(1 - \frac{B}{B_1}\right)^{1/2}}{\left(1 - \frac{B_o}{B_2}\right)^{1/2} - \left(1 - \frac{B_o}{B_1}\right)^{1/2}}$$

For $B_1 < B < B_2$,

$$(C12) \quad n = n_o \frac{\left(1 - \frac{B}{B_2}\right)^{1/2}}{\left(1 - \frac{B_o}{B_2}\right)^{1/2} - \left(1 - \frac{B_o}{B_1}\right)^{1/2}}$$

In (C8) and (C9) n_o is the midplane density of those particles in the allowed turning point span (z_1, z_2). These equations hold for an arbitrary magnetic mirror, but frequently the magnetic field can be approximated with the parabolic model:

$$(C13) \quad B(z) = B_o (1 + \beta z^2)$$

Then (C11) and (C12) reduce to (C14) and (C15), respectively:

$$(C14) \quad n = n_o \frac{(z_2^2 - z^2)^{1/2} - (z_1^2 - z^2)^{1/2} \sqrt{\left(\frac{r_2}{r_1}\right)}}{z_2 - z_1 \sqrt{\left(\frac{r_2}{r_1}\right)}} \qquad (0 < z < z_1)$$

$$(C15) \quad n = n_o \frac{(z_2^2 - z^2)^{1/2}}{z_2 - z_1 \sqrt{\left(\frac{r_2}{r_1}\right)}} \qquad (z_1 < z < z_2)$$

Here $r_2 \equiv 1 + \beta z_2^2$ and $r_1 \equiv 1 + \beta z_1^2$, the mirror ratios at the high and low ends of the turning point span.

Figure C.1 shows the density profile resulting from (C14) and (C15), for the turning point span centered on the point $z_r = 50$ cm, at which $r \equiv \frac{B(z_r)}{B_o} = 5$ is assumed. The values are chosen to be close to the resonance zone values in the DC Machine, where an accumulation of turning points exists. The density peaks at z_1.

Figures C.2 and C.3 show the dependence of the density FWHM and $\frac{\text{peak density}}{\text{midplane density}}$, respectively, as a function of turning point span Δz. The essential point is that the density FWHM is always close to Δz. A good fit for the range of parameters tested (1 cm $\leq \Delta z \leq$ 20 cm; r = 1.2 to 5) is

(C16) $\frac{\text{FWHM}}{\Delta z} =$

$1.312 - 10^{-2}[1.59 + .857\ \ell n(r-1)]\Delta z + 10^{-4}[1 + 3.83\ \ell n\ r]\Delta z^2$

For resonance zone density widths of a few centimeters, FWHM $\sim$ $1.3\Delta z$ is a very good estimate.

III. Test of finite grid method by comparison of density with partial Maxwellian model

The precision of the finite grid procedure (see Appendix E) can be compared with the exact values of the partial Maxwellian by filling in value f_{ij} with the Maxwellian values for the allowed turning point span. Table C.1 shows the values obtained for r = 5, and a central turning point of z_{res}=.5m, for three finite grid programs. A 30 x 30 grid of midplane velocity space with bin sides of $\Delta v = \frac{1}{10}\left(\frac{2kT_e}{m}\right)^{1/2}$ is seen to be too coarse to reveal resonance zone detail on a scale of less than ~14 cm, for the parameters of relevance here. By making a finer grid with $\Delta v = \frac{1}{20}\left(\frac{2kT_e}{m}\right)^{1/2}$, structure with FWHM down to ~11 cm can be reproduced with relative fidelity. Narrower features can be

modeled, but these are broadened by a factor of 2-3 at density FWHM's of ~1 cm. By taking a velocity space grid at the resonance zone itself, resolution of $\leq$ 1 cm is possible. In this case the predicted width is 1/2 to 2/3 of the actual value.

Table C.1

Comparison of finite grid program density FWHM with exact partial Maxwellian values for given turning point ranges

turning point span, Δz	30x30 grid at midplane	60x60 grid at midplane	60x60 grid at z_{res}	Partial Maxwellian
1	14.03	3.41	.68	1.281
2	14.03	5.59	1.25	2.505
4	14.02	7.86	2.69	3.671
8	13.80	10.73	5.40	9.086
10	14.34	12.03		11.095
15	17.27	15.81	10.32	15.897
20	20.24			20.504

Notes

1. All values are in centimeters.
2. Turning point span Δz is centered on z_{res} = 50 cm., where B/B_o = 5.
3. Partial Maxwellian used for non-resonance passing particles to supplement 60 x 60 grid at z_{res}.

Figure C.1
Density profiles of partial Maxwellian distributions with given turning point spans.

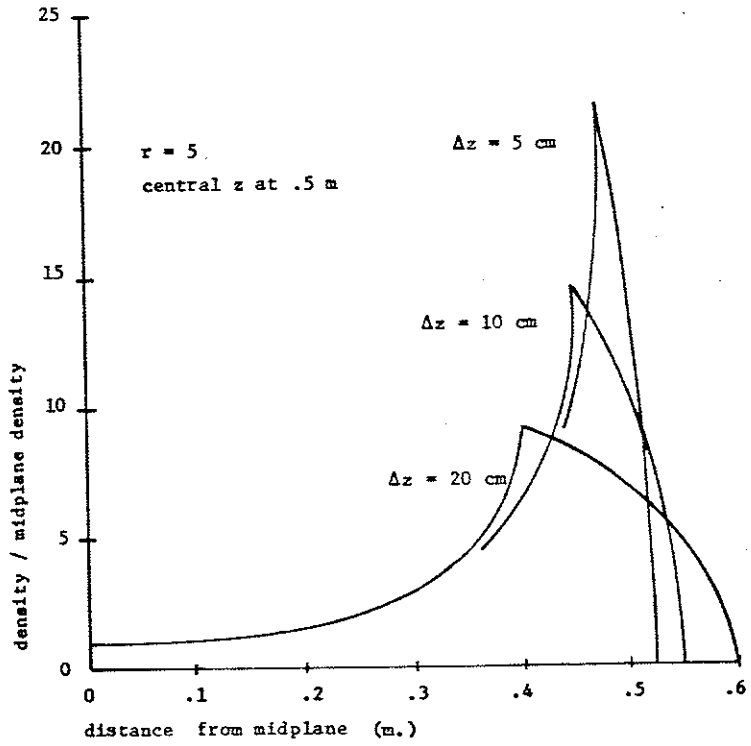

Figure C.2
Ratio of density FWHM to turning point span Δz vs. Δz for various r values.

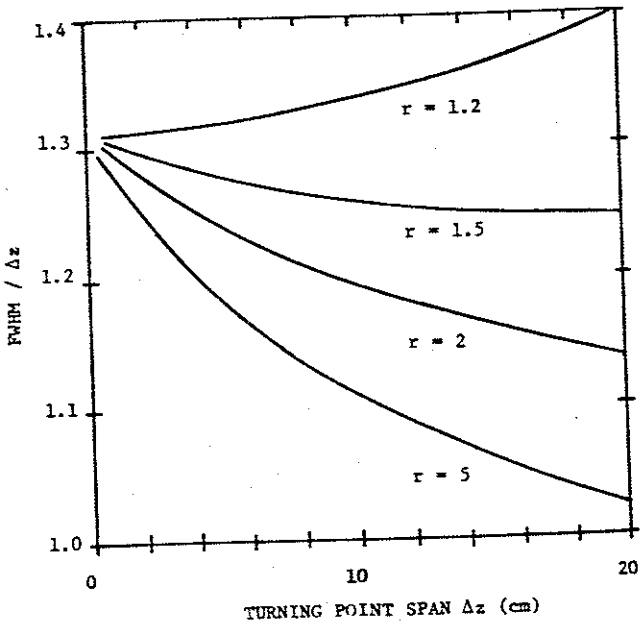

Figure C.3
Ratio of peak density to midplane density vs. turning point span.

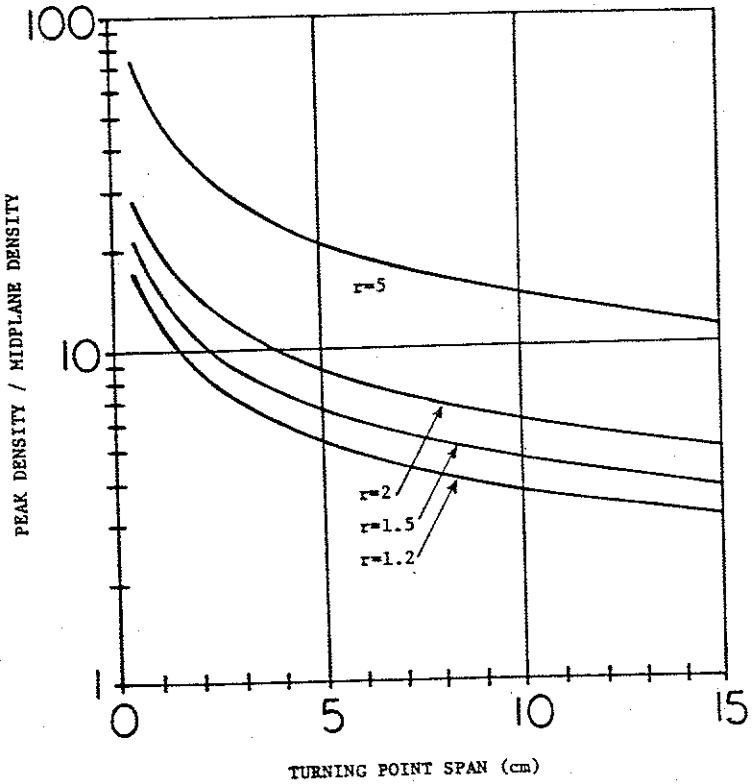

REFERENCES FOR APPENDIX C

[1]J. C. Sprott, PLP 519, (June, 1973).

[2]G. R. Haste and N. H. Lazar, Phys. Fluids 16, 683 (1973).

[3]D. H. Menzel (ed.), Fundamental Formulas of Physics, (Dover: New York, 1960) p. 95.

Appendix D

Characteristics of idealized sloshing particle distributions.

Since a large fraction of particles can have turning points near the resonance zone, it can be useful to estimate density and mean energy profiles from the idealized case of a distribution of particles with turning points exactly at resonance.

The profiles of density n, mean squared parallel speed $\langle v_\parallel^2 \rangle$, and mean squared perpendicular speed $\langle v_\perp^2 \rangle$ are given here for distributions functions consisting entirely of particles which have turning points at z_R. Only final results are given here. More detailed derivations are given in PLP 839.[1] The local, midplane, and sloshing point magnetic fields are denoted by B, B_o, and B_R, respectively. The normalized electostatic potentials are given by $\eta \equiv \frac{q(\phi-\phi_o)}{kT}$ and $\eta_R = \frac{q(\phi_R-\phi_o)}{kT}$ at the local and sloshing position, respectively.

Part I deals with the case of the potential well (from the perspective of midplane). Part II covers the potential hill case. Part III addresses miscellaneous issues such as the simplification that results when η is a linear function of B, the number of partilces in a sloshing system, and the ionization rate of a sloshing distribution.

I. $\eta_R > \eta > 0$

Assuming a Maxwellian dependence on energy (type 1 distribution):

$$(D1)\quad n = n_o \exp[(\frac{B}{B_R-B} - \frac{B_o}{B_R-B_o})\eta_R - \frac{B_R}{B_R-B}\eta] \frac{B}{B_o} (\frac{B_R-B_o}{B_R-B})^{1/2} \times \frac{1 - \mathrm{erf}[B_R \frac{\eta_R-\eta}{B_R-B}]^{1/2}}{1 - \mathrm{erf}[B_R \frac{\eta_R}{B_R-B_o}]^{1/2}}$$

$$(D2)\quad \langle v_\perp^2\rangle = \frac{kT}{m}\frac{B}{B_R}\{(1 + 2B_R\frac{\eta_R-\eta}{B_R-B}) + \frac{2}{\sqrt{\pi}}(B_R\frac{\eta_R-\eta}{B_R-B})^{\frac{1}{2}}\frac{\exp(-B_R\frac{\eta_R-\eta}{B_R-B})}{1-\mathrm{erf}[B_R\frac{\eta_R-\eta}{B_R-B}]^{1/2}}\}$$

$$(D3)\quad \langle v_\parallel^2\rangle = \frac{kT}{m}\frac{B_R-B}{B_R}\{1 + \frac{2}{\sqrt{\pi}}(B_R\frac{\eta_R-\eta}{B_R-B})^{1/2}\frac{\exp(-B_R\frac{\eta_R-\eta}{B_R-B})}{1-\mathrm{erf}[B_R\frac{\eta_R-\eta}{B_R-B}]^{1/2}}\}$$

With the assumption that just enough perpendicular energy given to an initially Maxwellian distribution at midplane to bring the turning point to z_R, and with deletion of particles with turning point $< z_R$, one obtains the type 2 distribution:

$$(D4)\quad n = n_o \frac{B}{B_o}(\frac{B_R-B_o}{B_R-B})^{1/2}\exp[-(\frac{B_R-B_o}{B_R-B})\eta + \frac{B-B_o}{B_R-B}\eta_R\}] \times \frac{1-\mathrm{erf}[\frac{B_R-B_o}{B_R-B}(\eta_R-\eta)]^{1/2} - (1-\frac{B_o}{B_R})^{1/2}\exp(B_o\frac{\eta_R-\eta}{B_R-B})\ (1-\mathrm{erf}[B_R\frac{\eta_R-\eta}{B_R-B}]^{1/2})}{1-\mathrm{erf}[\eta_R]^{1/2} - (1-\frac{B_o}{B_R})^{1/2}\exp(B_o\frac{\eta_R}{B_R-B_o})\ (1-\mathrm{erf}[B_R\frac{\eta_R}{B_R-B_o}]^{1/2})}$$

$$(D5)\quad \langle v_\perp^2\rangle = \frac{2kT}{m}\frac{B}{B_R-B_o}\{\frac{1}{2}(1-\frac{B_o}{B_R}) + \frac{B_R-B_o}{B_R-B}(\eta-\eta_R) + \frac{1}{2}\frac{B_o}{B_R}(1-\mathrm{erf}[\frac{B_R-B_o}{B_R-B}(\eta_R-\eta)]^{1/2} + \frac{2}{\sqrt{\pi}}(\frac{B_R-B_o}{B_R-B}(\eta_R-\eta))^{1/2}\exp(\frac{B_R-B_o}{B_R-B}(\eta_R-\eta)))\}$$
$$\overline{1-\mathrm{erf}[\frac{B_R-B_o}{B_R-B}(\eta_R-\eta)]^{1/2} - (1-\frac{B_o}{B_R})^{1/2}\exp(B_o\frac{\eta_R}{B_R-B})\ (1-\mathrm{erf}[B_R\frac{\eta_R}{B_R-B}]^{1/2})}$$

$$(D6)\quad \langle v_\parallel^2\rangle = \frac{kT}{m}\frac{B_R-B}{B_R-B_o}\{1 + \frac{B_o}{B_R}(\frac{B_R-B_o}{B_R})^{1/2}\exp[B_o\frac{\eta_R-\eta}{B_R-B}] \times (1 - \mathrm{erf}[B_R\frac{\eta_R-\eta}{B_R-B}]^{1/2} + \frac{2}{\sqrt{\pi}}(B_R\frac{\eta_R-\eta}{B_R-B})^{1/2}\exp(-B_R\frac{\eta_R-\eta}{B_R-B}))$$
$$\overline{1-\mathrm{erf}[\frac{B_R-B_o}{B_R-B}(\eta_R-\eta)]^{1/2} - (1-\frac{B_o}{B_R})^{1/2}\exp(B_o\frac{\eta_R-\eta}{B_R-B})\ (1-\mathrm{erf}[B_R\frac{\eta_R-\eta}{B_R-B}]^{1/2})}\}$$

The assumption that all particles have total energy E forms the basis of the type 3 distribution:

$$(D7)\quad n = n_o\frac{B}{B_o}\frac{\frac{B_o}{B_R}q\phi_R + (1-\frac{B_o}{B_R})E}{\frac{B}{B_R}q\phi_R - q\phi + (1-\frac{B}{B_R})E}$$

$$(D8)\quad \langle v_\perp^2\rangle = v_\perp^2 = \frac{2}{m}\frac{B}{B_R}(E - q\phi_R)$$

(D9) $\langle v_\parallel^2 \rangle = v_\parallel^2 = \frac{2}{m}\left[\left(1-\frac{B}{B_R}\right)E + \frac{B}{B_R}q\Phi_R - q\Phi\right]$

II. $\eta_R < \eta < 0$.

Type 1 distribution:

(D10) $$n = n_o \frac{B}{B_R}\left(\frac{B_R-B_o}{B_R-B}\right)^{1/2} \exp\left[\left(\frac{B}{B_R-B} - \frac{B_o}{B_R-B_o}\right)\eta_R - \frac{B_R}{B_R-B}\eta\right]$$

(D11) $$\langle v_\parallel^2 \rangle = \frac{kT}{m}\frac{B}{B_R}\left(1 - 2B_R\left(\frac{\eta_R-\eta}{B_R-B}\right)\right)$$

(D12) $$\langle v_\parallel^2 \rangle = \frac{kT}{m}\frac{B_R-B}{B_R}$$

Type 2 distribution:

(D13) $$n = n_o \frac{B}{B_o}\left(\frac{B_R-B_o}{B_R-B}\right)^{1/2} \exp\left[\left(\frac{B}{B_R-B} - \frac{B_o}{B_R-B_o}\right)\eta_R - \frac{B_o}{B_R-B}\eta\right]$$

(D14) $$\langle v_\parallel^2 \rangle = \frac{kT}{m}\frac{B}{B_R-B_o}\left\{\frac{B_R-B_o}{B_R-B}(\eta-\eta_R) + \frac{1-\left(\frac{B_R-B_o}{B_R}\right)^{3/2}}{1-\left(\frac{B_R-B_o}{B_R}\right)^{1/2}}\right\}$$

(D15) $$\langle v_\parallel^2 \rangle = \frac{kT}{m}\frac{B_R-B}{B_R-B_o}\frac{1-\left(\frac{B_R-B_o}{B_R}\right)^{3/2}}{1-\left(\frac{B_R-B_o}{B_R}\right)^{1/2}}$$

Type 3 distribution: same as in (D7), (D8), and (D10).

III. Miscellaneous issues.

III.1 Linear simplification.

In an early square well model of a mirror, BenDaniel[2] found that the electrostatic potential was almost a linear function of magnetic field B. Geller, et. al.[3] found that a linear dependence of η on B fit the data from the Pleiade device. If the electrostatic potential is truly a linear function of B, then all of the preceding density equations, for either $\eta_R > 0$ or $\eta_o < 0$, reduce to:

(D16) $$n = n_o \frac{B}{B_o}\left(\frac{B_R-B_o}{B_R-B}\right)^{1/2}$$

III.2 Number of particles in a sloshing system.

By integrating (D16) between resonance zones in a parabolic mirror, one finds the total number of sloshing particles crossing midplane area A_o and with midplane density n_o:

(D17) $$N = \pi\, n_o\, A_o\, z_R$$

III.3 Ionization rate from sloshing electrons

In a parabolic mirror the rate of increase of system particles by ionization is

(D18) $$\dot{N} = \pi\, n_o\, n_g \langle\sigma v\rangle_{ion}\, A_o\, z_r$$

where $\langle\sigma v\rangle$ = the Maxwellian rate coefficient for a type 1 distribution, $\sigma(v_o)\ v_o$ for a type 3 distribution, and for a type 2 distribution one has

$$(D19)\quad \langle\sigma v\rangle = n_o(r-1)\left(\frac{2kT}{rm}\right)^{1/2} \sum_j a_j\,(kT)^j \int_0^\infty dx\, x^{j+1/2}\, \mathrm{erf}\left[\frac{x}{r}\right]^{1/2} \exp\left[-\frac{r-1}{r}x\right]$$

where the ionization cross section is given by

$$(D19)\quad \sigma(E) = \sum_j a_j\, E^j$$

References for Appendix D

[1] P. K. Smith, PLP 839, (November, 1980).

[2] D. J. BenDaniel, Plas. Phys. 3, 235 (1961).

[3] R. Geller, et. al., J. Plas. Phys. 12, part 3, 467 (1974).

Appendix E

Calculation of profile variables with the finite grid approximation

This section is included so that future researchers might be spared the expense of time involved in re-derivation of the following expressions. The form of the equations in this section has been selected so that programmers will have no difficulty in vectorization of the corresponding computer expressions. This may reduce computational costs by up to a factor of seven.[1]

Non-Maxwellian plasmas may require a numerical treatment for solution of the distribution function. For the purpose of obtaining an approximation to $f(v_\parallel, v_\perp)$ the velocity space can be divided into an N x N square of bins, Δv on a side, extending from the $v_\parallel = 0$ and $v_\perp = 0$ axes up to $N\Delta v$. Symmetry of $f(v_\parallel, v_\perp)$ in $\pm v_\parallel$ is assumed so that that only positive $v_\parallel$ and $v_\perp$ need be covered. Inside the (i,j)-th bin, centered on $v_\parallel = v_i$, $v_\perp = v_j$, ($1 \le i \le N$; $1 \le j \le N$), the distribution function value is taken to be a constant, f_{ij}.

One way of obtaining values of such profile values as density, parallel energy per unit volume is to add the bin's contribution only if particles at the center of the bin have a turning point $z_T > z$.

With this method,

$$(E1)\quad n(z) = 4\pi\,(\Delta v)^2\,\frac{B}{B_o}\times$$
$$\sum_{i,j} f_{ij}\,v_i\,v_j\,\left[v_i^2-\left(\frac{B}{B_o}-1\right)v_j^2-\frac{2q}{m}(\phi-\phi_o)\right]^{-1/2}$$

$$(E2)\quad \langle v_\parallel(z)\rangle = \frac{4\pi}{n(z)}\,(\Delta v)^2\,\frac{B}{B_o}\sum_{i,j} f_{ij}\,v_i\,v_j$$

$$(E3)\quad \langle v_\parallel^2(z)\rangle = \frac{4\pi}{n(z)}\,(\Delta v)^2\,\frac{B}{B_o}\times$$
$$\sum_{i,j} f_{ij}\,v_i\,v_j\,\left[v_i^2-\left(\frac{B}{B_o}-1\right)v_j^2-\frac{2q}{m}(\phi-\phi_o)\right]^{1/2}$$

$$(E4)\quad \langle v_\perp^2(z)\rangle = \frac{4\pi}{n(z)}\,(\Delta v)^2\,\left(\frac{B}{B_o}\right)^2\times$$
$$\sum_{i,j} f_{ij}\,v_i\,v_j^3\,\left[v_i^2-\left(\frac{B}{B_o}-1\right)v_j^2-\frac{2q}{m}(\phi-\phi_o)\right]^{-1/2}$$

Equations (E1) through (E4) were used in early versions of a plasma profile determination program, but the resulting profiles were spiky. This is because the contribution of a bin changes discontinuously from a maximum to zero, as z crosses the turning point z_T associated with (v_i, v_j).

To avoid the problem of density discontinuities the contribution of bin (ij) should be calculated only from that portion of the bin that actually reaches z. The fraction of a given bin that has $z_T > z$ can be determined by examining the values of $v_\parallel^2$ at the corners of the bin. To make this clear, a few preliminary definitions are helpful:

$$(E5)\quad v_{11}^2 = v_{\parallel 11}^2 - \left(\frac{B}{B_o}-1\right)v_{\perp 11}^2 - \frac{2q}{m}(\phi-\phi_o)$$

$$v_{12}^2 = v_{\parallel 11}^2 - \left(\frac{B}{B_o}-1\right)v_{\perp 12}^2 - \frac{2q}{m}(\phi-\phi_o)$$

$$v_{21}^2 = v_{\parallel 12}^2 - \left(\frac{B}{B_o}-1\right)v_{\perp 11}^2 - \frac{2q}{m}(\phi-\phi_o)$$

$$v_{22}^2 = v_{\parallel 12}^2 - \left(\frac{B}{B_o}-1\right)v_{\perp 12}^2 - \frac{2q}{m}(\phi-\phi_o)$$

$$v_{\parallel 11} \equiv v_i - \frac{\Delta v}{2}\qquad v_{\parallel 12} \equiv v_j + \frac{\Delta v}{2}\qquad v_{\perp 11} \equiv v_j - \frac{\Delta v}{2}\qquad v_{\perp 12} \equiv v_j + \frac{\Delta v}{2}$$

The subscripts 11, 12, 21 and 22 stand for the lower left, upper left, lower right, and upper right corners of the bin, respectively. Table E.1 shows the situations that can arise. Note that all of the cases can be described by the single formula

$$(E6)\quad \Delta n_{ij} = \frac{4\pi}{3}\,\frac{B}{B-B_o}\,f_{ij}\sum_{\alpha,\beta}\varepsilon_{\alpha\beta}\,v_{\alpha\beta}^3$$

where α and β each take on values 1 and 2, with

$$(E7)\quad \varepsilon_{\alpha\beta} = 1 - 2\delta_{\alpha\beta} \qquad \text{if } v_{\alpha\beta}^2 > 0$$
$$= 0 \qquad \text{if } v_{\alpha\beta}^2 \le 0$$

$\delta_{\alpha\beta}$ is the Kronecker δ function.

In other words, starting with

$$\text{(E8)} \qquad \Delta n_{ij} = \frac{4\pi}{3} \frac{B}{B-B_o} f_{ij} \left[v_{12}^3 + v_{21}^3 - v_{11}^3 - v_{22}^3 \right] ,$$

one deletes those $v_{\alpha\beta}^3$ terms for which $v_{\alpha\beta}^2$ is negative.

The increment of squared parallel speed per unit volume is

$$\text{(E9)} \quad \Delta(nv_{\parallel}^2)_{ij} = \frac{4\pi}{15} \frac{B}{B-B_o} f_{ij} \sum_{\alpha,\beta} \epsilon_{\alpha\beta} v_{\alpha\beta}^5$$

The increment of squared perpendicular speed per unit volume is

$$\text{(E10)} \quad \Delta(nv_{\perp}^2)_{ij} = \frac{4\pi}{15} \left(\frac{B}{B-B_o}\right)^2 f_{ij} \sum_{\alpha,\beta} \epsilon_{\alpha\beta} \left(2v_{\alpha\beta}^5 + 5\left(\frac{B}{B_o} - 1\right) v_{\alpha\beta}^3 v_{1\beta}^2\right)$$

The parallel particle flux increment per unit area is

$$\text{(E11)} \quad \Delta(nv_{\parallel})_{ij} = \frac{\pi}{2} \frac{B}{B-B_o} f_{ij} \sum_{\alpha,\beta} \epsilon_{\alpha\beta} v_{\alpha\beta}^4$$

The rate of increase of the number of particles along a flux tube due to ionization events associated with resonance zone velocity space bin ij, between resonance zones of cross sectional area A, is

$$\text{(E12)}$$

$$\dot{N}_{ij} = A\, n_g\, \sigma_{ij}\, v_i\, (v_i^2 + v_j^2)^{1/2}\, f_{ij} \int_{-Z_{res}}^{Z_{res}} dz\, \left(v_i^2 - \left(\frac{B}{B_{res}} - 1\right) v_j^2\right)^{-1/2}$$

$$= 8\pi\, (\Delta v)^2$$

$$A\, n_g\, \sigma_{ij}\, v_i\, (v_i^2 + v_j^2)^{1/2}\, f_{ij}\, \sqrt{\left(\frac{r}{\beta}\right)}\, \sin^{-1}\left(\left\{1 + \frac{r}{r-1} \frac{v_i^2}{v_j^2}\right\}^{-1/2}\right)$$

In (E12) it is assumed that no potential difference exists along field lines. The neutral density is n_g, and the ionization cross section for $v = (v_i^2 + v_j^2)^{1/2}$ is σ_{ij}. The entire contribution from resonance passing particles is

$$\text{(E13)} \quad \dot{N}_r = 8\pi\, n_g\, A\, (\Delta v)^2 \sqrt{\left(\frac{r}{\beta}\right)} \times$$

$$\sum_{i,j} v_i\, (v_i^2 + v_j^2)^{1/2}\, \sigma_{ij}\, f_{ij}\, \sin^{-1}\left\{1 + \frac{r}{r-1} \frac{v_i^2}{v_j^2}\right\}^{-1/2}$$

For a Maxwellian population of non-resonance passing particles, there is an additional increment

$$\text{(E14)} \quad \dot{N}_{nr} = n_g\, n_*\, \langle\sigma v\rangle_{Max}\, Z_{res}\, \left(\frac{r}{r-1}\right)^{1/2} (\sqrt{r} - 1)$$

where n_* is the density of complete Maxwellian, and $\langle\sigma v\rangle_{Max}$ is the averaged product of cross section and speed for the complete Maxwellian.

In steady state the particle input to the system from (E13) and (E14) must be balanced by a loss current. With B and ϕ from (E5) interpreted as the loss position values B_L and ϕ_L, the loss current contribution from resonance zone bin ij is

$$(E15) \quad \dot{N}_{ij}\,(\text{loss}) = A\,\frac{\pi}{2}\,\frac{B_R}{B_R - B_L}\,f_{ij}\sum_{\alpha,\beta}\epsilon_{\alpha\beta}\,v_{\alpha\beta}^4$$

When the grid is chosen to represent resonance zone velocity space use can be made of the fact that cyclotron heating can be represented by changes in $v_\perp$ only, and that the change at a given resonance passage is

$$(E16) \quad \Delta v_\perp = v_{\perp max}\cos\theta$$

where θ is the angle between $\vec{v}_\perp$ and the microwave electric field $\vec{E}$, and is a random variable if the particle is in the stochastic regime. The maximum change in $v_\perp$, $v_{\perp max}$, is calculable in each bin of v-space. In a particular bin,

$$(E17) \quad \Delta v_{\perp max} = (M + \delta)\Delta v \qquad 0 \le \delta < 1,\ M = 0, 1, 2, 3 \ldots$$

M is the integer part and δ the fractional part of $\Delta v_{\perp max}$, normalized to the bin size δv. The task is to evaluate the probability $P_{ijj'}$ that a particle in bin ij will appear, after resonance passage, in bin ij'. With uniform distributions within each bin, and with the θ values randomly distributed in $[0,2\pi]$, then the probabilities of transfer from a bin with a given j in the case of M=0 are

$$(E18) \quad \begin{aligned} P_{ij(j-1)} &= \delta/\pi \\ P_{ij(j)} &= 1 - 2\delta/\pi \\ P_{ij(j+1)} &= \delta/\pi \end{aligned} \qquad (M = 0)$$

In the case of M>1, the probabilities are

(E19)

$$P_{ij(j+m)} = \frac{1}{\pi}\{2m\cos^{-1}\left(\frac{m}{M+\delta}\right) - (m-1)\cos^{-1}\left(\frac{m-1}{M+\delta}\right) - (m+1)\cos^{-1}\left(\frac{m+1}{M+\delta}\right) + [(M+\delta)^2-(m+1)^2]^{1/2} + [(M+\delta)^2-(m-1)^2]^{1/2} - 2[(M+\delta)^2 - m^2]^{1/2}\}$$

$$P_{ij(j+M)} = \frac{1}{\pi}\{2M\cos^{-1}\left(\frac{M}{M+\delta}\right) - (M-1)\cos^{-1}\left(\frac{M-1}{M+\delta}\right) - 2[(M+\delta)^2 - M^2]^{1/2}\}$$

$$P_{ij(j+M+1)} = \frac{1}{\pi}\{[(M+\delta)^2-M^2]^{1/2} - M\cos^{-1}\left(\frac{M}{M+\delta}\right)\}$$

The probability to transfer to bin j-m is the same as to bin j+m, due to symmetry of $\Delta v_\perp$ in (E16). Note that a transfer that has $j-m < 0$ is equivalent to a transfer to bin $1+m-j > 0$. $v_\perp$ must must be non-negative.

For iteration of the distribution function these probabilities must be adjusted to represent changes per unit time. After allowing for differing bounce times τ_{ij} and the differences in phase space volumes, one obtains

$$\text{(E20)} \quad \dot{f}_{ij'} = 4 \sum_{j} \left(\frac{v_j}{v_{j'}} f_{ij} P_{ijj'}/\tau_{ij} - f_{ij'} P_{ij'j}/\tau_{ij'} \right)$$

REFERENCE

[1]National Magnetic Fusion Energy Computer Center, CFT, (Rev. Date Mar. 3.20, 1980), p. 186ff.

Table E.1

Density increment from a uniformly populated velocity space bin.

The shaded portion of the bin has a turning point beyond z.

Bin Type	Density Expression
	$\Delta n_{ij} = \frac{4\pi}{3} \frac{B}{B-B_o} f_{ij} \left[v_{12}^3 + v_{21}^3 - v_{11}^3 - v_{22}^3 \right]$
	$\Delta n_{ij} = \frac{4\pi}{3} \frac{B}{B-B_o} f_{ij} \left[v_{21}^3 - v_{11}^3 - v_{22}^3 \right]$
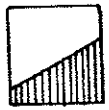	$\Delta n_{ij} = \frac{4\pi}{3} \frac{B}{B-B_o} f_{ij} \left[v_{21}^3 - v_{11}^3 \right]$
	$\Delta n_{ij} = \frac{4\pi}{3} \frac{B}{B-B_o} f_{ij} \left[v_{21}^3 - v_{22}^3 \right]$
	$\Delta n_{ij} = \frac{4\pi}{3} \frac{B}{B-B_o} f_{ij} \; v_{21}^3$

Appendix F

Spurious V_f dips resulting from finite probe impedance

The apparent reality of local density peaks brings up a source of possible worry about the V_f dips. Apparent extrema of V_f can result if an insufficiently large probe impedance is used at a density peak. To obtain the magnitude of this effect, note that the IV curve near V_f is approximately

$$(F1)\quad I = \frac{dI}{dV}\Big|_{V_f} (V - V_f) = R_s (V - V_f)$$

where R_s is the "sheath resistance". The load line of the input resistance R_{in} is given by

$$(F2)\quad I = -V/R_{in}$$

The apparent floating potential, V_{fm} is located at the intersection of these two curves:

$$(F3)\quad V_{fm} = \frac{\frac{dI}{dV}\Big|_{V_f}}{\frac{dI}{dV}\Big|_{V_f} + \frac{1}{R}} V_f = \frac{R_{in}}{R_{in} + R_s} V_f$$

Figure F.1 shows this. If $R_{in} \sim R_s$ a density peak can cause V_{fm} to rise (or fall) away from zero toward its true value.

R_s is found from the general expression for probe current:

$$(F4)\quad \frac{1}{R_s} = \frac{dI}{dV}\Big|_{V_f} = A_p\, n\, e\, \left(\frac{kT_e}{2\pi m_e}\right)^{1/2} \frac{e}{kT_e} \left(\frac{2\pi m_e}{m_i}\right) \exp\left(-\frac{1}{2}\right)$$

$$= 1.26 \times 10^{-15}\, A_p[m^2]\, n[m^{-3}]\, T[eV]^{-1/2}\, m_i[amu]^{-1/2}$$

The ratio $\frac{V_{fm}}{\text{true } V_f}$ is shown in figure F.2

For typical probe tip areas and plasma densities of these experiments, 10 MΩ input impedance is adequate to prevent this spurious V_f effect. Usually a value of 100 MΩ input impedance was used, obtained with the Hewlett-Packard null voltmeter. This effect can also be avoided by using low impedance (i. e., IV plot) data.

FIGURE F.1 SIMPLIFIED I-V DIAGRAM OF HIGH IMPEDANCE V_F PROBE.

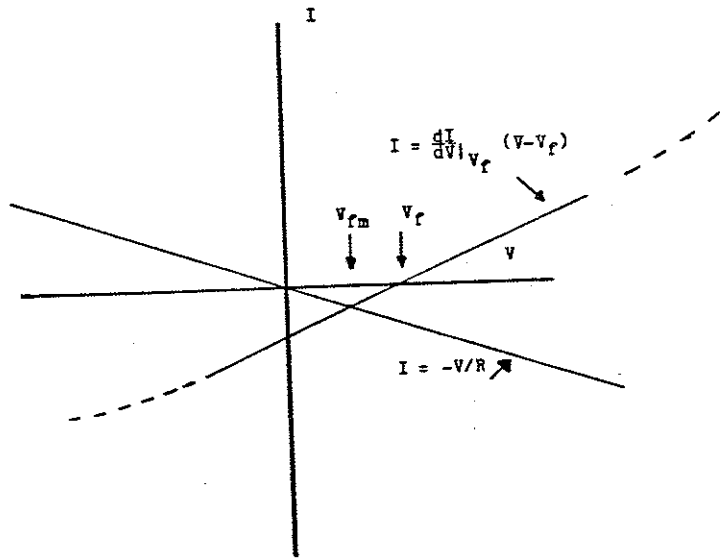

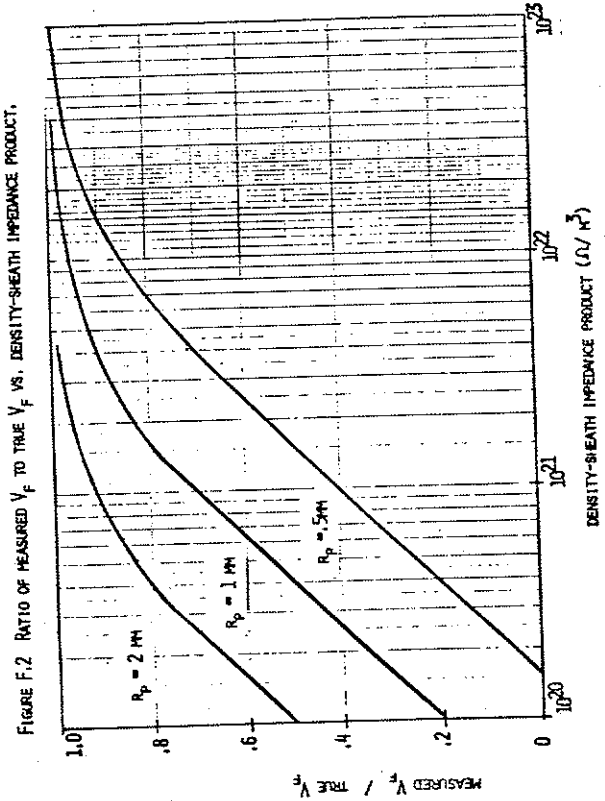

FIGURE F.2 RATIO OF MEASURED V_F TO TRUE V_F VS. DENSITY-SHEATH IMPEDANCE PRODUCT.

Appendix G

Relationship of ion saturation peak FWHM and density peak FWHM

For the sake of rapid data acquisition many ion saturation current ("I_{isat}") profiles were taken over the course of this research without getting an IV-trace at each point. For constant T_e, formulat 3.1.2 indicates the plasma density and I_{isat} are directly proportional, so that the FWHM of the I_{isat} and density peaks are identical.

However, both experimentally and theoretically, the mean speed of electrons has a peak near resonance. The question then arises whether the I_{isat} FWHM is still indicative of the density FWHM. What follows is an estimate based on idealized Gaussian peaks of I_{isat} and T_e.

For $\Delta V_p \ll \Delta V_f$, the V_f dip has the same shape (though inverted) as does the T_e peak. This is a result of

$$(G1) \qquad \frac{kT_e}{e} = \frac{V_p - V_f}{\alpha}$$

Approximating the T_e and I_{isat} peaks by Gaussians gives

$$(G2a) \qquad T_e = T_{eo}(1 + (h_T - 1) \exp[-k_T z^2])$$

$$(G2b) \qquad I_{isat} = I_{isat,o}(1 + (h_I - 1) \exp[-k_I z^2])$$

In these equations h_T is the ratio of peak temperature to

background temperature T_{eo}. The ratio of peak ion saturation current to the background level is h_I. The relationship between the coefficients within the exponentials and the FWHM's is

$$(G3) \qquad k = \frac{4 \ln 2}{(\text{FWHM})^2}$$

There is considerable scatter in the spread of FWHM's of V_f (thus T_e) and of I_{isat}. For a series of experiments in helium with the same field as shown in figure 5.7, it was found

$$\frac{\text{FWHM for } V_f}{\text{FWHM for } I_{isat}} = .66 \pm .45 \quad .$$

In view of this general spread, estimates of the ratio of the density FWHM were made for two cases:

(1) FWHM for V_f = FWHM for I_{isat}.

(2) FWHM for $V_f = \frac{1}{2}$ FWHM for I_{isat}.

For a given pair of enhancement ratios (h_T, h_I) the half-peak-density value is $\frac{1}{2}(1 + h_I/\sqrt{h_T})$. A short program was written to find the density FWHM resulting from (G2a) and (G2b). Table G.1 give the resulting FWHM values as a fraction of the I_{isat} FWHM. The significant message here is that, except for very large T_e enhancements, the ion saturation current FWHM is very close in value to the density FWHM. This justifies the use of I_{isat} FWHM values for density FWHM in fig. 7.27

Table G.1

Ratio of density FWHM to ion saturation peak FWHM

I. T_e FWHM = I_{isat} FWHM

ion sat. cur. peak ratio	T_e enhancement ratio 1.1	1.2	1.5	2	3	5
1.1	1.009	0.734	---	---	---	---
1.2	1.014	1.016	---	---	---	---
1.5	1.016	1.028	1.037	0.810	---	---
2.0	1.017	1.030	1.058	1.063	0.869	---
3.0	1.017	1.031	1.065	1.096	1.099	0.940
5.0	1.017	1.032	1.068	1.108	1.145	1.143

II. T_e FWHM = $\frac{1}{2}$ I_{isat} FWHM

ion sat. cur. peak ratio	T_e enhancement ratio 1.1	1.2	1.5	2	3	5
1.1	1.009	0.734	---	---	---	---
1.2	0.919	0.798	---	---	---	---
1.5	0.977	0.947	0.818	0.464	---	---
2.0	0.994	0.985	0.944	0.843	0.569	---
3.0	1.002	1.002	0.995	0.965	0.877	0.673
5.0	1.006	1.010	1.017	1.016	0.991	0.918